



Michigan Technological University
Create the Future Digital Commons @ Michigan Tech

Dissertations, Master's Theses and Master's
Reports - Open

Dissertations, Master's Theses and Master's
Reports

2009

Micro-fabrication of bio-MEMS based force sensor to measure the force response of living cells

Varun Gouthaman
Michigan Technological University

Follow this and additional works at: <https://digitalcommons.mtu.edu/etds>



Part of the [Mechanical Engineering Commons](#)

Copyright 2009 Varun Gouthaman

Recommended Citation

Gouthaman, Varun, "Micro-fabrication of bio-MEMS based force sensor to measure the force response of living cells", Master's Thesis, Michigan Technological University, 2009.
<https://doi.org/10.37099/mtu.dc.etds/367>

Follow this and additional works at: <https://digitalcommons.mtu.edu/etds>



Part of the [Mechanical Engineering Commons](#)

MICRO-FABRICATION OF BIO-MEMS BASED FORCE SENSOR TO
MEASURE THE FORCE RESPONSE OF LIVING CELLS

By

Varun Gouthaman

A THESIS

Submitted in partial fulfillment of the requirements

for the degree of

MASTER OF SCIENCE IN MECHANICAL ENGINEERING

MICHIGAN TECHNOLOGICAL UNIVERSITY

2009

Copyright © Varun Gouthaman 2009

This thesis, “Micro-Fabrication of Bio-MEMS based force sensor to measure the force response of a living cell” is hereby approved in partial fulfillment of the requirements for the Degree of MASTER OF SCIENCE IN MECHANICAL ENGINEERING.

DEPARTMENT:

Mechanical Engineering-Engineering Mechanics

Signatures:

Thesis Advisor: _____

Dr.Reza Shahbazian Yassar.

Department Chair: _____

Dr. William W. Predebon

Date: _____

Acknowledgements

I would like to sincerely thank my advisor, Dr. Reza Shahbazian Yassar for giving me this opportunity to work with some of the latest research in the world. I would like to thank him for all his help, guidance and support for the entire duration of my Master's Thesis. I would also like to thank Mr. Bill Knudsen for all his help throughout the experimentation and the fabrication processes. I would also like to thank my committee members Dr. Dennis Desheng Meng and Dr. Patricia Heiden for their time and effort.

I would like to thank Dr. K.V.C Rao for all his support that he endeared throughout my Master's program. I must say I enjoyed working with him and being his teaching assistant. I would like to thank Dr. Paul Bergstrom and Dr. Khalil Najafi who changed my outlook towards MEMS and helped me develop a keen interest in MEMS.

I would like to thank my friends Alex Joseph, Sunand Santhanagopalan, Michael Oisten, and Kumar Vanga who answered all my questions, helped me without any hesitation during the fabrication processes. I wish them all the best with their endeavors. I would also like to thank Mr. Greg Armatys to help me get through my Internship with Caterpillar and being the best mentor that I could have.

Last but not the least, I would like to thank my parents for giving me this opportunity to study abroad, pursue my Master's degree. I would like to thank my father G. Gouthaman for being a genius that he is, and helping me throughout my life. I would like to thank my mother Praveena G for her endless love and support.

Table of Contents

<i>ABSTRACT.....</i>	<i>xi</i>
<i>LIST OF FIGURES.....</i>	<i>xiii</i>
<i>CHAPTER 1 – INTRODUCTION.....</i>	<i>1</i>
1.1 Motivation.....	1
1.2 Cell Mechanics using MEMS.....	2
<i>CHAPTER 2 – INTRODUCTION TO MEMS TECHNOLOGIES.....</i>	<i>5</i>
2.1 MEMS Materials.....	6
2.2 Micro-Fabrication Techniques.....	7
2.2.1 Oxidation.....	7
2.2.2 Film Deposition.....	10
2.2.2.1 Evaporation.....	11
2.2.2.2 Sputtering.....	12
2.2.3 Photo-Lithography.....	13
2.2.4 Silicon Etching.....	15
2.2.5 Etch Stops.....	23
2.2.6 SCREAM Process.....	26
<i>CHAPTER 3 - MEMS Devices for Materials Testing and Cell Mechanics.....</i>	<i>27</i>
3.1 MEMS Devices for Material Sciences.....	29
3.1.1. First generation MEMS device.....	29
3.1.2. Second generation MEMS device.....	31
3.1.3. MEMS-device based on Force Capacitance	34
3.1.4. MEMS Device based on Beam Buckling.....	37
3.1.5. MEMS device for Indentation testing of freestanding nano-films...	40
3.1.6. MEMS Devices for Mechanical Testing of 1D Materials.....	41
3.1.7. Electrostatic Actuated Nano Tensile Testing Device (EANAT)..	48

3.1.8. Force Sensor Technologies.....	52
3.1.9. Actuator System.....	64
3.2. MEMS Devices for Life Sciences	72
3.2.1. Bio-MEMS based force sensor.....	73
3.2.1.1. Force Sensor working principle.....	74
3.2.1.2. Experimental Results.....	75
3.2.1.3. Multi-directional Force Sensors.....	78
3.2.2. MEMS platform for biaxial stimulation of living cells...	79
3.2.2.1. Experimental Results	82
3.2.3. BioMEMS Devices for Uniaxial Cell Stretching.....	85
3.2.3.1. Force Sensing Technique.....	87
3.2.3.2. Experimental Results.....	88
CHAPTER 4 – BIO-MEMS FORCE SENSOR FABRICATION.....	89
4.1 Oxidation.....	95
4.2 Photo-Lithography.....	102
4.2.1 Shipley SC 1827.....	104
4.2.2 P-Fuurrex: PR-2000.....	113
4.2.3 AZ-P4620.....	116
4.3 Etching.....	120
4.3.1 Reactive Ion Etching.....	121
4.3.2 Anisotropic Etching.....	142
4.4 Dry Thermal Oxidation.....	151
4.5 Isotropic Etching.....	154

<i>CHAPTER 5 – CONCLUSIONS AND RECOMMENDATIONS FOR FUTURE</i>	
<i>WORK.....</i>	<i>161</i>
<i>5.1 Conclusion.....</i>	<i>161</i>
<i>5.2 Results Summary.....</i>	<i>163</i>
<i>5.3 Recommendations for Future Work.....</i>	<i>164</i>
<i>BIBLIOGRAPHY</i>	<i>167</i>
<i>APPENDIX- A.....</i>	<i>175</i>
<i>APPENDIX- B.....</i>	<i>176</i>
<i>APPENDIX- C</i>	<i>177</i>
<i>APPENDIX- D.....</i>	<i>178</i>
<i>APPENDIX- E.....</i>	<i>179</i>
<i>APPENDIX- F</i>	<i>187</i>

Abstract

Understanding how a living cell behaves has become a very important topic in today's research field. Hence, different sensors and testing devices have been designed to test the mechanical properties of these living cells. This thesis presents a method of micro-fabricating a bio-MEMS based force sensor which is used to measure the force response of living cells. Initially, the basic concepts of MEMS have been discussed and the different micro-fabrication techniques used to manufacture various MEMS devices have been described. There have been many MEMS based devices manufactured and employed for testing many nano-materials and bio-materials. Each of the MEMS based devices described in this thesis use a novel concept of testing the specimens. The different specimens tested are nano-tubes, nano-wires, thin film membranes and biological living cells. Hence, these different devices used for material testing and cell mechanics have been explained.

The micro-fabrication techniques used to fabricate this force sensor has been described and the experiments performed to successfully characterize each step in the fabrication have been explained. The fabrication of this force sensor is based on the facilities available at Michigan Technological University. There are some interesting and uncommon concepts in MEMS which have been observed during this fabrication. These concepts in MEMS which have been observed are shown in multiple SEM images.

Abstract

List of Figures

Figure 2.1: Schematic of the apparatus showing the high temperature oxidation procedure.....	8
Figure 2.2: Oxide growth rate of (100) Si wafer in dry and wet ambience (Gandhi, 1994).....	10
Figure 2.3: Schematic diagram of the experimental setup of sputtering system.....	12
Figure 2.4: Schematic of Photolithography process, showing the effect of photo-resist.....	14
Figure 2.5: Crystallographic planes of Si and their orientations showing the Miller Indices.....	18
Figure 2.6: Schematic of an anisotropic etch process.....	19
Figure 2.7: Schematic of the anisotropic etching in the exposed corners of the mask.....	20
Figure 2.8: Schematic of scalloping process.....	23
Figure 2.9: Step by step micro-fabrication process explaining the SCREAM process.....	26
Figure 3.1: SEM image of the device. (Haque et al, 2002).....	29
Figure 3.2: The stress strain relationship for a 200 nm aluminum thin film (Haque et al, 2002).....	31
Figure 3.3: SEM image of the device. (Han et al, 2006).....	33
Figure 3.4: Result of uniaxial tensile test by Han and Saif (2006).....	34
Figure 3.5: SEM image of the device (Espinosa et al, 2007).....	35
Figure 3.6: Results from the test performed on the device by Zhu and Espinosa (Espinosa et al, 2007).....	36
Figure 3.7: MEMS based testing device by Samuel and Haque (Samuel et al, 2006).....	37
Figure 3.8: Results from the test performed on the device by Samuel and Haque (Samuel et al, 2006).....	39
Figure 3.9: SEM image of the device (Leseman et al, 2007).....	41
Figure 3.10: SEM image of the device (Demczyk et al, 2002).....	43
Figure 3.11: Multiwall carbon nano-tube just prior to tensile testing (Demczyk et al, 2002)	43
Figure 3.12: In-situ bending sequence on a single multi-walled carbon nano-tube.(Demczyk et al, 2002).....	44
Figure 3.13: SEM image of a MEMS-based testing device with direct force sensing beams (Lu et al, 2006).....	45
Figure 3.14: A SEM image of a T-CNT deposited across the platforms before being clamped. (Lu et al, 2006).....	47
Figure 3.15: Stress vs strain data for a T-CNT loaded with the MEMS device (Lu et al, 2006).....	47
Figure 3.16: Schematic of the design layout for an <i>ENAT</i> (Kuichi et al, 2007).....	48
Figure 3.17: Load-displacement curves for carbon nano-wires on <i>ENATs</i> (Kuichi et al, 2007).....	51

List of Figures

Figure 3.18: SEM micrograph of the entire stage showing the calibration of force sensing beams of the device.....	54
Figure 3.19: Description of the calibrator design by Han and Saif (Haque et al, 2002).....	54
Figure 3.20: Double-chip architecture used for measuring capacitance change. (Espinosa et al, 2007).....	55
Figure 3.21: Device with ETA and corresponding resistances and capacitances (Espinosa et al, 2006).....	57
Figure 3.22: The plot of capacitance change vs displacement (Espinosa et al, 2006).....	57
Figure 3.23: Calibration curve for the load cell used in the experiments by Leseman and Mackin in 2007.....	60
Figure 3.24: Schematic ready experimental setup of the design by Leseman and Mackin in 2007.....	61
Figure 3.25: Schematic diagram of the cantilever used as the lever amplification system. (Kiuchi et al, 2007).....	64
Figure 3.26: Schematic figure of the device showing the pulling direction and the actuation (Haque et al, 2002).....	65
Figure 3.27: SEM image of the MEMS device being tested and the piezo electric actuator (Haque et al, 2002).....	65
Figure 3.28: Schematic figure of the thermal actuator by Zhu and Espinosa (2007).....	66
Figure 3.29: Results by Zhu and Espinosa (a) Temperature and (b) displacement fields in the thermal actuator	67
Figure 3.30: Schematic of experimental setup by Leseman and Mackin in 2007.....	69
Figure 3.31: Schematic and the SEM image of the device by Yang and Saif (Yang et al, 2005).....	73
Figure 3.32: Experimental system and the sensor to measure the force response of the living cell (Yang et al, 2005)...	75
Figure 3.33: Morphological changes of two cells due to mechanical disturbance of the sensor probe.....	77
Figure 3.34: Force response of a MKF due to large lateral indentation (Yang et al, 2005)	78
Figure 3.35: The developments to the previous design (Yang et al, 2007).....	79
Figure 3.36: Layout of the MEMS based biaxial cell stretcher (Scuor et al, 2006)	80
Figure 3.39: Kinematic principle of the biaxial cell stretcher platform (Scuor et al, 2006)	81
Figure 3.38: Micro-graphs representing the biaxial cell stretcher platform in air at (a) 0V and (b) 100V	83
Figure 3.39: Plot of the cell stretcher displacement vs driving voltage in air. (Scuor et al, 2006).....	84
Figure 3.40: Micrograph representing the biaxial cell stretcher in DI water at (a) 0V and (b) 20V.....	84
Figure 3.41: Schematic of the BioMEMS device for uniaxial cell stretching (Serrell et al, 2007).....	85
Figure 3.42: Schematic of the complete device with the actuation and force sensing system (Serrell et al, 2007).....	86
Figure 4.1: Pattern and the dimensions of the clear-field mask	89
Figure 4.2: Schematic of step 1 of fabrication process, showing the cross section.....	91
Figure 4.3: Schematic of step 3 of fabrication process, showing the cross section.....	92

List of Figures

Figure 4.4: Schematic of step 3 of fabrication process, showing the cross section.....	92
Figure 4.5: Schematic of step 6 of fabrication process, showing the cross section.....	93
Figure 4.6: Schematic of step 7 of fabrication process, showing the cross section.....	93
Figure 4.7: Schematic of step 8 of fabrication process, showing the cross section.....	94
Figure 4.8: Schematic of step of fabrication process after the cantilevers have been obtained and SiO_2 is remove	94
Figure 4.9: Mellen Furnace to perform dry thermal oxidation.....	95
Figure 4.10: Oxide thickness vs. time plot for dry ambience (Gandhi, 1994).....	96
Figure 4.11 (a): Filmetrics tool which measures the oxide thickness.....	97
Figure 4.11(b): Oxide Thickness measured after the thermal oxidation (258 nm with a goodness of fit of 0.99945)...	98
Figure 4.12: Perkin-Elmer 8 inch sputter tool.....	99
Figure 4.13: Ultek Auto Pumpdown control panel.....	100
Figure 4.14: Oxide Thickness measured after sputtering using Filmetrics.....	101
Figure 4.15: Oxide thickness measured after thermal oxidation using Filmetrics.....	102
Figure 4.16: Figure shows the distinction between clear field mask and dark field mask.....	103
Figure 4.17: Picture showing the Fume hood inside the clean room.....	106
Figure 4.18: DEKTAK 6M Profiler used to measure the step profile of the etched material on the substrate.....	108
Figure 4.19: Plot showing the thickness result given to be $28571 \text{ \AA} = 2.85 \mu\text{m}$	109
Figure 4.20: Plot showing the thickness result given to be $32535 \text{ \AA} = 3.25 \mu\text{m}$	111
Figure 4.21: Spin speed vs. the thickness obtained plot, shown for SC 1827 photo-resist.....	113
Figure 4.22: Picture showing the photo-resist P-Futurrex in the clean room.....	114
Figure 4.23: Plot showing the thickness result given to be $19688 \text{ \AA} = 1.97 \mu\text{m}$	115
Figure 4.24: Picture showing the photo-resist AZ-P4620 in the clean room.....	116
Figure 4.25: Plot showing the thickness result given to be $95398 \text{ \AA} = 9.54 \mu\text{m}$	118
Figure 4.26: Automated Dicing System which was used for all the dicing purposes.....	118
Figure 4.27: SEM image of the SC1827 photo-resist patterned on the Si wafer.....	119
Figure 4.28: TRION ICP-RIE system, which was used for all the etch characterizations.....	120
Figure 4.29: Schematic showing the etching of PR as well as SiO_2 taking place.....	125

List of Figures

Figure 4.30: Oxide Thickness measured after 8 minutes of etching, using Filmetrics.....	134
Figure 4.31: Schematic showing the etching of PR as well as SiO ₂ taking place after 8 minutes.....	136
Figure 4.32: SEM image of the 32 minute RIE etch. Sidewalls of the features are visible very clearly.....	138
Figure 4.33: SEM image force sensor beam along with the support features.....	139
Figure 4.34: SEM image of the force sensor beam and the nearby regions after plasma etch.....	139
Figure 4.35: Picture of a failed sample while taking it out of the SEM sample holder.....	140
Figure 4.36: The thickness of the thermal oxide layer before the KOH etch was 975 nm.....	146
Figure 4.37: SEM image of the Si substrate being etched by KOH.....	147
Figure 4.38: SEM image of the feature side walls, showing a depth of 24 microns of sidewalls.....	148
Figure 4.39: SEM image of the probe end of the device. The exposed convex corners are clearly being etched.....	149
Figure 4.40 SEM image showing the weakening of the oxide mask.....	149
Figure 4.41 SEM image showing the device in the minimum magnification.....	150
Figure 4.42 Laboratory experimental setup of the thermal oxidation furnace.....	152
Figure 4.43: Oxide thickness of the coupon 1 and coupon 2.....	153
Figure 4.44: SEM image of the sample after performing RIE for 4 minutes to remove the Oxide layer.....	154
Figure 4.45: SEM image of the sample after the first attempt on isotropic etching.....	157
Figure 4.46: SEM image of the sample after the test 2 on isotropic etching.....	158
Figure 4.47: SEM image of the sample after the test 3 in isotropic etching.....	159
Figure 5.1: Picture showing the experimental which is required.....	165

Chapter 1

Introduction

1.1. Motivation

A living cell is the structural and functional unit of all living organisms. A biological cell performs various functions for the sustenance of the living organism. Some of the cell functions are: synthesis of bio-molecules, storage and transport of genetic information, transmission and transduction of nervous signals. The living cell also converts energy from one form to another. The living cells also have a property of altering their structure when necessary. Lately, studies have shown that mechanical forces have a great influence on the living cells.

Mechanical stresses on living cells can affect various cellular processes such as growth, differentiation, transduction of proteins, and cell division. The mechanical forces on cells are some known causes for diseases such as sickle cell anemia and asthma. Some bone cells and the cells in the endothelium are subjected to forces throughout their existence. Any change would have a drastic effect on their functioning. Some cells such as cochlear outer hair cells, convert the electrical and chemical stimulus into a mechanical force. Some cells such as the axon of the nerve cells die when they are stretched severely. But when they are stretched slowly, it helps the neural cell growth. The cell locomotion is altered with the stiffness of the environment. The cells have an ability to change their direction by sensing the stiffness of their surrounding substrate.

Hence, this makes it extremely important to understand how living cells behave under the influence of mechanical forces and stresses. (Bao et al, 2003)

1.2. Cell Mechanics using MEMS

There have been multiple techniques developed to measure the mechanical responses of living cells. The most common ones are atomic force microscopy (AFM), magnetic twisting cytometry (MTC), magnetic traps, optical traps, and silicon cantilevers etc. The size of the living cells is in the order of microns. All the above techniques work in the dimensional range of micro-meters. In today's world of research there is another technique which is being used to test the mechanical response of the living cells. Micro-electro mechanical systems (MEMS) have been a popular method to build devices which can perform mechanical tests on living cells. They are increasingly being used as tools in biological applications due to their dimensional advantage. MEMS are systems which can act as sensors, actuators, and specimen holders. When put together, you get a device which can perform characterizations on different materials. In addition to living cells, with MEMS we can test nano-materials of different kinds. Not only can we perform mechanical characterizations of materials, but also electrical characterizations when needed.

In this thesis, we mainly talk about one of such MEMS devices which can measure the mechanical force response of biological living cell. This MEMS device constitutes mainly of two parts: probe and force sensing beams. The probe performs

indentation or stretching of the cells and the force sensing beams can measure the amount of force that the cell is withstanding. In this thesis we talk about the fabrication of this force sensor. This thesis is divided into three parts. In the first part basic concepts of MEMS is explained. Different MEMS techniques used to fabricate the devices and some interesting concepts of MEMS is described. These are the micro-fabrication techniques which have been used to fabricate the force sensor.

The second part of this thesis describes some of the MEMS techniques used to design and fabricate the devices to perform material testing. It also discusses application of MEMS in the field of life sciences. Some of the MEMS devices which have been designed and used to perform experimentation on living cells have been examined. The basic idea, the working principle, and the experimental results of these devices have also been described.

The third part in this thesis discusses the experimental techniques used to perform the micro-fabrication of the force sensor. There are seven micro-fabrication steps to fabricate this device. Each of these seven steps needs characterization to correctly fabricate this device. The facilities available at Michigan Technological University have been used to perform this micro-fabrication.

Finally some recommendations and conclusions have been made based on the results obtained during this fabrication process. Hence, with this we will move on to the first part which explains the basic concepts of MEMS techniques.

Chapter 1- Introduction

Chapter 2

Introduction to MEMS Technologies

Micro electro mechanical systems (MEMS) are a set of miniature multifunctional Microsystems consisting of sensors, actuators, mechanical elements, and electronics on a common silicon substrate. These MEMS systems are built using micromachining technologies. Micromachining is an enabling technology that allows the formation of physical as well as electronic devices. It uses many of the standard silicon IC fabrication techniques. Sensors are the devices that can measure a parameter of interest, typically non electrical, and generate an electrical signal that can be processed by computers. Actuators are the devices that convert one signal into some other form of signal that can be delivered to an environment of interest. Many different types of non-electrical signals exist, and therefore a number of transduction techniques have been utilized to convert non- electrical signals to electrical signals. Transducers are generally referred to as devices that convert signals of a particular type to another type of signal. Sometimes transducers are also energy conversion devices, meaning that they not only convert one type of signal to another, they also convert one form of energy to another.

There are several applications for MEMS and nanotechnology. MEMS techniques are being used in different fields such as weather forecasting and environmental monitoring, biomedical systems (diagnostic and therapeutic), homeland security and

Chapter 2- Introduction to MEMS Technologies

defense applications, communication systems (RF and optical), consumer electronics, appliances, entertainment, transportation systems, adaptive automated manufacturing tools, smart homes and wide ranging consumer products, space probes and launch/satellite instrumentation, and power generation etc. The most widely used areas are: biotechnology, communications, and accelerometers. The working of the electrical inductors and capacitors can be improved significantly compared to their integrated counterparts if they are made using MEMS and Nanotechnology. The performance of communication circuits will improve with the integration of such components, while the power consumption and the cost will be reduced. (Bryant & Bernard, 2000)

2.1. MEMS Materials:

The most important and the basic material used in MEMS techniques is Silicon. Silicon is used to create most integrated circuits used in consumer electronics in the modern world. Silicon also has significant advantages engendered through its material properties. Let us start with the base material which forms the basis of MEMS and electronics as a whole. Silicon like many other materials reacts with oxygen and forms a very stable and high quality dielectric, silicon dioxide (SiO_2). This ability to form a high quality dielectric is perhaps one of the most important properties that has enabled silicon to become the material of choice for integrated circuits. Silicon dioxide has a wide range of use in both IC's as well as MEMS.

Metals can also be used to create MEMS devices. While metals do not have some of the advantages displayed by silicon in terms of mechanical properties, when used within their limitations, metals can exhibit very high degrees of reliability. Different metals used are Aluminum (Al), Gold (Au), Copper (Cu), Titanium (Ti), Tungsten (W), Silver (Ag), Chromium (Cr), Nickel (Ni), Iridium (Ir), Molybdenum (Mo), Tantalum (Ta), and different other alloys. Different polymers are used for patterning to perform lithography. Different polymers used are polyimides, photo-resists, parylene, plastics, paraffin wax etc.

The other materials used in MEMS are Silicon nitride, Silicon oxide and other metal oxides as insulators, ceramics, poly-diamond, silicon carbide, glass. Silicon is not the only semiconductor used in MEMS; researchers have been working with other semiconductors such as gallium arsenide (GaAs) etc. Now let us move on to the micro-fabrication techniques.

2.2. *Micro Fabrication Techniques:*

These techniques are used to fabricate the MEMS devices. The different techniques will be discussed in detail as follows;

2.2.1. *Oxidation:*

Silicon like many other materials reacts with oxygen and forms a very stable and high quality dielectric, silicon dioxide (SiO_2). This ability to form a high quality

dielectric is perhaps one of the most important properties that have enabled silicon to become the material of choice for integrated circuits. Silicon dioxide has a wide range of use in both IC's as well as MEMS. At room temperature the silicon oxidation procedure is extremely slow. Therefore, high temperature process is used to facilitate silicon oxidation in a timely manner.

High Temperature Oxidation: In this type of oxidation process, the wafers are first cleaned and then placed inside a furnace whose temperature can be controlled accurately. Figure 2.1 shows the schematic diagram of the apparatus. A carrier gas, typically nitrogen mixed with oxygen, is blown through the furnace chamber. It is made of a Quartz tube and is in a system with heating elements which maintain the desired temperature. Oxygen is introduced into the furnace by the carrier gas using liquid or gaseous sources.

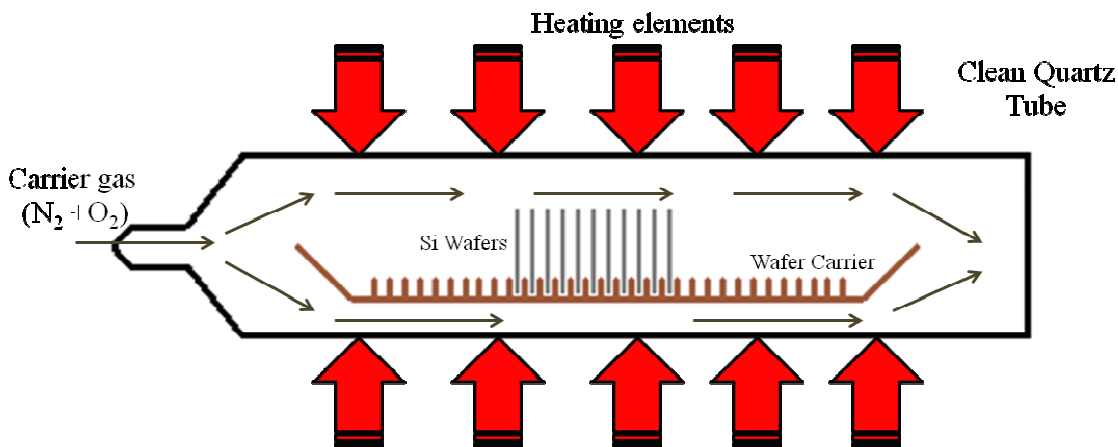


Figure 2.1: A schematic of the apparatus showing the high temperature oxidation procedure, the quartz tube maintains the clean environment and the temperature range of 900-1200 °C is maintained by the heating elements. A carrier gas containing N_2 and O_2 is introduced from one end. The Si wafers are placed in a wafer carrier boat.

As the carrier gas carries oxygen atoms through the chamber, it passes through the silicon wafers at high temperature. Oxidation requires that oxygen is constantly provided at the silicon oxide interface. As the oxide gets thicker, it takes longer for oxygen to reach the interface and the oxidation takes longer. As the oxide thickness increases, the arrival of oxygen at the oxide-silicon interface takes longer and the kinetics of oxidation change. As we can deduce from the name, oxidation is carried out at a high temperature environment. It is typically carried out at a temperature range of 900 to 1200 °C. Oxidation can typically take place under two conditions: dry ambient and wet ambient. In the dry oxidation process, the oxidation rate is usually very slow. This method is suitable for growing oxides in the range of about 10-100 nm. The oxide is a very high quality oxide and is usually used for making electronic devices. In the wet oxidation process, oxidation is performed in a steam environment. The growth rate is much faster than dry oxidation. Hence, the wet oxidation is used for growing oxides thicker than about 500 nm. The oxide is of a good quality, but a little less dense than the dry oxide and may have more pin holes. The oxide growth rate can be determined by using Fick's equations for diffusion. Figure 2.2 above shows the oxidation rates for wet and dry oxidation respectively.

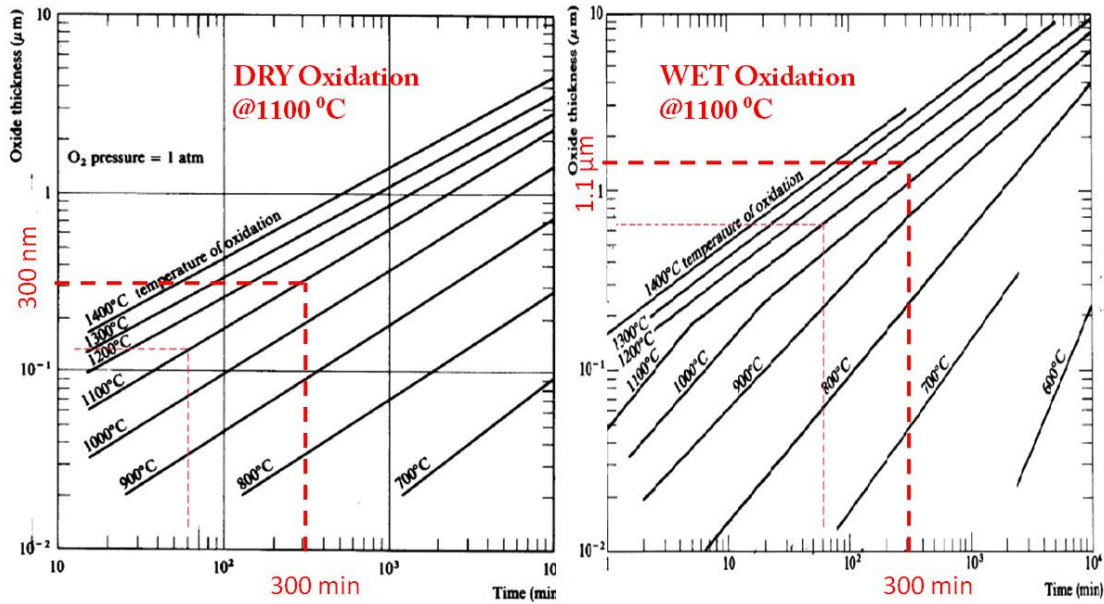


Figure 2.2: Oxide growth rate of (100) Si wafer in dry and wet ambience is shown. Higher the temperature, higher is the rate of oxidation in both cases. Wet oxidation has a higher rate of oxidation compared to dry oxidation. The above figure shows the oxidation at 1100°C for both environments. (Gandhi, 1994)

2.2.2. Film Deposition:

Thin films of any material can be deposited onto a substrate. These films can be used as masking layers or etch stop layers or can be a device requirement. This film deposition can be done in 2 ways; physical vapor deposition and chemical vapor deposition. Many materials can be deposited in thin film form by the process of physical vapor deposition. The material is placed in a vacuum chamber, and the material is transformed into a gas phase (using different techniques). Atoms of the material leave the source and land on the wafer which is known as the target. The molecular species of the material have to be in gas phase. Two standard techniques that can be used to create these

molecular species are; evaporation and sputtering. The physical vapor deposition is typically used to deposit most metals and some insulating and semiconductor films. It is most practical to deposit metal films using these techniques. By this technique, films ranging from 1 nm to several microns can be deposited.

2.2.2.1. Evaporation:

The material to be deposited is placed in a vacuum chamber, it is heated until it melts and evaporates. The gas phase molecules land on the target wafer and form the desired layer. The longer the deposition goes the thicker the film becomes. There are two types; thermal evaporation and electron beam evaporation. Thermal evaporation is the easiest of all and requires the simplest system. The film to be deposited is placed inside a crucible inside a vacuum chamber. The crucible is heated until the material evaporates. Heating of the crucible can be done in several ways, including resistive and inductive heating. The temperature required to evaporate the material depends on the vapor pressure of the material and on the pressure. Typically the vapor pressure of the material should be somewhere between 10 to 20 mTorr. The pressure inside the chamber typically ranges from 0.1-1 micro Torr. In e-beam evaporation, the material is heated and melted using a high energy electron beam. With this electron beam, higher temperatures can be achieved and hence, a wider range of materials can be deposited. With e-beam evaporation, refractory materials with low vapor pressure, as well as insulators such as oxides and glass can be deposited. The evaporation rate is higher at lower pressures.

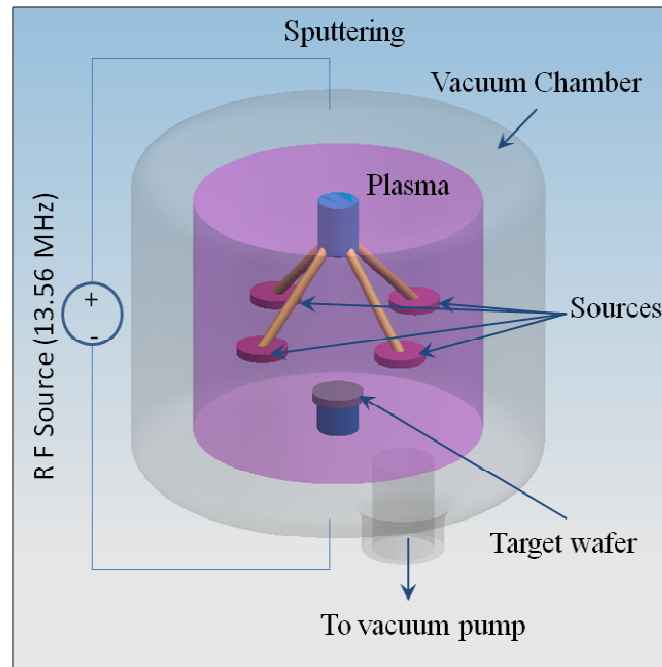


Figure 2.3: A schematic diagram of the experimental setup of Sputtering system. In this system, inside the vacuum chamber, there are multiple sources which can be used to deposit on to the target wafer. Plasma created in addition to the RF power bombards the source to knock off the atoms which deposit on the target wafer.

2.2.2.2.Sputtering:

This is another type of film deposition where RF plasma is used to bombard the atoms from the source and deposit them on the target. The plasma is generated by applying a RF voltage signal of 5-15 kV in a pressure range of 10-100 mTorr. Typically the plasma gases are inert gases; hence argon is used as the plasma gas. The plasma creates argon ions and electrons which bombard the source knocking off the source atoms. The source can be a substrate with SiO₂ deposited or also can be a metal substrate. Now these source atoms get deposited on the substrate which is the target. Figure 2.3

shows the schematic of the experimental setup of a sputtering system. A wide variety of materials can be deposited using sputtering, including metals, semiconductors and insulators. When deposited in a reactive environment with oxygen, oxides can be deposited. One can deposit multiple materials in a single pump down, as multiple sources can be placed in the same chamber. It is also possible to deposit alloys and compounds like silicides (MoSi, TaSi).

2.2.3. Photolithography:

Photolithography is a process in micro-fabrication which selectively removes parts of the thin film called photo-resist, to expose the bulk of the substrate. The first step in the lithography procedure is the spin coating of the photo resist. The photo resist is spun over the substrate at a particular speed, which is obtained from characterization results. This substrate is then kept on a hot plate at a certain temperature of about 90-100 °C. This process of heating up the substrate is called Soft Baking. Soft baking is a very important process step during lithography, as it plays a crucial role in the development of the photo-resist. The UV-light is used to transfer a geometric pattern from a photo mask to the substrate. The mask is typically made of a glass plate (soda lime or quartz glass) that is transparent to UV light. The pattern of interest is created on the glass using a thin metal film such as chromium or gold. The mask plate has the pattern of interest repeatedly printed on it. Mask polarity can be designed to either allow incident radiation pass through the field regions outside of the patterned areas or vice versa.

The photo-resist is a polymer whose chemical properties change when it is exposed to incident radiation, UV light. Note that the photo-resist cannot be exposed to temperatures beyond 200 °C as it will get burnt. The photo-resist can then be developed in a developer like the standard photographic process. Two different results can be obtained depending on the type of photo-resist used; positive photo-resist, and negative photo-resist. Figure 2.4 shows a schematic of the lithography process.

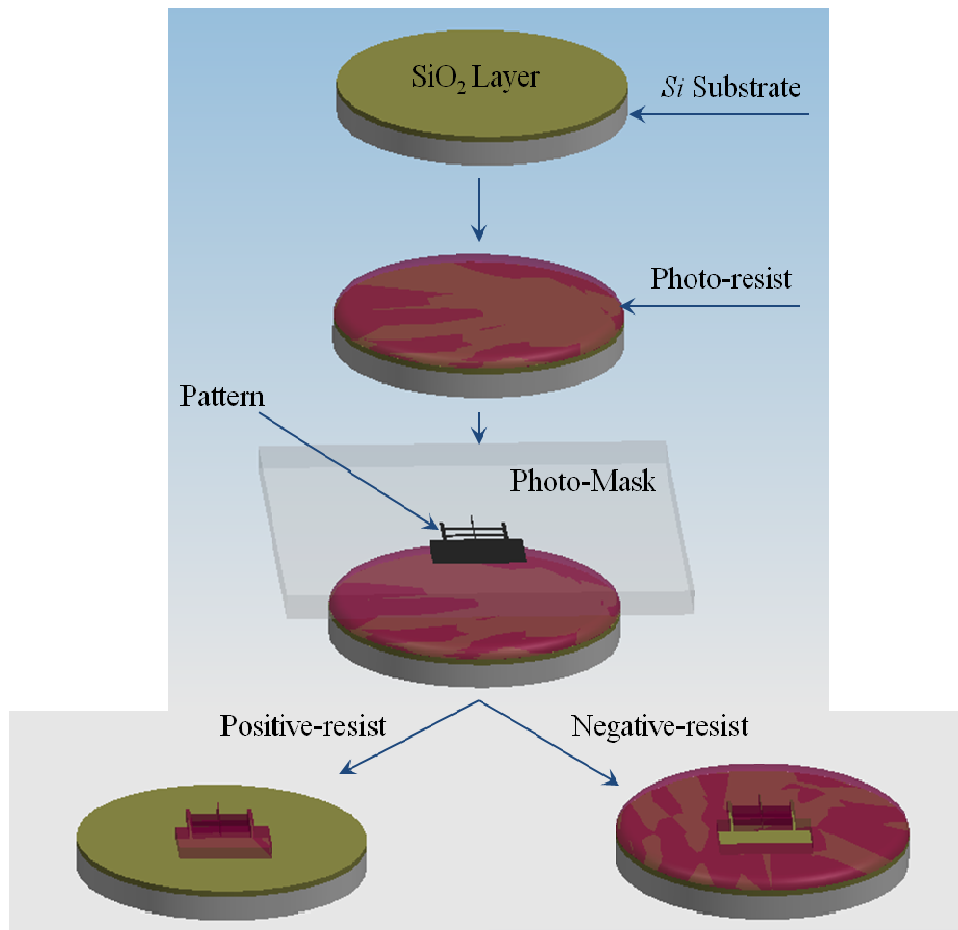


Figure 2.4: Schematic of Photolithography process, showing the effect of positive and negative photo-resist after developing the polymer.

Positive photo-resist gets etched away in the developer solution only in the areas that have been exposed to UV radiation. Negative photo-resist gets hardened and hence cannot be removed in the developer solution in the areas that have been exposed to UV radiation. The photo-resist is typically in a liquid state that can be spun onto a silicon wafer at speeds of a few thousand rpm's. The spinning process creates a uniform film thickness in the range of 1-10's of microns.

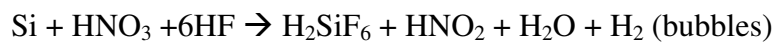
2.2.4. *Silicon Etching:*

“Etching and cleaning processes are involved at many points in the micro-fabrication process. The term etching is used to describe all techniques by which material can be uniformly removed from a wafer as in surface polishing, or locally removed as in the delineation of a pattern for a micro circuit. It also includes chemical machining of a semiconductor as part of the fabrication process, as well as the delineation of surface features such as defects.” (Ghandhi, VLSI Fabrication Principles - Silicon and Gallium Arsenide (2nd Edition), 1994)

After the deposition of a given thin film material and the development of the photo-resist image, the image must be transferred to the thin film. This can be done by wet chemical etching or by dry etching. The photo-resist acts as the masking material during the etching of the thin film material. Therefore, whatever etchant is used, the photo-resist must be capable of withstanding attack by that etchant. After the completion of etching, the photo-resist is removed and the process of photo-lithography and pattern

transfer onto the next thin film is repeated. As the feature sizes, i.e. the smallest dimension of a pattern, get smaller, the pattern transfer from the photo-resist to the thin film should be more accurate. Depending upon the etchants, the selectivity is different for different etchants. Selectivity is the etch rate of the intended film versus the etch rate of the masking material. Different important properties of the etchants other than selectivity are uniformity, etch rate, etch profile, and reproducibility. Ideally, the pattern on the photo-resist should be perfectly transferred to the thin film being etched. However, this does not happen partly because the photo-resist can be etched during the etching process, and partly because of the nature of the etching process.

The etching process can be classified in different ways. Depending upon the nature of the etching process, it can be classified as **Isotropic** and **Anisotropic** etching. In Isotropic etching, the material etches at the same rate in all directions. This is undesirable in most situations, as there will be considerable reduction in the feature size, line width, and especially as the thickness of the film becomes larger. This type of etch removes n-type or p-type silicon in all directions at about the same rate. Etching does depend on agitation, more the agitation during etching; larger is the undercut under the masked regions. Etching is carried out in a beaker where nitrogen bubbles are introduced to facilitate the transport of etchants and by products to and from the wafer. The equation below shows the chemical reaction during etching.



Anisotropic etchants are desirable because one can transfer the exact pattern and dimension of the photo-resist onto the thin film material. The etching follows a direction of the atomic arrangement of the material and can etch away only the desired parts. Mask erosion is another important and one should select masking materials, such as the photo-resist that can withstand the etchants for the length of the time needed. One of the commonly used anisotropic etchant constitutes a mixture of 44 wt% KOH in water. The use of isopropanol alcohol in addition to water and KOH reduces the etching rate of silicon dioxide masks. This however will change the etch behavior to make the (100) planes etch at a rapid rate than the (111) planes. As there is a problem of alcohol evaporating, a condenser is required to avoid this evaporation process.

A number of etchants etch silicon at different rates along different crystal orientations. These etchants are referred to as the orientation dependant etchants because they etch the different crystallographic planes of silicon preferentially, ie at different rates.

Miller indices: Figure 2.5 shows the miller representation of the three primary planes [(100), (110), and (111)] in silicon. (xyz) values are the inverse of the coordinate of the intercepts of a given plane with three axes. For example, (100) plane represents the plane that intersects the x-axis and runs parallel to the yz plane. [xyz] is a given crystal direction of the vector perpendicular to the plane (100).

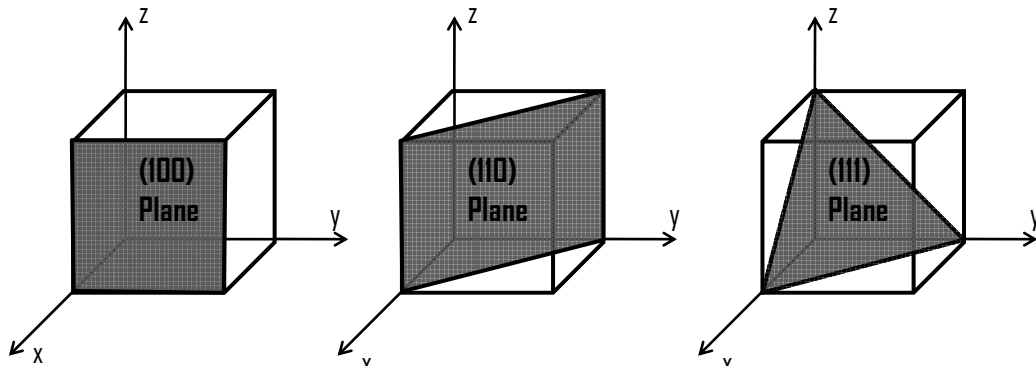


Figure 2.5: Figure shows the crystallographic planes and their orientations. The silicon wafer is oriented with respect to these planes.

It is believed that anisotropic etching occurs because these different planes represent a different density of silicon atoms to the etchant as the respective plane is exposed. In addition, the atoms at the surface for each plane have different number of dangling bonds. Dangling bonds are the bonds which are not complete. It is easier for the etchant to etch the plane with the higher number of dangling bonds. Those planes with higher number of dangling bonds will etch faster because the silicon atoms are more weakly bound to the rest of the lattice. Based on this, the etch rates of the three primary planes are as follows:

$$(111) \ll (110) \ll (100)$$

Figure 2.6 shows the anisotropic etching of a (100) silicon substrate using a mask, which may be silicon dioxide or silicon nitride. The etching takes place following the 54.7° (111) plane.

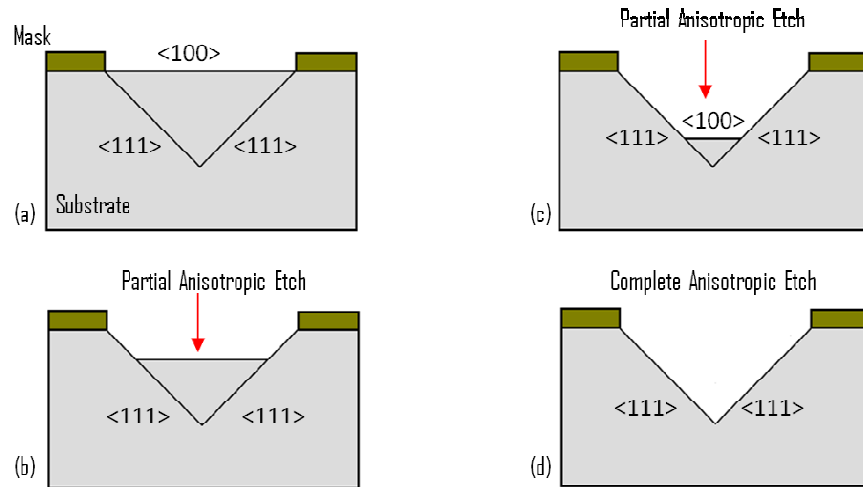


Figure 2.6: Schematic of an anisotropic etch process. Here the etchant etches the silicon atoms on the (100) planes and does not etch the atoms on the (111) planes due the selectivity ratio.

There is an interesting phenomenon which occurs during the anisotropic etching. When the mask which supports the pattern on the substrate contains exposed corners as shown in the Figure 2.7, after a while of etching, the etchant starts to etch the (111) planes also and there occurs undercutting beneath the mask. After a while the whole of silicon substrate beneath the exposed mask etches away.

Depending upon the method or etching process, it can be classified into two approaches; **wet chemical etching** and **dry plasma etching**. Wet chemical etching is a quiet straightforward and common method of etching in micro-fabrication. A variety of wet chemicals are used to etch the most common materials used in micro-fabrication, some typical etchants include the following; Buffered hydrofluoric acid (BHF), hot phosphoric acid, phosphoric acid, acetic acid, nitric acid and hydrochloric acid.

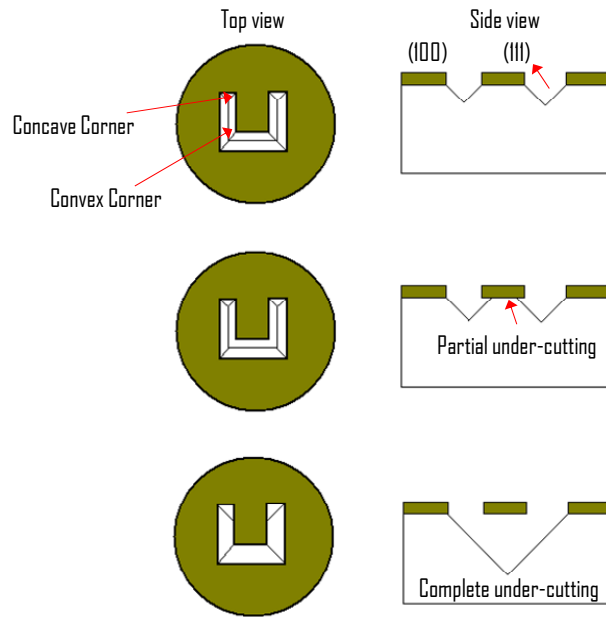
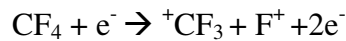


Figure 2.7: Shows the schematic of the anisotropic etching in the exposed corners of the mask. When the substrate is kept in the solution for a longer time, then the planes along the convex corners of the mask will etch first instead of the concave corners.

These chemicals can be made into a mixture and used as etchants for etching different materials. Although wet chemicals are commonly used as they offer a high throughput, very good selectivity, and low cost, but the disadvantage of these wet chemicals is that they are typically isotropic in nature. Their isotropic nature leads to lateral undercutting which becomes significant when the thin film thickness becomes larger.

Dry plasma etching is another chemical etching technique which employs gases instead of liquids. The gases are ionized in an RF glow discharge (plasma) and the specific chemical species are used to etch the thin films. The gases used to create the plasma determine the etch rate, etch profile and the selectivity. Many gases are used to

etch different thin films. One of the main disadvantages of dry plasma etching is that it has the worst selectivity with respect to both the mask which is typically photo-resist, and to the other layers. In today's research world, dry etching has become very popular and has its own place. Some of the gaseous etchants are; CF_4 , SF_6 , CHF_3 , CF_4/O_2 , BCl_3 etc. Many of these etch gases involve the radicals of fluorine and chlorine. For example, both silicon nitride and poly-silicon can be etched using CF_4 plasma. The basic reaction is:



Hence, it is possible to etch a variety of thin films, including di-electrics, metals, semiconductors, using variety of gases. Dry etching has become a routine and irreplaceable step in the fabrication of MEMS devices and IC's. There are three main types of dry etching techniques; plasma etching, reactive ion etching (RIE), and reactive ion beam etching (RIBE).

Plasma etching: Plasma etching is primarily a chemical etching process with minimal directionality which means that it is isotropic in nature. In this technique, many of the gases mentioned previously are used. In these systems, the wafers are placed on a platter which is grounded. So, when the plasma is created, the wafers get exposed to the various species and get etched. The etch rates obtained are quite fast; the process is quite simple and relatively easy to use.

Reactive Ion Etching (RIE): The reactive ion etching has the same basic setup as the plasma etcher, except that in this case the sample is placed on an electrode that is driven by the RF signal. RIE can be accomplished by replacing the neutral gas in a RF sputtering system by one or more chemical species. Plasma interactions with these chemicals result in the production of both neutral and ionized energetic species which can etch the substrate. The vacuum chamber is grounded and the systems use a lower pressure than the plasma etchers. These two effects lead to voltages of about 20-500 V at the wafer surface. Because of this higher voltage, the ions achieve a much higher energy as they approach the wafer surface and bombard it. Therefore, the RIE involves both the chemical and physical etching which results in very anisotropic etch profiles. The etch rate and sometimes etch selectivity take a hit during RIE. It becomes difficult to control the etch rates and the etch selectivity during RIE.

RIE is dry plasma etch in which the substrates are etched with the help of gases such as CF_4 and SF_6 , and also RF power which generates the plasma. Here, the substrates are placed at normal position to the gas flow, and are immersed in plasma. In addition, they are normal to the RF field, so that the movement of the ionized particles is both highly directional and rapid. Due to this, a high degree of anisotropic etching will occur. This anisotropic nature can be improved by using chemicals which have reaction products with large ionized components. There is another technique which can be used to enhance the anisotropic nature of the etching. This process is known as Scalloping. In this process, special gas chemistry is utilized to form a polymer on the sidewalls of the trench as it is

being etched. This gas chemistry is known as passivation gas. This thin layer of polymer prevents lateral undercutting and etching of the Si on the side walls resulting in a high aspect ratio etch. Figure 2.8 shows the schematic of the scalloping process. Tetra fluoro methane (CHF_3) is the most commonly used gas for this scalloping process.

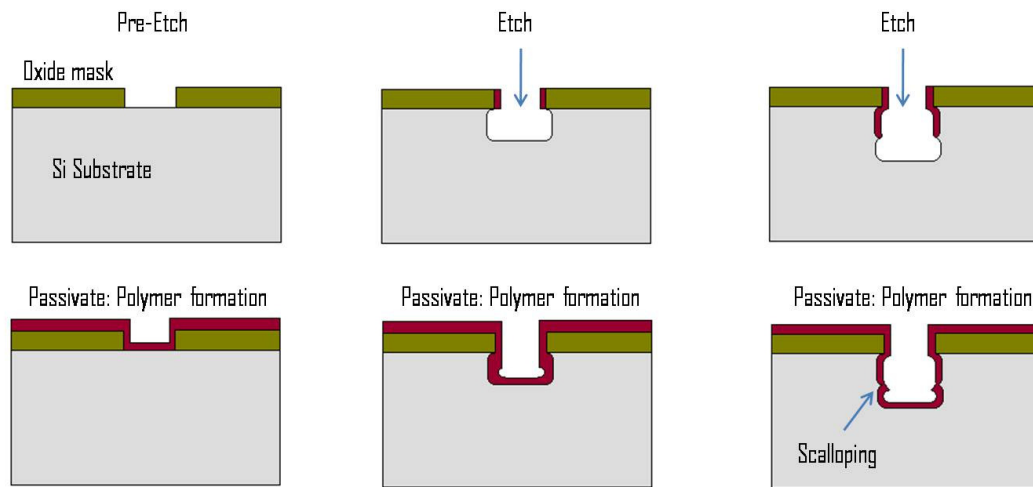


Figure 2.8: Scallop process explained step by step. The passivation after etching improves the anisotropy of the etching. This tends to prevent any undercutting during the RIE etch.

2.2.5. Etch Stops:

The isotropic and the anisotropic etching techniques discussed above are not very easily controlled to fabricate microstructures of specific and desired thickness. Often, it is a necessary step in micro-fabrication to maintain a constant depth. To do this it becomes important to control the etching. Etch stop is a technique where the etching stops abruptly. There are several etch stop techniques including doping which is concentration dependant, electrochemical etch and dielectric etch stop. These etch stops allow one to

Chapter 2- Introduction to MEMS Technologies

control the thickness of a microstructure accurately, and have a very uniform etch thickness.

Concentration dependant silicon etching: most anisotropic etchants have an etch rate that is also dependant on the doping concentration of the substrate. This doping dependence can be used to advantage to fabricate different microstructures. The microstructure of interest can be doped using diffusion or ion implantation to the desired thickness, and then the lightly doped silicon regions can be etched. High concentration boron doped layers can be formed in silicon using several techniques:

- High temperature diffusion using the solid and gaseous sources.
- High temperature diffusion using spin on glass sources.
- Epitaxial growth
- Low temperature ion implantation.

The most common dopant used in this purpose is boron. Concentrations of $2 \times 10^{20} \text{ cm}^{-3}$ at depths of 10-15 microns can be achieved. The disadvantage of this technique is that the concentration needed to achieve such etch stops is very high which will not allow the formation of electronic devices in the materials that are highly doped.

Electrochemical etch: In this technique, instead of creating a highly doped layer, one can simply form a pn-junction diode and use the unique characteristics of the diode to force the etchant to stop at a certain location. When silicon is electrically biased with

respect to the etchant such that its voltage is positive anodic with respect to the solution, an oxide layer is formed on it and this oxide layer can prevent further etching. At a negative bias with respect to the solution, silicon will continue to etch. This feature can be used to create an etch stop.

Di-electric etch stop: in this case, an insulator layer is deposited on the silicon wafer. This insulator layer is usually silicon dioxide. This oxide layer acts as an excellent etch stop because it does not etch appreciably in etchant like KOH or EDP. The thickness of the silicon on top of the insulator can be controlled very accurately with better than 5% uniformity. These wafers are called silicon on insulator (SOI) wafers.

2.2.6. *SCREAM Process: Single-Crystal-Reactive Etched And Metallization*

This process was developed at Cornell University. This method can be used for multiple purposes. It can be used to create the cantilevers and release the beams, and can also be used to create electrodes by depositing a metallic layer after the etch is complete. A silicon wafer is taken and a thermal oxide is grown on top to act as a mask. Figure 2.9 will explain the process clearly.

After the oxide layer is grown, the wafer is patterned with photo-lithography. Once the pattern is on the wafer, the wafer is etched with RIE to achieve the anisotropic nature of etch. Another layer of oxide is grown after the RIE etch. This layer of oxide is to protect the sidewalls of the device.

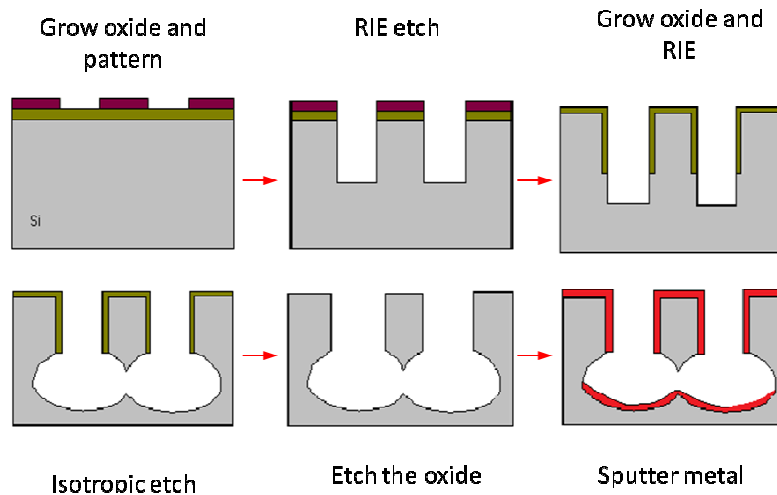


Figure 2.9: Step by step micro-fabrication process explaining the SCREAM process.

Another RIE is performed on the sample so as to etch away the oxide on the bottom of the pit to expose the silicon substrate. Now once the silicon is exposed and oxide mask is present to protect the sidewalls, isotropic etching is carried out to carry out the undercutting and to release the beams or the features. If required, a metal layer is sputtered. This is the SCREAM process to release the beams.

With this introduction to MEMS, we move on to the next chapter. The next chapter discusses the recent developments in the MEMS field. Various MEMS devices that have been developed for mechanical and electrical testing of materials and biological cells will be discussed.

Chapter 3

MEMS Devices for Materials Testing and Cell Mechanics

This chapter discusses the recent developments in the field of MEMS for materials and life sciences. It is known that nano-scale material properties cannot be extrapolated from the bulk values since materials behavior is different in micro and nano-scale. (Haque et al, 2002) It is therefore of particular relevance to accurately evaluate the mechanical properties of such nano-structures. Advances in the field of nano-technology have shown that very high-resolution sensors are required to perform the tests and obtain results. As material systems, the living organisms are much more complicated than engineering materials. They perform many complex functions such as control of metabolism, sensing, communication, growth, and remodeling. Living cells can sense mechanical forces and convert them into biological responses (Bao et al, 2003). Extensive research has been taking place which show the relation between mechanical responses and biological functions of a single living cell. This research has improved the diagnostic quality and the treatment processes of orthopedic, cardiovascular and respiratory diseases.

Many researchers around the world have been showing keen interest in the development of the MEMS technologies for determining the mechanical properties of different nano-materials, thin films, and bio-materials. In today's world of science and

technology, the most commonly measured mechanical quantities are force and displacement. Devices are being developed to measure these quantities for performing a variety of tests in engineering applications. Irrespective of the type of application, force (F) is always measured as the product of the stiffness (K) of the probe (usually a mechanical structure) and the measured displacement (x) of the probe ($F = K*x$). In order to achieve higher force sensing resolution, either we need to reduce the stiffness of the probe or have to employ very high-resolution displacement sensors. To be able to apply in the field of nano-technology and cell biology, we require techniques capable of measuring the properties of nanostructures and living cells. This task is quite challenging as the requirement is the load and displacement resolution in nanometer scale.

This chapter critically reviews some of the MEMS based testing devices that have been employed to perform mechanical tests on nano and bio materials. The materials include poly-silicon, bulk aluminum, carbon nano-tubes and biological cells. These MEMS devices can be integrated to microscopy setups including AFM, SEM, TEM and optical microscopy allowing imaging. Each device consists of three components: force sensor, actuator and the specimen holder. Section 3.1 in this chapter discusses about the different MEMS devices in the field of material testing. It describes the main contributions and results of the experiment performed, giving details of the force sensing technique and the unique actuation system involved in each. Section 3.2 includes the different MEMS devices for cell mechanics and life sciences.

3.1. MEMS Devices for Material Sciences

This section mainly describes the unique idea of different MEMS devices for testing of different nano-materials such as nano-tubes, nano-wires, thin film membranes, of different engineering materials such as metals, etc. This section involves the unique force sensing system and the actuation system of each device.

3.1.1. First generation MEMS device for mechanical characterization of thin films.

Saif and Haque in 2002 developed the first generation experimental method for the mechanical characterization of freestanding thin films with thickness on the order of nanometers to micrometers. Figure 3.1 shows the SEM image of the device and shows a close up view of the specimen.

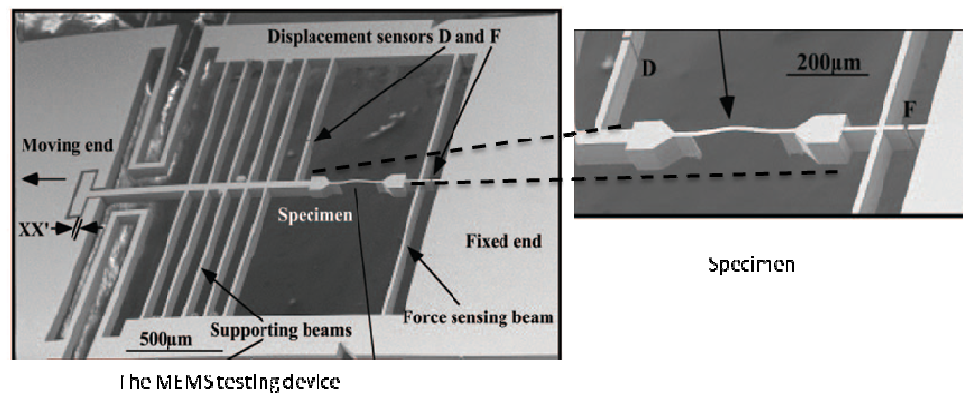


Figure 3.1: The SEM image of the device by Saif and Haque showing the moving end of the device, the U-spring for the structural stability, support beams, the force sensor beam near the fixed end, the displacement sensors D and F and the magnified image of the freestanding specimen, showing clearly the displacement markers. (Haque et al, 2004)

This method allowed the in situ SEM and TEM observation of material responses under uniaxial tension with measurements of both stresses and strains under a wide variety of environmental conditions such as temperature and humidity. This MEMS device consists of three components. On the actuator end, a piezo-actuator applies the load, at the center there is a specimen holder where the nano structure is placed, and at the force sensing end, there are displacement sensing beams which measure the deflection as the load is applied. The force sensing and the actuator mechanism will be discussed further in this Section. Using this MEMS-device with a force-resolution of 18.2 μN , changes in the characteristics of the aluminum polycrystalline material at the nano-level were found. The specimen was loaded by applying voltage to the piezo actuator. From Figure 3.1, the displacement sensors D and F measured directly from the SEM observation. Figure 3.2 shows the stress strain plot for the 200 nm thick aluminum film. The residual stress was found to be 69 MPa, which is well below the yield stress. The specimen yields at 330 MPa which is about 33 times the bulk value for aluminum, and this clearly reflects a significant strengthening at the nano scale.

The most attractive feature of this technique is that it demonstrates the feasibility of in situ experimentation inside the chambers such as SEM and TEM. An advantage of this design is that the total force and resolution requirements can be varied by varying the dimensions of the sensor such as the width and depth of the force sensing beams. It addresses the commonly encountered problems of pre-loading, gripping and misalignment of the specimen by making the test purely uniaxial.

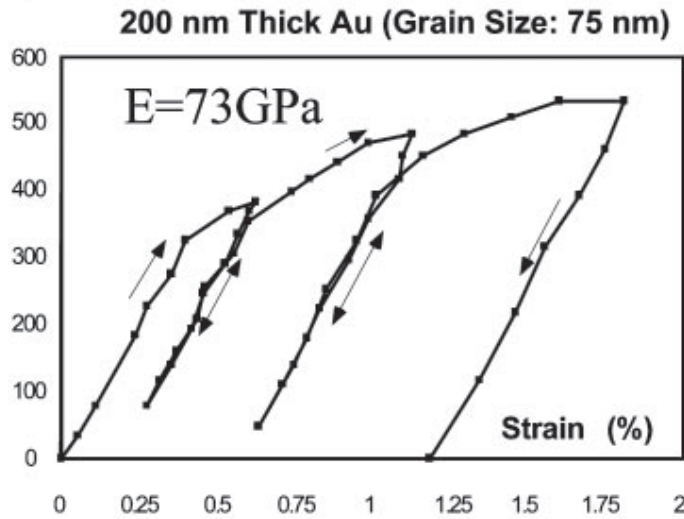


Figure 3.2: The stress strain relationship tested by Haque and Saif, for a 200 nm aluminum thin film. Here a cyclic loading was employed to test the specimen. (Haque et al, 2004)

There were some disadvantages of this device. This device could not perform electrical characterization. Furthermore, it had a high probability of sample failure during fabrication and the force sensor could only be calibrated by cleaving the stage after sample testing. Now let's move on to the next generation of the MEMS device.

3.1.2. Second generation MEMS device for mechanical characterization of thin films.

The first generation device discussed above could perform mechanical characterization, but failed to perform electrical characterization. The second generation of the MEMS device designed by Han and Saif in 2006, had a similar design to the first device, but could perform both mechanical and electrical characterizations of nano materials. The stress strain response of a 100 nm thick freestanding aluminum film is measured in the SEM, and by measuring the conductivity of the freestanding film at

different temperatures, the electrical characterization is demonstrated. The test performed resulted that the nano-grained metal conductivity may increase due to thermal annealing without the grain growth, and possibly by reorganizing of the grain boundaries. This new stage prevented sample failures and allowed calibration before the testing without cleaving and resistivity measurement of the sample at different temperatures (Han et al, 2006).

Figure 3.3 shows an SEM image of the device developed by Han and Saif. This stage operates as follows: the freestanding sample is attached at one end to the force sensing micro-beams (AB) as shown in Figure 3.3. The other end is attached to a series of support beams (CD), which helps align the loading axis with the specimen axis and ensures mechanical integrity of the stage. One end of the stage is held fixed, while the other end is pulled by an actuator such as a piezo-actuator if tested in SEM, or by a motor in TEM. A small gap (XX) between the support end of the sample and the stage protects the sample from undesirable loading during handling.

Thus, during the experiment, the stage has to be pulled to first close the gap (XX) and then to strain the sample. The U beams correct any misalignment error in loading by five orders of magnitude. As the stage is deformed by an external actuation, the sample is strained and the force sensing beams (AB) get deformed. The force on the sample is obtained from the change in the gap, G_1 , and the spring constant of the force sensing

beams calibrated by nano-indenter. The stretch in the sample film is attained by subtracting the displacement change in G_1 from the change in G_2 .

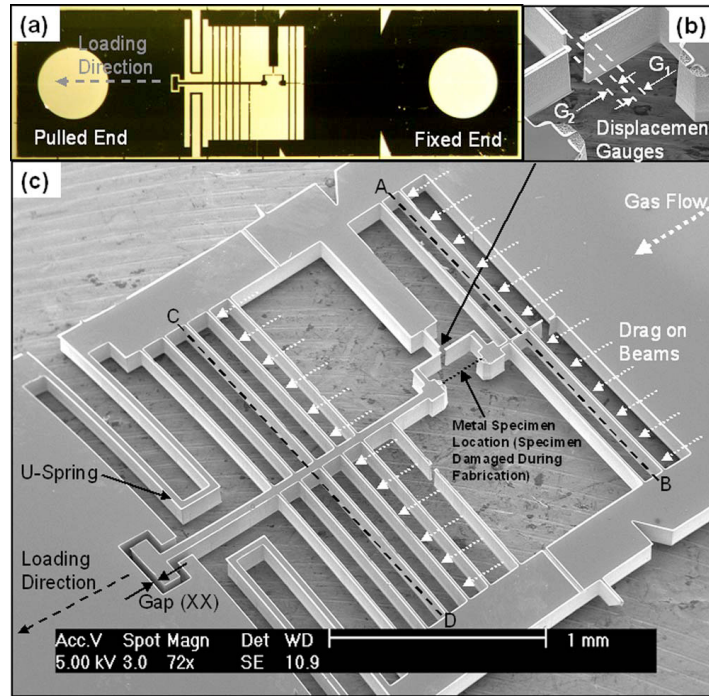


Figure 3.3: The MEMS testing device by Han and Saif, (a) Optical micrograph of the whole device, where the fixed and the pulled ends are clearly visible and the loading direction is shown. (b) Magnified view near displacement gauges. (c) Components of the stage subjected to possible drag force due to gas flows in the ICP chamber shown by dotted arrows. (Han et al, 2006).

It was observed that, most of the freestanding thin film specimens failed after the ICP-RIE process of the Si wafer. The gas flow in the RIE chamber induces drag forces on the stage which sets it to dynamical motion. The Figure 3.4 shows the stress-strain curve which is plotted during the experiment. This device is fabricated by using micro fabrication techniques and is applied to test a 100-nm thick freestanding Al sample. The stress-strain response of the sample shows an elastic modulus of 61 GPa. The room

temperature resistivity of this nano-grained specimen is almost 20 times higher than the bulk value. The resistivity decreases irreversibly with increasing temperature. It also decreases with time without any significant grain growth. Upon cooling the resistivity increases with the decreasing temperature, contrary to bulk metallic behavior.

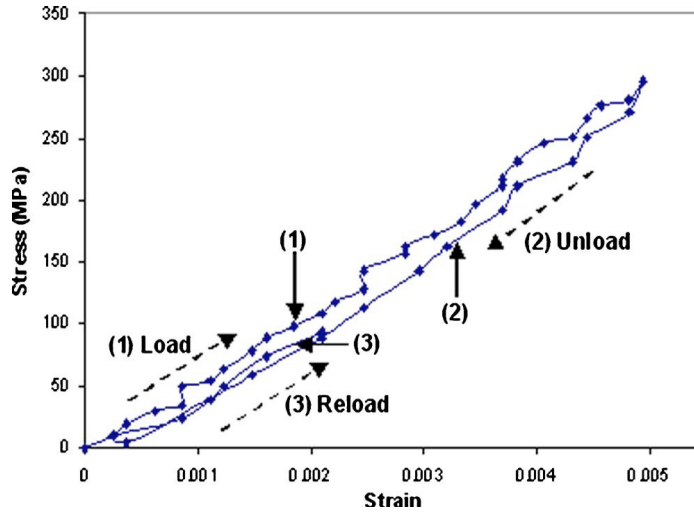


Figure 3.4: Result of uniaxial tensile test by Han and Saif (2006) on the Al specimen that is 810 μm long, 13 μm wide and 100 nm thick, having an average grain size of 65 nm. Here, first loading is done then it is unloaded, then reloaded. The points 1, 2, 3 show the states where the resistivity at room temperature prior to annealing, resistivity decreases, resistivity increases with cooling respectively. (Han et al, 2006)

3.1.3. MEMS-device based on Force Capacitance

In the above two designs, it is observed that the deflection of the force sensor beams are observed and measured. The device, which is described below, gives an electrical output, offers the possibility of continuous observation of the specimen deformation and fractures with sub-nanometer resolution, while simultaneously

measuring the applied load electronically with nano-Newton resolution. Espinosa and Zhu in 2007 described the design, fabrication, and operation of a novel MEMS-based material testing system used for *in situ* tensile testing of nanostructures. Including SEM and TEM, the device could also be employed to perform *in situ* testing in scanning probe microscopes and synchrotron X-ray nano-diffraction stages. The overall device performance was demonstrated by testing freestanding co-fabricated poly-silicon films and multi-walled carbon nano-tubes (Espinosa et al, 2007).

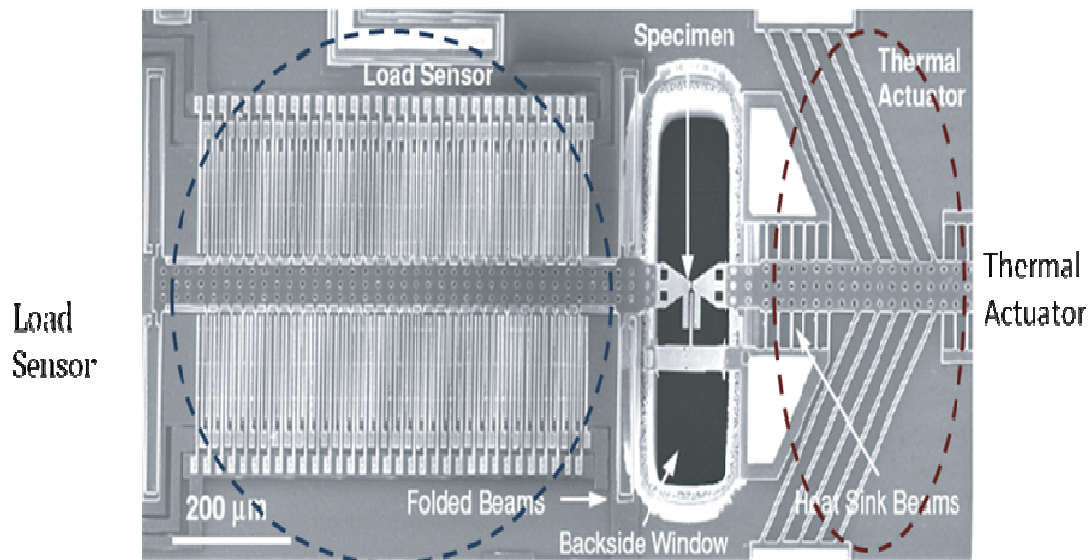


Figure 3.5: The MEMS based testing device, by Zhu and Espinosa (2007), which shows a capacitive load sensor, a thermal actuator, and a gap for the placement of the specimen. The specimen is kept freestanding with the help of a *backside window*. The thermal actuator also has the heat sink beams which restrict the heat from reaching the specimen. (Espinosa et al, 2007)

This device consists of three components: a thermal actuator that applies load on the specimen by the principle of thermal expansion, a specimen holder, which is

fabricated along with the device. This specimen holder contains a backside window. The Figure 3.5 shows the device structure where the presence of the backside window is very important as it makes the specimen freestanding and also allows the electron beam to pass. The Load sensor is the third component of this device, which uses a comb drive capacitor principle to sense the force. Figure 3.6 shows the testing of MWCNTs on the device by Zhu and Espinosa. There were some tests performed on 5 different specimens and the load displacement curve is shown in Figure 3.6a. This device achieved resolutions of 0.05 fF in capacitance, 1 nm in displacement, and 12 nN in load.

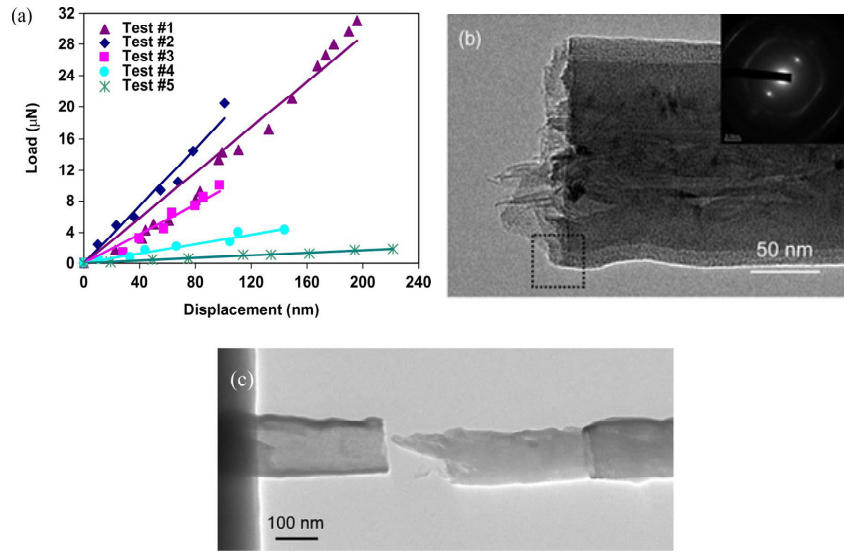


Figure 3.6: Results from the device by Zhu and Espinosa. (a) Load-elongation measurements corresponding to CVD-grown MWCNT specimens tested under various irradiation conditions. Note that specimen #1 does not possess the highest stiffness despite being exposed to the highest Ga ion irradiation because its length is about twice that of specimen #2. Its stiffness is the highest if normalized by the length. Refer to Table II for the maximum load and displacement. Test #6 is not plotted because it failed prematurely, likely due to heavy ion and electron irradiation. (b) Typical fracture surface of an MWCNT subjected to ion beam irradiation showing failure of the entire cross-sectional area (Test #1). (c) Typical fracture surface of an MWCNT subjected to e-beam irradiation at 200 kV, showing telescopic failure with multiple-shells broken (Test #4) (Espinosa et al, 2007)

Another important feature of the developed device is the capability of electronically measuring the load as well as the average specimen deformation. The working principle of this device is based on the force sensing technique and the actuator mechanism which is discussed in the following sections of this chapter.

3.1.4. Pico Newton Load Sensing MEMS Device based on Beam Buckling.

This device developed by Samuel and Haque in 2006, showed an interesting technique which involved displacement amplification to sense the deflection of the specimen. This device exploited the non-structural mechanics of two post buckled slender silicon columns to achieve ultra low stiffness. Figure 3.7 shows the MEMS force sensor.

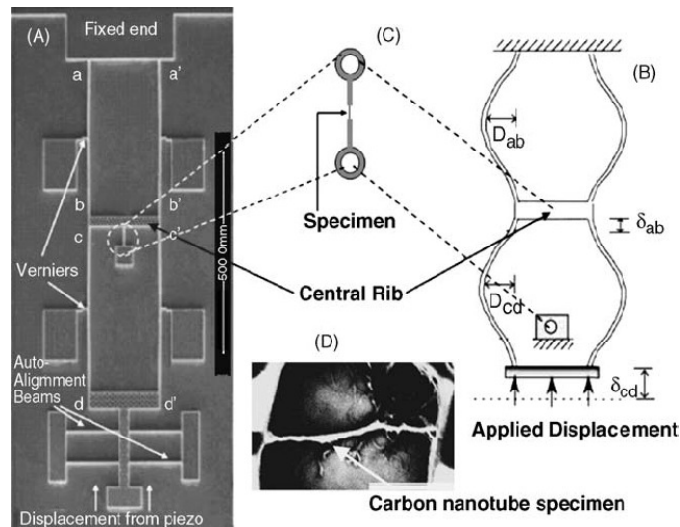


Figure 3.7: MEMS based testing device by Samuel and Haque. (A) SEM micrograph of the device showing the 2 pairs of columns the calipers which measure the displacement the auto alignment beams; (B) schematic of the buckled device after the displacement is induced, showing the change in displacement which measures the eventual force; (C) schematic of specimen fixture showing that one end of the specimen is fixed and the other end is moving connected to the central rib; (D) freestanding carbon nanotube specimen. (Samuel et al, 2006)

This was for the first time; displacement amplification was used concomitantly with stiffness attenuation in the post buckling domain. This sensor can be used to perform different, qualitative and quantitative measurements inside different microscopy instruments such as SEM, TEM and STM. This sensor can be used to characterize the carbon nano-tube polymer interfaces, nano-scale thin testing, mechanical testing of thin film biological cells etc. The loading technique utilized could be differential loading of two small stiffness structures which can be used to obtain very high force resolution, on the order of nano-Newton, and pico-Newton range (Samuel et al, 2006).

One of the most significant aspects of this design is that post-buckling mechanics inherently results in the amplification of axial displacements, which thereby allows us to achieve pico-Newton force resolution, even though the measured displacements as shown in Figure 3.8, are in micrometer range. The unique sensor design allows it to be integrated with virtually any form of microscopy (optical, fluorescence, electron and tunneling electron) and does not require any complex actuation or sensing mechanism, while still being capable of high resolution force measurements. The device performance is comparable to that of an AFM, only several orders of magnitude cheaper (due to MEMS batch fabrication techniques), much smaller and with a high degree of customizability afforded due to nanofabrication techniques.

The force resolution achieved by this device is close to 0.74 pN and a displacement resolution of about 25 nm is achieved even under an ordinary optical

microscope. Changing the geometry could vary the range and resolution of the device. The unique configuration of the structural members automatically results in finer resolutions for softer (biological, polymeric) specimens and coarser resolution for stiffer ones. This provided the sensor with a high degree of customizability, enabling it to be incorporated in a variety of experiments where conventional tools cannot be used. The purely mechanical nature of the device made it less susceptible to environmental conditions (such as electromagnetic fields and aqueous medium). This novel sensor design could also be implemented at the macro scale to measure/load forces with very high precision.

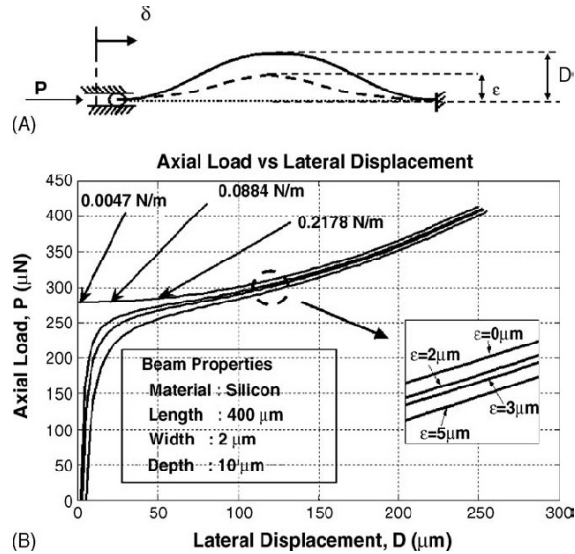


Figure 3.8: Results by Samuel and Haque. (A) Shows the post-buckling geometry where transition of the axial force to axial displacement to the lateral displacement which is measured is shown. ϵ is the initial buckle which is provided to maintain a unidirectional lateral displacement. (B) Shows the load displacement plot where the lateral displacement varies with the axial load for different values of ϵ . (Samuel et al, 2006)

3.1.5. MEMS device for Indentation testing of freestanding nano-films.

Leseman and Mackin in 2007 developed a novel tool for the mechanical characterization of axisymmetric freestanding films. The main objective was to devise a fabrication system to produce freestanding films and developing a reliable testing method for these thin films. Considering this purpose, calibrated MEMS based load cell with a spherical loading tip and a positioning system capable of sub nano-meter accuracy was designed. Figure 3.9(a) shows the typical load cell designed by this group. As shown in the Figure 3.9(b), loading tip is connected to a fixed-fixed beam at the midpoint. The load cell is calibrated using a novel approach that allows accurate load measurements during testing. The fixed-fixed beam with its loading tip was pressed into an axi-symmetric freestanding thin film membrane with a calibrated piezoelectric stage. A double fixed-fixed beam configuration was used to counteract any misalignments in the load tip and to limit rotations in and out of the plane of the load cell. Deflection of the beam, and thus the load applied to the membrane, was read from a co-fabricated vernier scale on the load cell while the displacement field of the membrane was measured from interferometric images of the membrane. (Leseman et al, 2007). The films analyzed were freestanding Gold films. The main advantage of this technique according to them is that, it allows us to perform multiple experiments with a single load cell, at resolutions better than 50 nN on films with defects, and with potential to operate in a liquid. The working principle of this MEMS load cell is explained in the further sections of this chapter. The devices

discussed until this point describe different techniques of testing the mechanical properties of nano-structures, and thin-films.

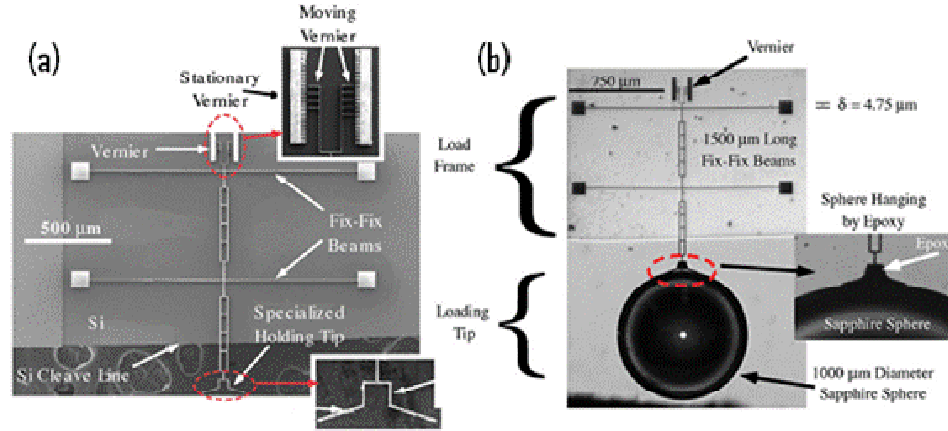


Figure 3.9: Design by Leseman and Mackin. (a) An SEM image of a MEMS-based load cell. This image shows two single crystal silicon fixed-fixed beams, a vernier for measuring vertical displacements the magnified view is shown as a microscope is present to view the readings, and a testing tip (specialized holding tip) with two key design components: first is a lamp-shade like structure to which we attach a 300 μm diameter sphere; second is a structure that allows for a controlled wicking of liquids. (b) Shows the complete system with the 1000μm ball lens epoxied to the tip of the load cell. (Leseman et al, 2007)

3.1.6. MEMS Devices for Mechanical Testing of One-Dimensional Materials.

The MEMS device described here allows tensile and bending tests on individual carbon nano-tubes inside a TEM. Direct tensile testing of individual carbon nano-tubes has been onerous due to their dimensions. Micro-fabrication techniques were employed to develop a tensile testing stage for this purpose. This device enables a direct application of tensile strain to individual nano-tubes while being viewed under a TEM. The resolution and contrast mechanisms of the TEM are essential in detecting defect

structures and lattice deformation, as well as for accurately measuring tube dimensions, which are on the order of the nanometer scale, a combination which neither atomic force microscopy (AFM) nor scanning electron microscopy (SEM) can match. (Demczk et al, 2002)

Different tests were performed using this stage, which included tensile pulling experiments. Based on their observation of the force required to break the tube, a tensile strength of 0.15 TPa was observed. From corresponding bending studies on such nano-tubes, the Young's modulus was estimated to be 0.9 TPa. These results suggested a strength that was a large fraction of the elastic modulus, although previous measurements of their elastic stiffness have yielded higher modulus values, by as much as a factor of 2. The result does indicate that individual nano-tubes can fail as essentially defect-free materials. Furthermore, they observed no obvious reduction in cross-sectional area prior to the failure. In addition, the bending experiments revealed a remarkable flexibility in these tubes. These unique properties support the potential of nano-tubes as reinforcement fibers in structural materials.

Figure 3.10 (a) shows the micro fabricated tensile testing device with the springs; Figure 3.10 (b) indicates the TEM image of the MWCNT spanning the gap. Figure 3.10 (c) details the experimental setup. Initially the CNT were synthesized by arc discharge method. This process facilitated the testing of nano-tubes of tens of nm of length. This tensile testing device was then micro-fabricated; the specimen which is the carbon nano-

tube was adhered to the system by depositing gold films around the gap. The observations were conducted using videotaping. Figure 3.11 (a) shows a still micrograph of the nano-tube under test just prior to straining.

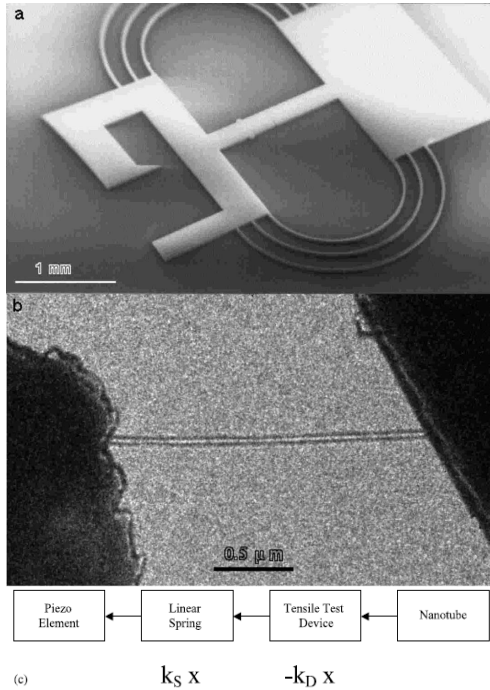


Figure 3.10: (a) The micro-fabricated nano-tube tensile testing device by Demczyk et al. (b) TEM image of a MWCNT spanning device gap. (c) Block diagram of the experimental setup. (Demczyk et al, 2002)

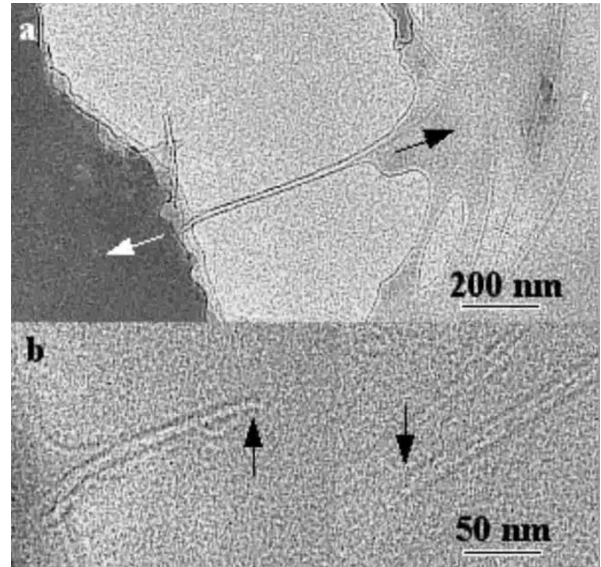


Figure 3.11: (a) Multiwall carbon nano-tube just prior to tensile testing. Arrows indicate direction of loading (white is actual pulling direction); (b) fracture surfaces of both ends of the tube after breakage. Note that rightmost end of nano-tube has moved vertically downward past another tube. (Demczvk et al. 2002)

Other research groups have proposed that, above critical elongation which is just before the failure, a 90 degree rotation of the carbon-carbon bond occurs which results in the dislocation dipole due to Stone Wales transformation (Nardelli, 1998), (Yakobson, 1997). Figure 3.11 (b) shows both ends of the tube after failure. There were multiple bending sequences observed as shown in the Figure 3.12, in which nano-tubes exhibited

remarkable flexural robustness which is not displayed by any other material. Simple cantilever beam theory was employed to obtain the Young's modulus of the specimen by approximating it to the cantilever beam in simple bending. The formula being:

$$E = \frac{PL^3}{3I\delta_{max}}$$

Where δ_{max} is the maximum deflection, I is the moment of inertia. With a load of 10.9 μN they achieved the Young's modulus as $E = 0.91 \text{ TPa}$ which seems to be consistent with the theoretical results.

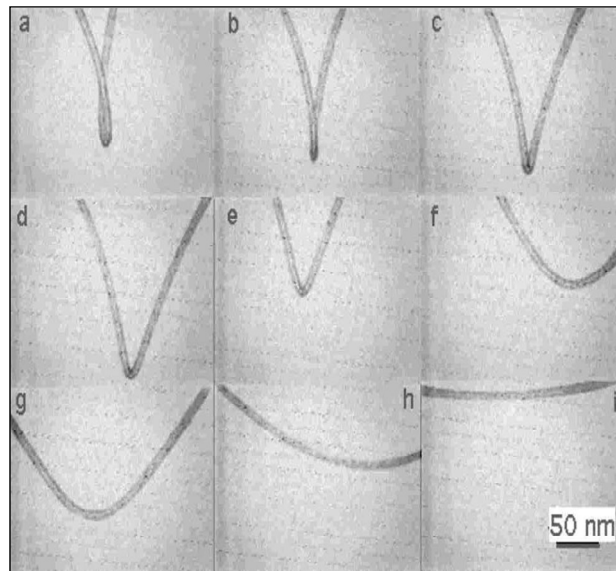


Figure 3.12: In-situ bending sequence on a single multi-walled carbon nano-tube. Note strain contrast at sharp bends (b–e) and the lack of the same in the straightened tube (i). (Demczyk et al, 2002)

Another group of scientists developed a different MEMS device which was used to obtain the elastic properties of a templated carbon nano-tube (Lu et al, 2006). The

templated-CNTs (T-CNTs) are known to be amorphous and probably contain hydrogen. This device constituted of an actuator system, direct force sensing beams, and integrated electrodes for di-electrophoretic deposition of nanostructures. During this test, an increasing tensile load was induced to the T-CNT by actuating the device and high resolution SEM images were obtained at different loading conditions. The results obtained included the load (from the bending of the direct force sensing beam), the elongation of the specimen during the loading, and the specimen geometry. A stress strain curve was fitted, which provided the modulus of 14.6 ± 4.6 GPa. Figure 3.13 shows the SEM image of the MEMS device developed by this group.

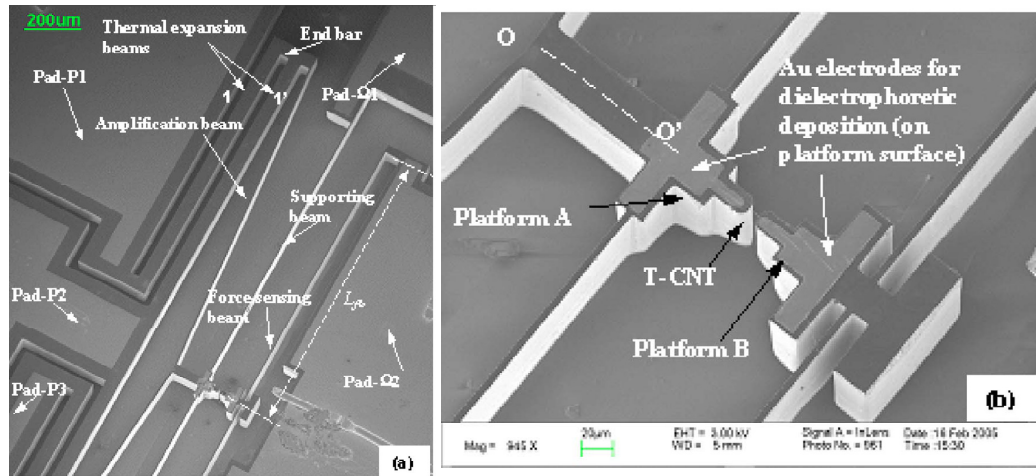


Figure 3.13: (a) SEM image of a MEMS-based testing device with direct force sensing beams. The end bar is free end of the thermal expansion beams. The amplification beam is the structure which results in the amplification of the deflection of the specimen. The pads shown are for electrical connections. The support beams are attached to the platform A to give stability. (b) Central area of the testing platforms, with a T-CNT

This device is designed in three parts of functionality: mechanical structure, electrical circuit and thermal path. The mechanical structure includes an actuation unit,

two supporting beams and force sensing beams. The electrical circuit has three parts; the contact pads for introducing the current to the substrate, the silicon structure as the Joule heating element metal electrodes (platform A and B) for electric field assisted deposition. The thermal path is created such that the heat is generated in the thermal expansion beams and dissipated to the large silicon base of the contact pads through the supporting beams. Due to the different complications involved with growing of carbon nano-tubes at high temperatures on MEMS devices, di-electrophoretic deposition was employed to assemble a single T-CNT on to the device by liquid dispersion (Lu et al, 2005). As we know that silicon is conductive in nature, electric field was applied between the electrodes. Platforms A and B in the Figure 3.13 acted as the electrodes. Electrical connections were made between the contact pads of the device. To perform tensile loading experiments, it was necessary to first clamp the T-CNT to the two platforms because the interaction between the T-CNT and substrate surface was not strong enough for loading the T-CNT. One method for making clamps was via electron beam induced deposition (EBID). In this process, the electron beam is used to decompose molecules and thereby deposit material on the surface exposed to the beam. Paraffin was used as a solid phased hydrocarbon to accelerate the clamping process. After a small amount of paraffin solution was pushed out of the nozzle of the glass fountain pen, the toluene evaporates immediately, leaving a minute quantity of paraffin deposit at the outer surface of the nozzle tip. Figure 3.14 shows a SEM image of the device with a template carbon nano-tube deposited and paraffin nearby and hence the clamp is fabricated.

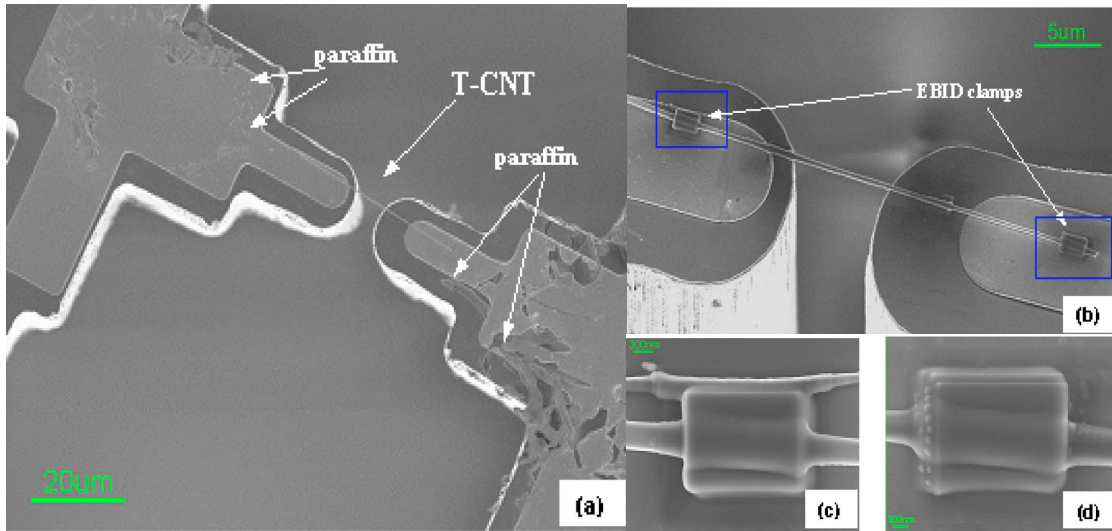


Figure 3.14: (a) A SEM image of a T-CNT deposited across the platforms before being clamped. Paraffin has been deposited close to each end of the T-CNT on each of the platforms. (b) The T-CNT after clamp deposition by the EBID/paraffin method. (c-d) Magnified views of each EBID deposit on each end of the T-CNT. (Lu et al, 2006)

After the clamping was complete the specimen was loaded. The test was conducted and a stress strain curve was obtained. Figure 3.15 shows the results obtained from the test. (Lu et al, 2006)

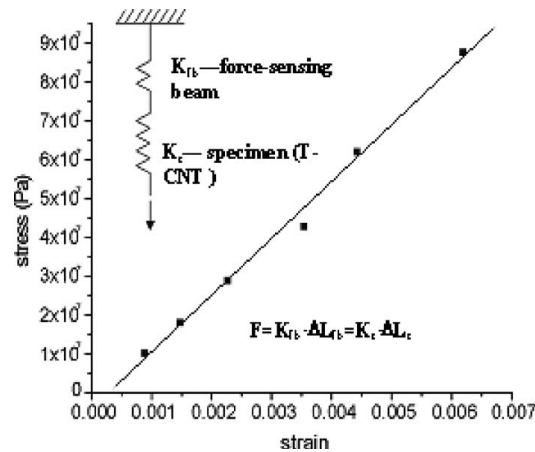


Figure 3.15: Stress vs strain data for a T-CNT loaded with the MEMS device. K_b is the spring constant of the force sensing beam, ΔL_{fb} is the displacement of the beam, K_s is stiffness of the specimen (T-CNT), and ΔL is the elongation of the specimen. (Lu et al, 2006)

3.1.7. Electrostatic Actuated Nano Tensile Testing Device (EANAT).

Kiuchi, Matsui and Isono in 2007 developed the electrostatic actuated nano-tensile testing device using MEMS fabrication technology to evaluate the mechanical properties of carbon nano-tubes. Focussed Ion beam- chemical vapor deposition (FIB-CVD) technique is used to deposit the carbon nano-wires. This procedure is carried out at room temperature. The schematic of the device is shown in the Figure 3.16 below.

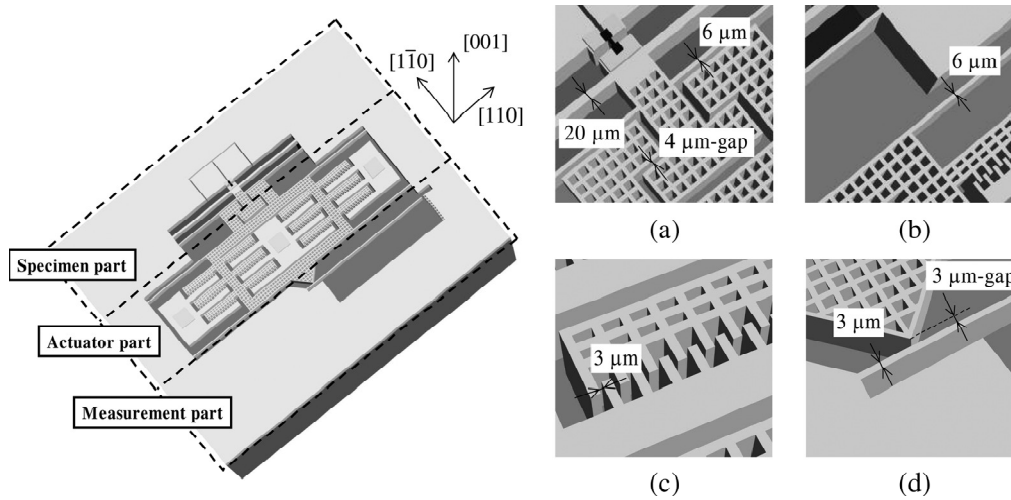


Figure 3.16: Schematic of the design layout for an EANAT by Kiuchi, Matsui, and Isono. Details of: (a) specimen part suspended by a 20- and a 6-μm-wide beam including 5-μm long carbon nanowire with diameter ranging from 90-150 nm; (b) a 6-μm-wide suspended beam of the actuator part consisting of 1000, 3000, and 5000 pairs of electrostatic comb drive actuators; (c) electrostatic comb drive actuators; and (d) fixed end of cantilever of the measurement part used as a lever motion amplification system for calibrating tensile load and displacement of the nano-wires. (Kiuchi et al, 2007)

The actuator part which is located at the side of the sample, has a gap of four microns. The sensor part of the device is present next to the actuator part with a gap of 3 microns. These gaps play an important role in confirming the start of a tensile test by

preventing the nano-wires from pre-loading before the test begins. The specimen and the actuator parts of the device are suspended by fixed fixed beams used to support the parts of the device and also to calculate the tensile load from the spring constants of the beams. Since only the cantilever is asymmetrically integrated into the *EANATs*, the friction force generated at the contact point of the actuator part with the cantilever has the possibilities of a lateral movement of the specimen and the actuator part. The friction force can also lead to a deviation from the theoretical position at the free end of the cantilever. The displacement in the x-direction at the specimen part was predicted to be in the range from 0.01 to 0.04 nm from the center axis of the *EANATs* and was considered negligible in comparison with the y-direction displacement. Tensile tests using *EANATs* undergo the following three stages. During the first stage, a bias voltage is applied to the comb drive actuators to cause travel of the actuator part toward the cantilever integrated into the measurement part. Due to the initial gap of 3 microns, there is no deflection of the cantilever observed at the free end. The actuator part comes into contact with the cantilever when the gap has completely reduced. The comb drive actuators which are present produce the electrostatic force right before the contact with the cantilever. This electrostatic force is expressed as a function of the total spring constant of the suspended beams in the actuator part.

$$F = k_1 \cdot D_1$$

D_1 is the displacement of the actuator, k_1 is the total spring constant of the suspended beams of the actuator. During the second stage, the cantilever is bent by the actuator part with an increase of the bias voltage. The electrostatic force produced at this stage is given by the following:

$$F = g_A k_1 + D_2(k_1 + k_2)$$

Here g_A is the gap width between the actuator and the cantilever, k_2 is the spring constant of the cantilever, and D_2 is the displacement of the actuator part from the position at contact with the cantilever to the specimen part. During the third stage, further increase in the bias voltage results in contact of the actuator part with the specimen part, so that the nano-wire is stretched by the actuator part. Before tensile failure of the nano-wire, the force produced by the comb drive actuators is expressed by:

$$F = g_A k_1 + (g_b - g_a) \cdot (k_1 + k_2) + \left[\frac{\delta_{amp1}}{91} - (g_b + g_a) \right] \cdot (k_1 + k_2 + k_3) + p$$

Here, g_b is the gap width between the specimen and the actuator part, δ_{amp1} is the deflection at the free end of the cantilever before tensile failure of the nano-wire, k_3 is the total spring constant of the suspended beams fabricated in the specimen part, and P is the tensile load spent on deformation of the nano-wire. The tensile testing results of for the FIB deposited carbon nano wires is shown in the Figure 3.17 which shows the load displacement curves for carbon nano-wires deposited on EANATs. Fine resolutions for tensile load and displacement were obtained, for the *EANAT* with 1000 pairs of comb-

drive actuators as shown in Figure 3.17 (a), whereas the resolution is weakened for the *EANAT* with 5000 pairs of actuators shown in 3.17 (c). This is because the electrostatic force generated by a step of 0.1 V/0.1 s is proportional to the number of comb actuators. No load increments are also observed in each initial stage of the tensile tests. These are due to an initial deflection of the nano-wire as shown in the example of Figure 3.17 (d). The initial arch-like deflection was produced during the FIB-CVD process where the nano-wire was bridged across the gap space of 5 μm in the specimen part of the *EANAT*. The length of the stretched nano-wire at full-length, according to the above explanation, was used to calculate the strain.

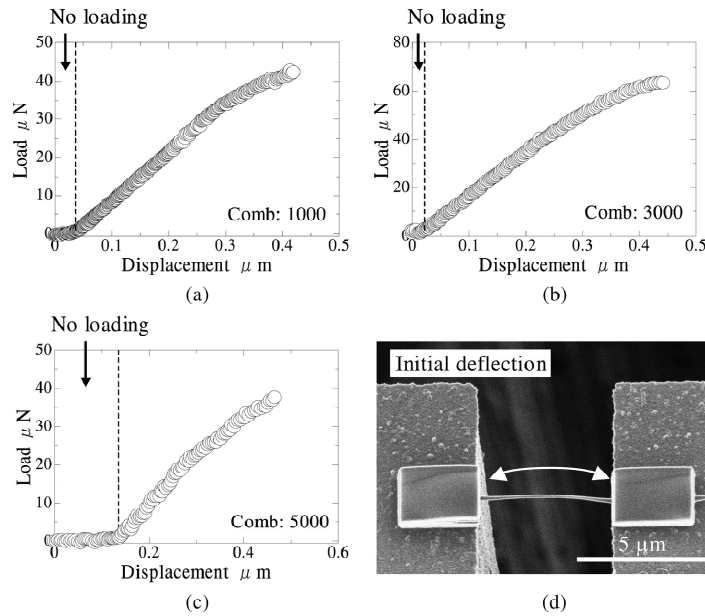


Figure 3.17: Load-displacement curves for carbon nano-wires on *EANATs* by Kiuchi, Matsui and Isono (2007) with: (a) 1000; (b) 3000; and (c) 5000 pairs of comb drive actuators. (d) FE-SEM micrograph of a carbon nano-wire with initial deflection. (Kiuchi et al, 2007)

The stress-strain curves show inelastic deformation behaviors just before tensile failure. Although other experimental results are omitted here, most carbon nano-wires have displayed similar stress-strain trends in relation to these Figures. Young's moduli for the carbon nano-wires are 53.7, 51.3, and 74.7 GPa for the *EANATs* with 1000, 3000, and 5000 pairs of actuators, respectively. Fracture stress and strain range from 3.9 to 4.6 GPa, and from 0.074 to 0.094, respectively.

3.1.8. Force Sensor Technologies:

In this design by Haque and Saif (2002), the force sensor system is a relatively simple design. It consists of pairs of force sensor beams with two displacement markers as shown in the Figure 3.1. When the actuation takes place there is a deflection in the specimen which in turn causes a deflection force sensor beam. Let this deflection be δ . The force on the specimen is given by $F=k*\delta$. Here, k is the stiffness and is given by;

$$k = \frac{24EI}{L^3};$$

Where L is half of the total length of the force sensor beam, E is the elastic modulus of the material and I is the moment of inertia obtained from the beam cross section. A nano-indenter could be used to find an accurate value of k . The force resolution depends on the spring constant ' k ' of the force sensor beams and the measurement of δ . The displacement sensors A and B which are marker gaps in the chip read the displacements of both ends of the specimen. Readings of the marker A gives the

displacement δ of the force sensor beam. The relative displacements between markers A and B will result in the elongation of the specimen, which is subsequently used to compute the strain and the stress. (Haque et al, 2002)

The force sensing mechanism in the design by Han and Saif (2006) boasts the calibration of the sensing technique before the testing without cleaving the stage. There are 2 separate silicon calibrators each having a leaf spring. One of the calibrators, the “master calibrator” is first calibrated by a nano-indenter, which is then used to calibrate the leaf-spring of the second calibrator. The force sensing beams of the tensile testing stage are calibrated by second calibrator which fits in the space of the tensile stage, as shown in Figs. 3.18 (b) and 3.19 (c). The guides (Fig. 3.18 (a)), guide spring, and guide fit (Fig. 3.19 (a)) prevent calibrator (ii) from rotating and ensure proper alignment. The force sensing beams and the leaf spring of calibrator (ii) are freestanding during calibration in order to avoid friction with the substrate. The deflections of the leaf spring and the force sensing beams are measured from the change of the gaps at the gauges shown in Figs. 3.19 (b) and 3.18 (d). The master calibrator cannot be used to calibrate the force sensing beams directly since it is glued to a larger substrate that allows its calibration in the nano-indenter (Han et al, 2006).

Note that during calibration, the freestanding metal specimen buckles and hence its force contribution against the calibrator leaf spring is negligible.

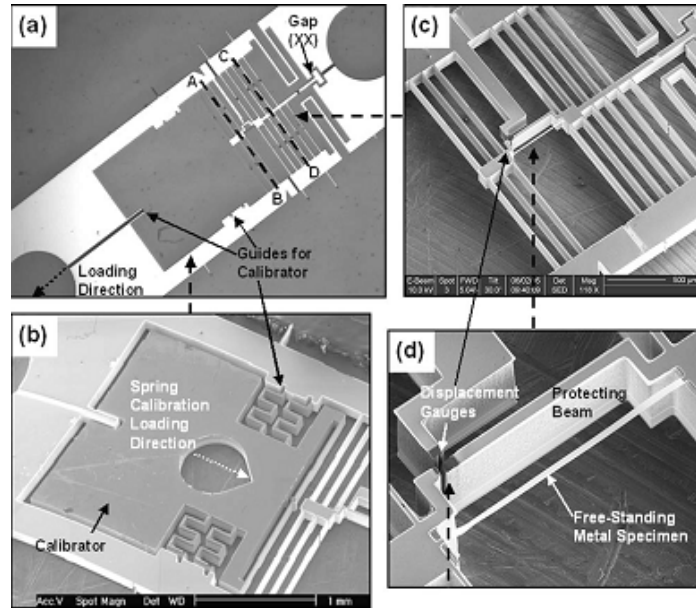


Figure 3.18: (a) Optical microscope view of the entire stage with force sensing beams (*AB*) and support beams (*CD*), (b) SEM micrograph showing the calibrator in place for calibration of the force sensing beams, (c) SEM micrograph of the stage near the specimen and Si beams, (d) Zoomed-in view near the displacement gauges (the displacement gauges serve as a protecting beam before FIB cut. (Han et al, 2006)

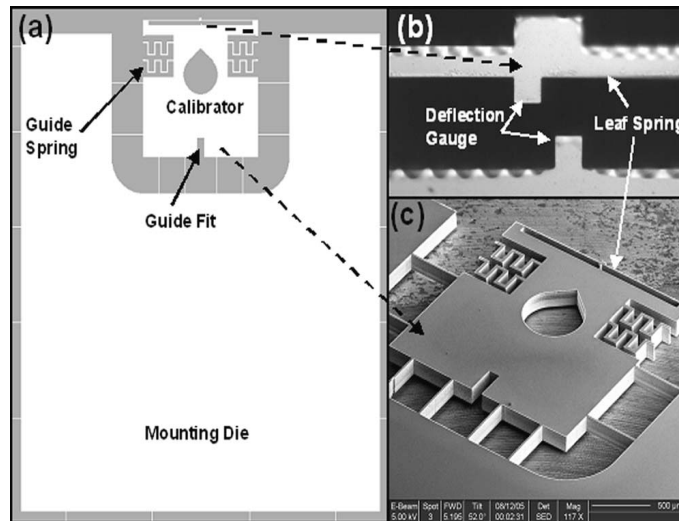


Figure 3.19: Description of the calibrator design by Han and Saif: (a) computer-aided design (CAD) drawing of a calibrator connected to a mounting die by thin Si beams, (b) optical microscope view at the deflection gauge area, and (c) SEM view of the calibrator and part of the mounting die. (Han et al, 2006)

In the design by Zhu and Espinosa (2007), the load on the specimen was measured electronically by means of a load sensor. The load sensor that was employed was based on differential capacitive sensing of displacement due to its sensitivity and linear behavior within the displacement range that was needed to investigate nanostructures. Through a proper calibration of the load sensor stiffness, the load was computed, and a calibration equation was obtained. The key of the load sensor is to measure displacement in terms of capacitance change with high resolution. The differential capacitive sensor consists of one set of movable electrodes (fingers) and two sets of stationary electrodes (fingers), as shown in the left portion in Figure 3.20.

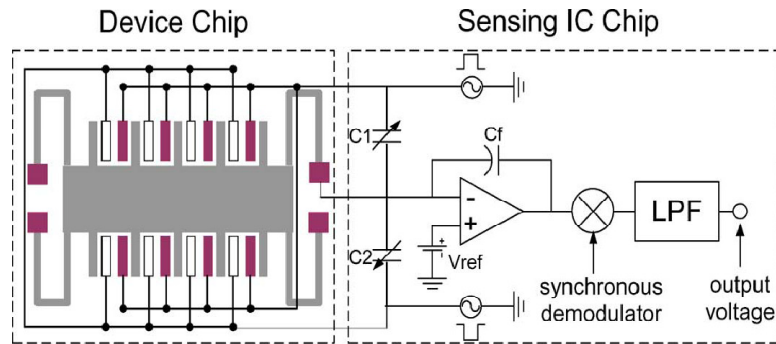


Figure 3.20: Double-chip architecture used for measuring capacitance change. Schematic figure shows the differential capacitor and signal conditioning circuit. The device chip consists of the stationary and the movable fingers and the capacitance is measured. (Espinosa et al, 2007)

Initially, each movable finger is equally spaced between two stationary fingers. The displacement of the movable fingers is equal to the deflection of the folded beams in the axial direction. There is a variety of circuit configurations to complete the capacitance measurements. Figure 3.20 shows the schematic of the charge-sensing method that is

used in our approach. In brief, change of the output voltage V_{sense} is proportional to the capacitance change.

$$\Delta V_{\text{sense}} = \frac{V_0}{C_f} \Delta C$$

Where ΔV_{sense} is the change of the output voltage, V_0 is the amplitude of an ac voltage signal that is applied to the stationary fingers, and C_f is the feedback capacitor. Now the equivalent change in the capacitance is given by:

$$C_{13} - C_{23} = N\epsilon_0 A_1 \left(1 + \frac{C_1 + C_2}{C_1 C_2} \right) \left(\frac{1}{d_0 + \Delta d} - \frac{1}{d_0 - \Delta d} \right)$$

$C_{13} - C_{23}$ is the capacitance difference that we measure in the experiments. The value agreed well with those obtained from finite element simulation (Corigliano et al, 2004). Figure 3.21 shows the device, with its electric circuit and the equivalent electrical circuit after a $\Delta - Y$ transformation.

It can be Figured that $C_{13} - C_{23}$ is larger than $C_1 - C_2$ for the same displacement Δd . Now the curve between the capacitance change and the displacement is shown in the Figure 3.24. As the displacement is a known quantity, the force can also be calculated as follows;

$$K_{LS} X_{LS} = K_S X_S \quad K_S X_S + K_A X_A = F$$

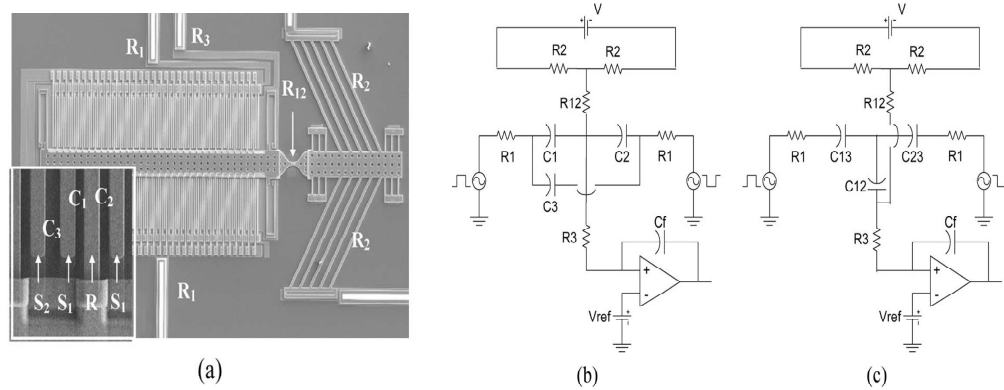


Figure 3.21: (a) Device with ETA and corresponding resistances and capacitances. Inset shows the details of movable finger and stationary fingers. $R2$ denotes the resistance of the thermal beams, $R12$ denotes the resistance of the specimen, $R1$ and $R3$ denote the resistances of the electric traces, $C1$ and $C2$ denote the capacitances between the movable beams and the two stationary beams, respectively, $C3$ denotes the capacitance between two nearby stationary beams. (b) Electric circuit for the device in (a). (c) Equivalent circuit to that in (b) after a $\Delta - Y$ transformation. (Espinosa et al, 2006)

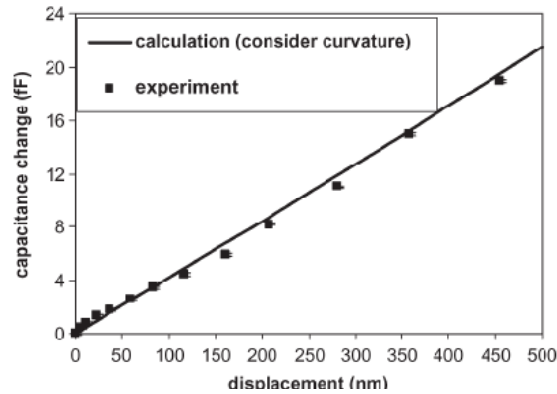


Figure 3.22: The plot of capacitance change vs displacement. This shows that the displacement varies linearly with capacitance change and hence with the capacitance change known the displacement and the force can be found. (Espinosa et al, 2007)

Here X_s is the deformation of the specimen; X_{LS} is the displacement of the load sensor, X_A is the displacement of the actuator, K_S is the stiffness of the specimen, K_{LS} is

the stiffness of the load sensor, K_A is the stiffness of the actuator, and F is the total force that is generated by the actuator.

The force sensor design in this MEMS device developed by (Samuel, 2006) is an analytical process. The amplified lateral displacement is measured which helps calculating the force. When a column buckles the lateral displacement (' D ' in Figure 3.8 (a)) of the column represents an amplified version of the axial displacement (δ in Figure 3.8(a)).

In these columns an initial buckle of ε is given as shown in the Figure 3.8. The force on the columns can be measured from the lateral deflection;

$$F = \omega^2 \left[1 - \left(\frac{\varepsilon}{D} \right) \right] k + \omega^4 D^2 \left[1 - \left(\frac{\varepsilon}{D} \right)^3 \right] \frac{k}{32}$$

Where k is the lowest flexural rigidity (EI); $\omega=2\pi/L$. The force on the specimen is given as the differential force and upper sets of columns;

$$F_{specimen} = (F_{cd} + F_{c'd'}) - (F_{ab} + F_{a'b'})$$

The axial displacement δ is the scaled down version of the lateral displacement of the column. As the buckle is considered to be a sinusoidal curve the relation is given by;

$$\delta = \frac{w^2 D^2 L}{16} \left(1 - 0.7697 \left(\frac{\varepsilon^2}{D^2} \right) \right)$$

Hence, the force on the columns and consequently on the specimen and the axial displacement can be estimated from the lateral displacement.

In this following design by Leseman and Mackin in 2007, a load cell is present which measures the load on the membrane. In order to accurately measure this load, the load cell must first be calibrated. Several calibrated weights are hung on the load cell. After this a calibration curve as shown in the Figure is generated. (Leseman et al, 2007)

The relationship between force and displacement for the load cell used in the following experiments was found to be:

$$F = 37.7x + 1.73x^3$$

Where F is the force and x is the displacement of the centerline of the fixed-fixed beam structure. The first and second numbers are the linear and cubic spring constants. This equation fit the calibration data with an R value of 0.9999. Figure 3.23 shows the calibration curve for the load cell used in the experiments.

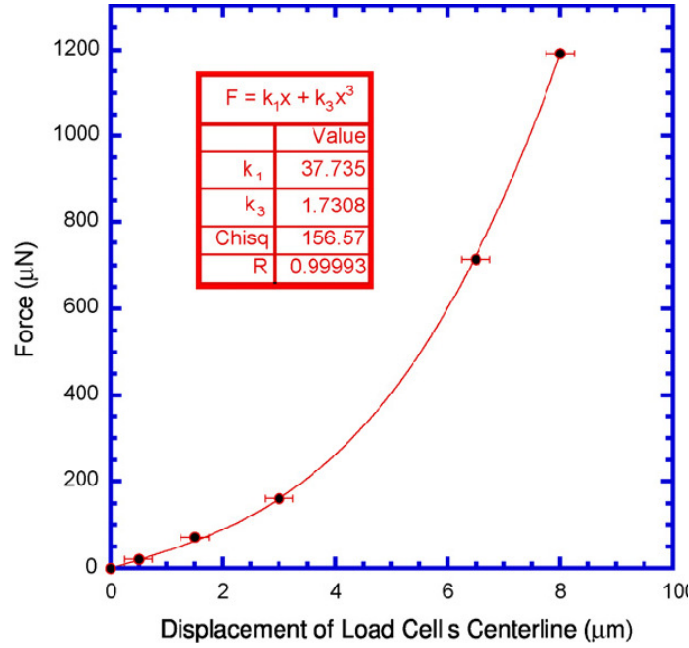


Figure 3.23: Calibration curve for the load cell used in the experiments by Leseman and Mackin. The x -error bars are due to the resolution of the co-fabricated vernier, while the y -error bars are not visible due to the fine accuracy of the calibrated weights. (Leseman et al, 2007)

As shown in the Figure 3.24, two microscopes were used, first an interferometric microscope for measuring membrane displacement and second an optical microscope used to image the vernier. The interferometric microscope was positioned such that it faced the bottom side of the membrane basically to record the deflection of the membrane. Fringe counting technique was used to measure the deflection. The interferometer also helped in identifying the starting point of the experiment. The optical microscope was positioned in front of the vernier in order to measure the motion of the load cell via the vernier. Motions of ± 250 nm can be resolved by the vernier. Note that the displacement of the vernier also gives the force applied to the load cell.

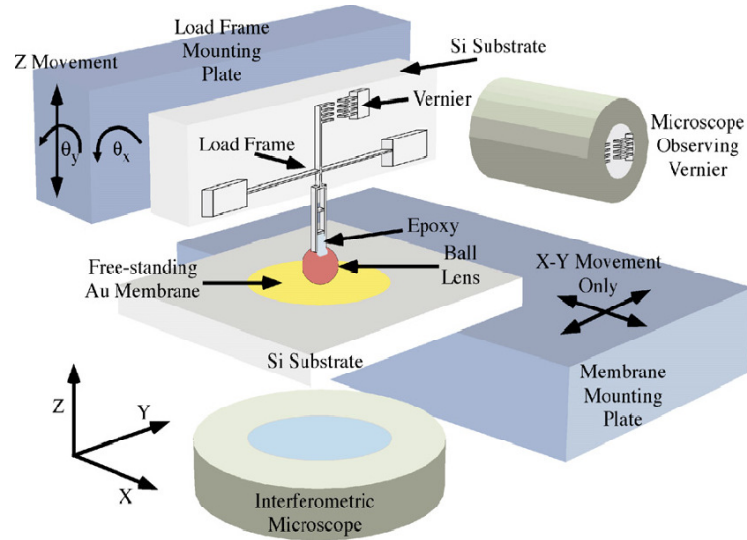


Figure 3.24: Schematic ready experimental setup of the design by Leseman and Mackin. Here the load frames the load cell, the axisymmetric thin film membrane, high precision linear and rotational stages and the 2 microscopes. (Leseman et al, 2007)

The force sensing technique in this device presented by Demczyk et al in 2002, where there is a direct tensile load applied to the nano-tubes is presented. An AFM stage was mounted in the TEM. The stiffness of the AFM cantilever was known and the deflection of the AFM cantilever was measured through a range of travel of the drive. Hence, the force could be determined for a given extension of the drive. A tensile test device replaced the AFM cantilever and the extension of this device was noted for the same force exerted by the spring. By this the force sensing capability of the testing device was calibrated. During the experiment, the piezoelectric stage of the manipulation holder imparts load on the spring, applying a deflection. The force applied by the linear spring

minus the restoring force supplied by the test device was the total force applied on the specimen (Demczyk et al, 2002)

In the design by Lu et al in 2006, there is a direct force sensing beam present which is attached to the platform B shown in the Figure 3.13 which measures the force by measuring the deflection of this beam. The advantage of this device is that this approach has the flexibility to separate the electrical circuits for the assembly and testing in the same device. Now, when load is applied on the specimen through the actuator, the force sensor beam also deflects with the specimen. A strain is caused, which is computed from the original length and the measured length. The force on the specimen (T-CNT) was calculated by;

$$F = K_{fb}x_{fb}$$

Where x_{fb} is the deflection of the force sensor beam and K_{fb} is the stiffness of the force sensing beam. The deflection of the force-sensing beam is obtained by measuring the displacement of platform B attached at the center of the force-sensing beam. From the equilibrium of forces, the load on the T-CNT from the actuator is equal to the force that the T-CNT applies on the force-sensing beam. The stiffness of the force-sensing beam was calculated from;

$$K_{fb} = \frac{24EI_{fb}}{L_{fb}^3}$$

Where E is the silicon modulus taken as 169 GPa; I_{fb} and L_{fb} are the moment of inertia of the beam and the length from the center of the beam to one of the fixed ends shown in Figure 3.13. (Lu et al, 2006)

In the design by Kiuchi, Matsui, and Isono, there is a separate measurement part as shown in the Figure 3.16. The measurement part is used as a lever motion amplification system for calibrating tensile load and displacement of the nano-wires. Figure 3.25 shows a schematic diagram of the cantilever used in the measurement part. The travel distance of the actuator part in the tensile direction has been measured from deflection at the free end of the cantilever. The cantilever is bent by contact with the actuator part when a bias voltage is applied to the comb drive actuators, and it amplifies the travel distance of the actuator part according to the following equation:

$$\delta_{amp} = l_2 \sin i + \delta \cong \frac{2l_1 + 3l_2}{2l_1} \delta$$

Where δ_{amp} is the cantilever deflection at the free end, i is the angle of the deflected cantilever, l_1 is 50 in the present design of the *EANATs*, the length of the cantilever from its fixed end to the contact point of the actuator part with the cantilever, and l_2 is 3000 in the present design, the length from the contact point to the free end of the cantilever. Therefore, the amplification factor is defined as 91 for the present design. (Kiuchi et al, 2007)

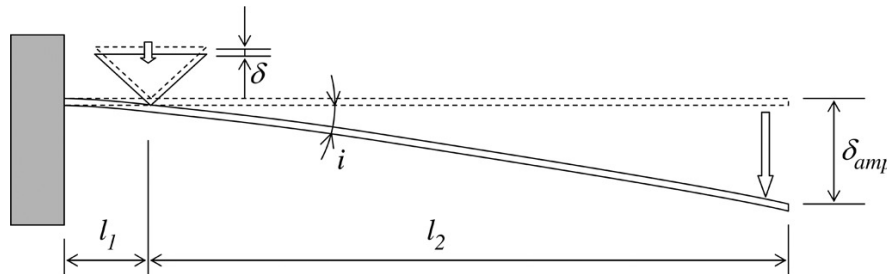


Figure 3.25: Schematic diagram of the cantilever used as the lever amplification system by Kiuchi, Matsui, and Isono. The actuator deflects the base of the cantilever by δ and the resultant deflection at the tip of the cantilever is δ_{amp} , which is the amplified deflection. (Kiuchi et al, 2007)

3.1.9. Actuator System:

Now we will be discussing the actuation system of all the devices described above. Each device has its own unique actuator system to apply the load to the respective specimens.

In the design by Haque and Saif in 2002, the device is divided into three portions. One end of the testing device contains the force sensor beams as shown in the Figure 3.26. The other end of the device consists of the support beams, the deflection marker, and the u springs for stability. The central part of this device is the free standing film specimen. Gripping of the specimen to the testing chip is due to the adhesive forces between the silicon substrate and the specimen. The u-shaped springs maintain the structural integrity and the stability of the device between the fixed and the moving ends of the device. There are two holes on either side of the device, which are designed such that they can fit the mounting device on the TEM straining stage. One end of the device

as shown in the Figure 3.27 is pulled by the motor and the other end is fixed. Tensile force is applied on the specimen by applying a displacement on the moving end of the stage.

This causes a deflection in the specimen, which in turn causes the same deflection on the force sensing beams. The piezo-actuator is mounted on to the fixed column. The maximum displacement provided by the actuator is about $18\text{ }\mu\text{m}$ at 150V (Haque et al, 2002). The actuator system in this second generation MEMS device developed by Han and Saif in 2006 is exactly the same as the first generation actuator system as discussed above.

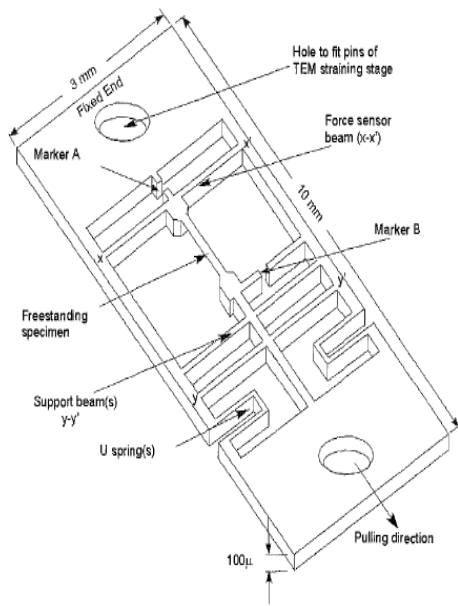


Figure 3.26: Schematic figure of the device showing the pulling direction and the actuation, the markers A and B are the displacement markers which sense the displacement (Haque et al, 2002)

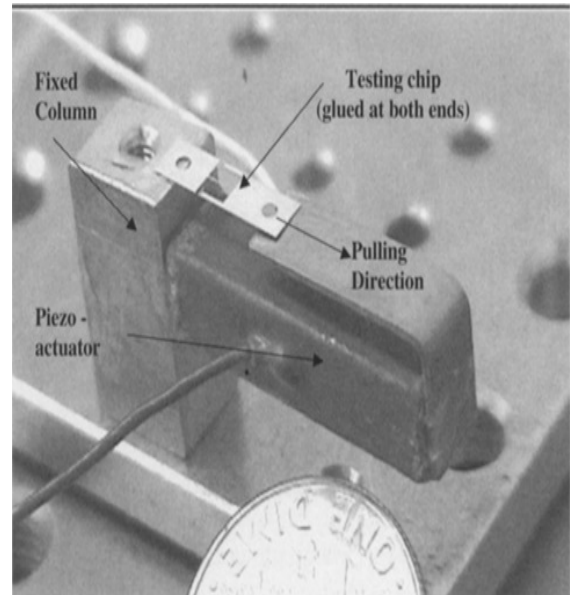


Figure 3.27: SEM image of the MEMS device being tested and the piezo electric actuator. (Haque et al, 2002)

In the MEMS based material testing system developed by Zhu and Espinosa in 2007, an interesting actuation system was introduced in this device. This theory is based on the thermal expansion of free standing beams when subjected to joule heating. Figure 3.28 shows a schematic of the electro-thermal actuation system. The system consists of a shuttle at the center which is connected to the two anchors on either ends of the shuttle by the inclined beams. When there is a voltage difference applied across the two anchor sites, heat is generated along the beams. This heat results in the thermal expansion of the inclined beams. This expansion will push the center shuttle forward as shown in the Figure 3.28 clearly. There are heat sink beams present which are designed to reduce the temperature at the actuator-specimen interface. Figure 3.29 shows the temperature increase and the displacement variation in the shuttle axial movement. (Espinosa et al, 2007).

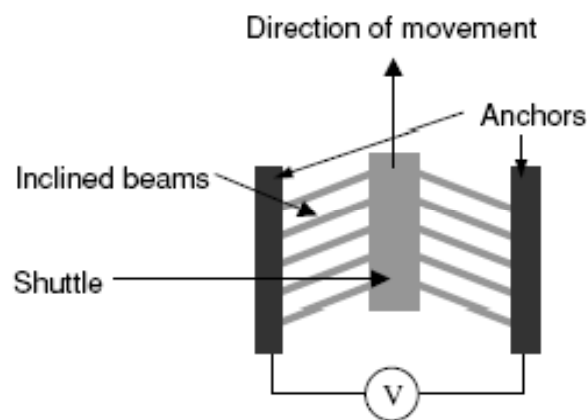


Figure 3.28: Schematic figure of the thermal actuator by Zhu and Espinosa (2007) where there are 5 pairs of inclined beams clamped to the shuttle and anchors at the 2 ends, the voltage is applied between the anchors. (H.Espinosa et al, 2007)

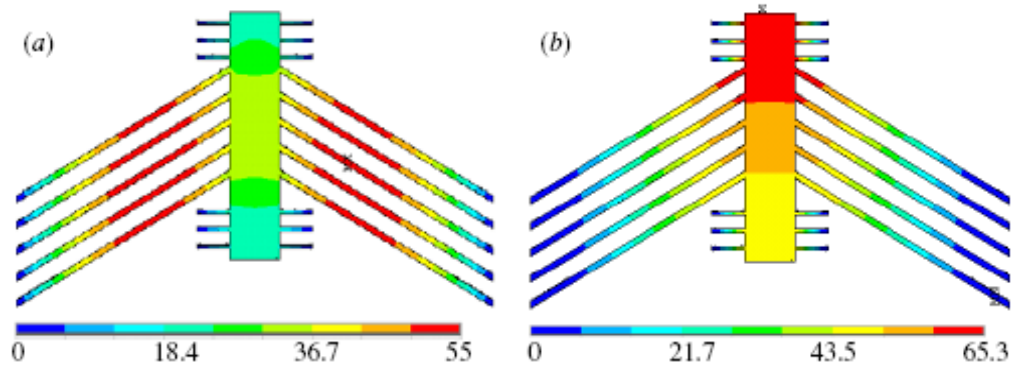


Figure 3.29: Results by Zhu and Espinosa (a) Temperature (in °C) and (b) displacement (in nm) fields in the thermal actuator with three pairs of heat sink beams at the specimen end. The displacement component in the plot is in the shuttle axial direction. (Espinosa et al, 2007)

In this actuation system, it is assumed that the thermal actuator does not buckle within the operational temperature range. The displacement of the shuttle in the y -direction and the reaction force in the x -direction, due to the average increase of the temperature along the beam is given by;

$$U^{\Delta T} \equiv U_y^A = \alpha \Delta T l \frac{s}{\left(s^2 + c^2 \frac{12I}{Al^2}\right)} = \alpha \Delta T l \frac{s}{\left(s^2 + \frac{c^2}{\phi}\right)}$$

$$R_x^{\Delta T} \equiv R_x^A = -\alpha \Delta T E A \frac{c}{\left(c^2 + s^2 \frac{12I}{Al^2}\right)} = -\alpha \Delta T E A \frac{c}{(s^2 \phi + c^2)}$$

Here, α is the coefficient of thermal expansion of the beam material, E is Young's modulus of the material, l is the beam length, A is the beam cross section, I is the moment of inertia of the cross section with respect to the out of plane axis z and c and s are cosine

and sine of the beam angle θ . The dimensionless parameter $\psi = Al^2/12I$ is defined as the axial over bending stiffness ratio. The displacement caused by the thermal actuation affects the specimen displacement which in turn is sensed by the load sensor. With the known stiffness of the actuator and the sensor we can determine the load on the specimen.

In the load sensing device designed by Samuel and Haque in 2006, a piezo motor is used to load the lower set of columns as shown in Figure 2.7. The lower set of columns (cd and c'd') in the Figure 2.7, is longer than the upper set of columns (ab and a'b'). As we reach the critical load, the lower columns buckle before their upper counterparts. The shorter set of columns has a higher critical load. By further applying the load, when the critical load of the upper set of columns is reached, they will also buckle. At this point, the central rib will begin to translate upwards, which will cause tensile loading on the specimen. It should be noted that, by placing the fixed support on the upper side of the central rib, the device can also be used to apply compressive loading on the specimen (Samuel et al, 2006).

In this design of MEMS load cell by Leseman and Mackin in 2007, experiments were conducted by bringing the sapphire ball lens, which is attached to the load cell, into contact with the center of the free standing thin membrane. By doing this the membrane is deflected. When there is no strain on the tip of the load cell, there is a simple relationship between the motion of the piezo-electric crystal, the deflection of the fixed-

fixed beam's center point, and the center point of the membrane, as shown in the Figure 3.30.

$$\Delta y_{piezo} = \Delta y_{vernier} + \Delta y_{membrane}$$

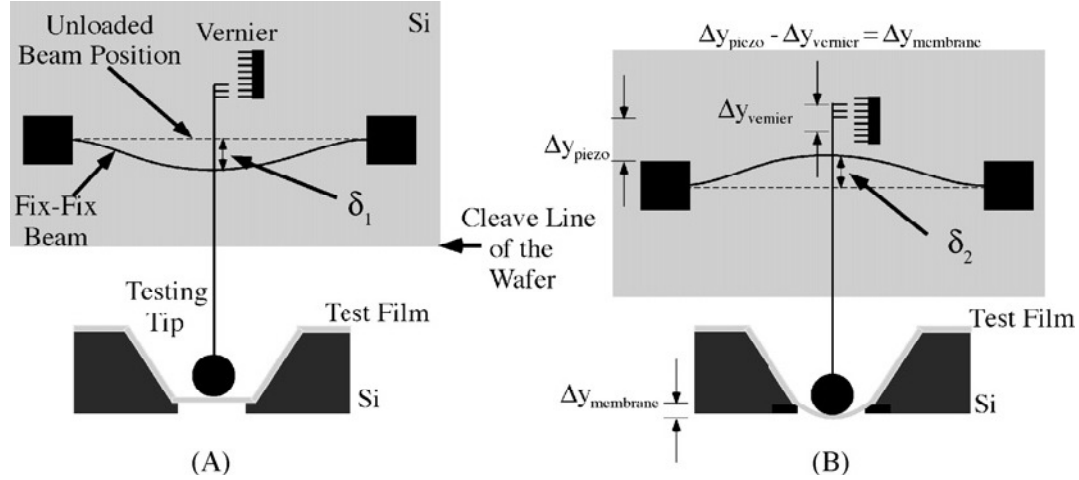


Figure 3.30: Schematic of experimental setup by Leseman and Mackin. (a) Before loading of the freestanding thin film membrane. Here the fixed beam is in unloaded position and there is a initial deflection of δ which is due to the calibrated weights and the vernier is set to zero error. (b) After loading of the freestanding thin film membrane the vernier gives a reading and the membrane is bent as shown. (Leseman et al, 2007)

The alignment of the membrane extreme care was taken. Four high resolution

linear stages and two rotational stages were used to align the membrane. Two stages were used to position the center of the membrane in the x-y plane. The other two stages were used to move the ball lens into contact and further deflect the membrane. One of these two stages was a manually operated stage which allowed coarse movement of the load cell. The outer stage was mounted on the coarse stage. This stage was actuated by a piezo-electric crystal stack with sub-nm resolution. Two goniometers were used to align the load cell to the place of the membrane.

In the design by Demczyk et al (2002), the actuation was done by applying tension by utilizing a piezoelectric manipulation holder, fabricated in-house. (Cummings et al, 2000), (Collins et al, 2000) (Poncharal et al, 1999)

In the design for in-situ tensile testing for template carbon nano-tubes by Lu et al (2006), theory of thermal expansion was used to actuate the testing as shown in the Figure 3.13. The actuation unit is composed of thermal expansion beams and a motion amplification system. . By running current through the thermal expansion beams, displacement at their free ends is transferred into nanoscale motion along the axis of the platform A by a V-shaped structure for motion amplification. As the end bars of the thermal beams expand out they will stretch the V-shaped beam longitudinally outwards causing the platform A to deflect and this applies a tensile load on the specimen. On the opposite side of platform A, platform B is attached in the middle of the direct force-sensing beam, which is suspended and clamped at both ends to the fixed contact pads Q_1 and Q_2 . The support beams ensure that the platform A moves away from platform B in the longitudinal direction as shown in the Figure 3.13. The resistance of the entire device, with the applied dc current which was incremented and the voltage drop across the device was simultaneously recorded to obtain the power supplied. This is the actuation unit in this design.

In the design by Kiuchi Matsui and Isono (2007), there is a separate actuator part as shown in the Figure 3.16. The actuator consists of 1000, 3000, and 5000 pairs of

combs. The actuator works on the comb drive actuator principle. By application of a bias voltage, the capacitance change is induced which applies a force on the movable fingers of the combs and the actuation takes place. The pairs of combs are in parallel which makes the capacitors in parallel, hence the capacitances add up and the force applied on the carbon nanowires increases. This is the actuation system used by the authors.

These are the different MEMS devices, which have been produced and been used to test the mechanical properties of different nano- materials. All the above discussed devices test the mechanical properties of the nano-materials. Now let us venture into a different field of specimens: Bio-materials such as living cells. The next section discusses about the different MEMS devices designed for cell mechanics and life sciences.

3.2. *MEMS Devices for Life Sciences*

There has been extensive study on living cells, and the results show that the living cell responds to mechanical stimuli. This response might be with biological changes which might alter cell internal structure which in turn might change the mechanical behavior of the cell. There have been multiple techniques developed to measure the mechanical response of the living cells. These include, Atomic Force microscopy (AFM) (Shroff et al, 1995), centrifugation (Easty et al, 1960), substrate deformation (Banes et al, 1985), multiple particle tracking micro-rheology (Tseng et al, 2002), magnetic twisting cytometry (Wang et al, 1993), magnetic bead micro-rheometry (Bausch et al, 1998), micro pipette aspiration (Evans et al, 1991), magnetic traps (Haber et al, 2000), optical stretcher (Guck et al, 2002), optical traps (Dai et al, 1995), bio membrane force probe (Merkel et al, 1999), shear on single cells (Yamamoto et al, 1998), and tensile tester (Miyazaki et al, 2000). All of these techniques have their own advantages and disadvantages. Some of their common limitations are: they only measure certain types of deformations or small ranges of cell deformation and force response. They also can measure the mechanical response only at certain states. Here we talk about a completely new set of devices which can measure the cell responses of living cells in different approaches. MEMS technologies are employed to fabricate these devices. Let us discuss some of these devices to measure the cell force response in detail.

3.2.1. MEMS based force sensor to measure the force response of living cells.

In this section, we will be discussing the design of the MEMS based force sensor developed by Yang and Saif in 2005. This is a novel technique in which the micro fabricated mechanical force sensors are used to manipulate living cells and measure their force response. This sensor basically deals with the mechano-biological study of living cells and tissues. Initially, the first sensor which was developed was the one component force sensor. The sensor consists of a probe and some flexible force sensing beams. The probe is used to indent the specimen or induce some mechanical change on the specimen, and the flexible beams sense the force by deflecting. The deflection measurement is directly proportional to the force response. Standard optical microscope system is used to record the deformations of the cells and the deflections of the beams. Figure 3.31 shows a schematic and the SEM image of the one component force sensor (Yang et al, 2005).

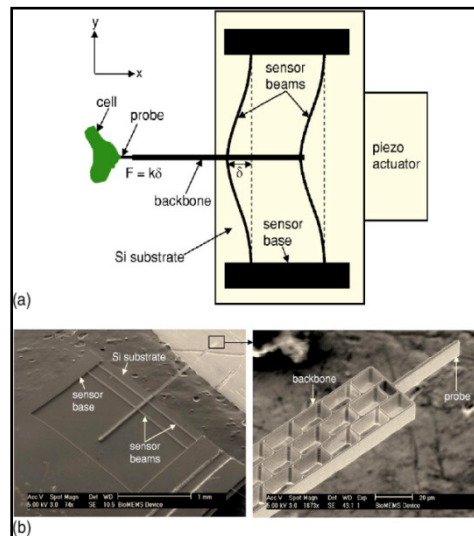


Figure 3.31: MEMS force sensor by Yang and Saif , (a) shows the schematic of the force sensor. (b) Shows the SEM image of the force sensor and its close in image. (Yang et al, 2005)

The probe is connected to the sensor beams with the help of the backbone. This backbone is attached to the center of the sensor beams. The wafer on which the sensor is fabricated is driven by a piezo actuator held by an x - y - z - θ_x - θ_y - θ_z stage.

3.2.1.1. Force sensor working principle:

The force sensor measures the force response of the living cell by indenting the specimen. As the sensor indents, the force sensor beams deflect. The stiffness of the sensor in the x -direction is much smaller than the other two directions due to the high aspect ratio of the beams and their geometry. The stiffness of the sensor along the y direction is extremely high. The sensor is made of single crystal silicon with a young's modulus of 170 GPa. The sensor was fabricated for the following dimensions. The length of each sensor beam is about 2 mm. the cross section of the beam is rectangular. Hence, the depth of the beam is in the order of 10 microns, and the width of the beam in the order of 1 micron. These dimensions result in a particular stiffness of the beam. They can be changed as per the requirement to manipulate the force sensor stiffness. The stiffness is calculated by the following formulas.

$$k = \frac{384 EI}{L^3};$$

Where, the E is the young's modulus and I is the moment of inertia given by;

$$I = \frac{1}{12}bh^3$$

Hence the force response is calculated as: $F = k\delta$,

Here, δ is the deflection of the sensor beams. The exact value of the sensor stiffness may not be very crucial during the cell experiments.

3.2.1.2. Experimental Results:

Figure 3.32 shows a schematic of the experimental system using the sensor. The sensor is fixed to a holder which is mounted on the x-y-z piezo stage with 1 nm resolution, and this piezo stage is in turn mounted on an x-y-z mechanical stage with 1 micron resolution. This mechanical stage is mounted on a rotational platform. An inverted optical microscope is used to monitor the deformation of the cell and the displacement of the sensor beams. Images are taken using a CCD camera and its image acquisition software.

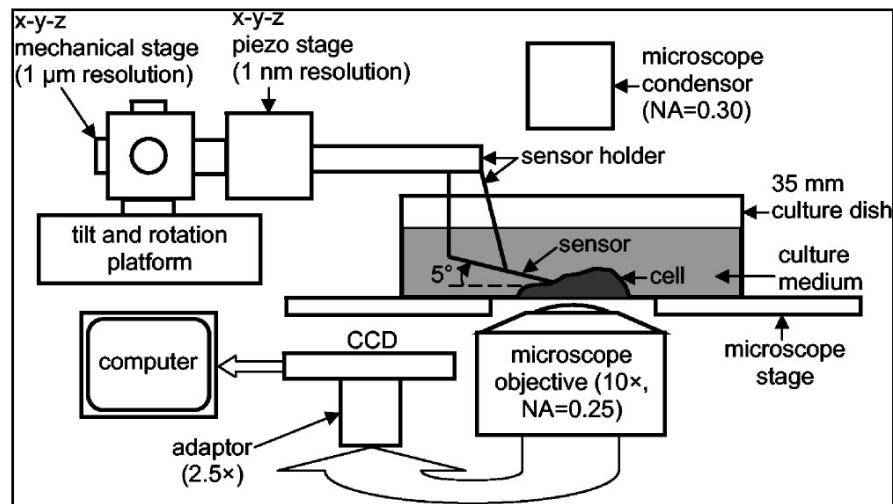


Figure 3.32: Experimental system and the sensor to measure the force response of the living cell. (Yang et al, 2005)

Specimen: The cells are cultured in a 35 mm dish, and the sensor is supposed to be immersed inside the culture medium for indentation purposes. The piezo actuator will perform the indentation in a controlled manner. The sensor plane is inclined by 5 degrees wrt the bottom of the culture dish.

The commonly tested cells which were used for the experimental procedure are monkey kidney fibroblast (MKF) cell line. The experiment was conducted at room temperature. These cells were cultured in a medium with 90% DMEM (ATCC) and 10% FBS (ATCC) in an environment with 37°C. The cell force measurements were conducted at room temperature.

After the cells are ready for experimentation, and the setup is complete, the sensor probe is made to indent the cell inside the culture dish to cause a displacement. This displacement is a small amount of about 2 microns. Figure 3.33 shows the microscope image of the cell being indented. About 72 minutes after indentation there was an obvious change in the shape of the cell observed and the mechanical indentation was reduced. Figure 3.33 (c), (d), and (e) shows the results of different cells.

Another test was performed using the one component force sensor in which the cells were subjected to large lateral indentation. Initially a small amount of indentation was caused for about 20 minutes to observe a cell shape change. If there was no shape change observed, and then the indentation was continued else it was stopped. Figure 3.34 shows the micrographs examining the results of the test.

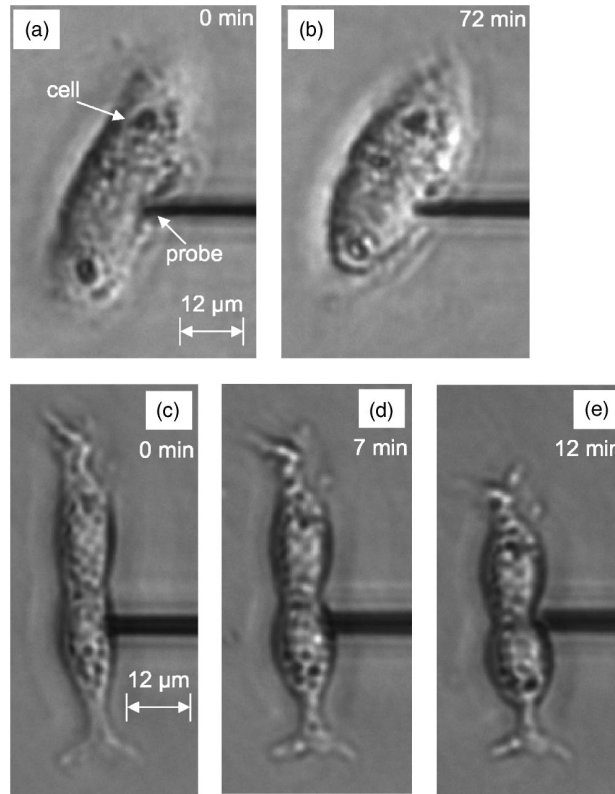


Figure 3.33: Morphological changes of two cells due to mechanical disturbance of the sensor probe. (a) right after the probe indented a monkey kidney fibroblast; (b) the same cell after 72 minutes; (c) right after the probe indented the MKF; (d) seven minutes after; (e) 12 minutes after. (Yang et al, 2005)

From Figure 3.34 (a), we see that the slope between (b) and (c) is larger than between (c) and (d). This might be due to partial breaking of the adhesion with the substrate. After the linear force response stage, the cell has yielded hence shows increased cell indentation without any increase in the force response.

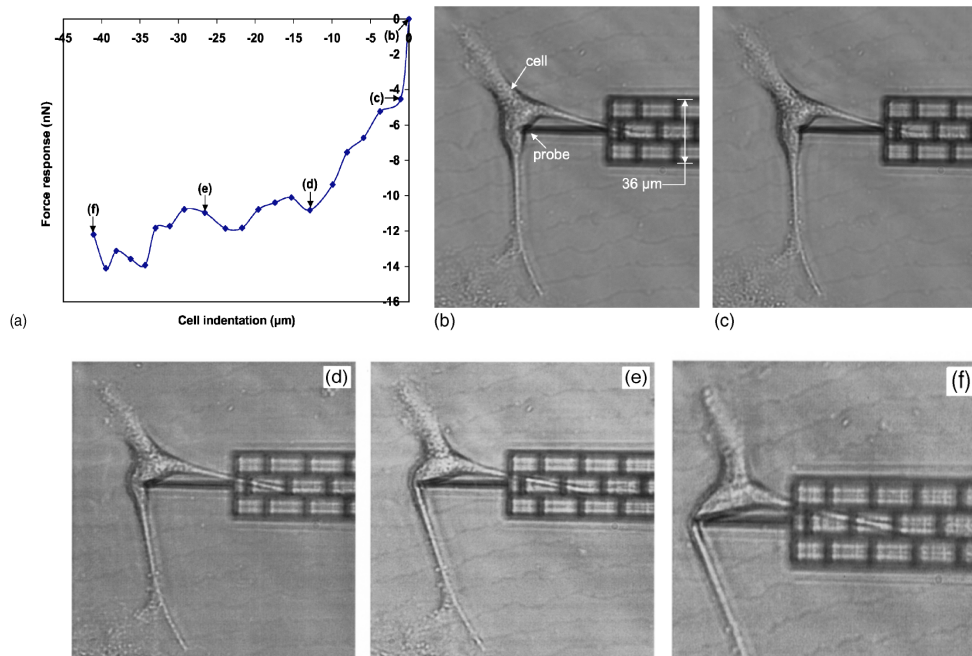


Figure 3.34: Force response of a MKF due to large lateral indentation. (a) the force response vs cell indentation plot; (b) to (f) are representative phase contrast images. (Yang et al, 2005)

3.2.1.3. Multidirectional Force Sensors for BioMEMS

There were further developments made on the previous force sensor. Another kind of sensor was also designed. The sensor we have discussed so far could measure the force response in only one direction. This next sensor could measure the force response in 2 directions. It was known as the two-component force sensor. (Yang et al, 2007). This two component sensor has not been fabricated and tested. Figure 3.35 shows the schematic diagram of the one component force sensor with improvements, and the two component force sensor. It also shows the SEM image of the one component sensor showing the development of adding the deflection measurement reference point.

The new one component force sensor consists of the deflection measurement reference point. This reference point helps measure the deflection very accurately. Now, we will move on to the next device which shows a biaxial test on a single living cell.

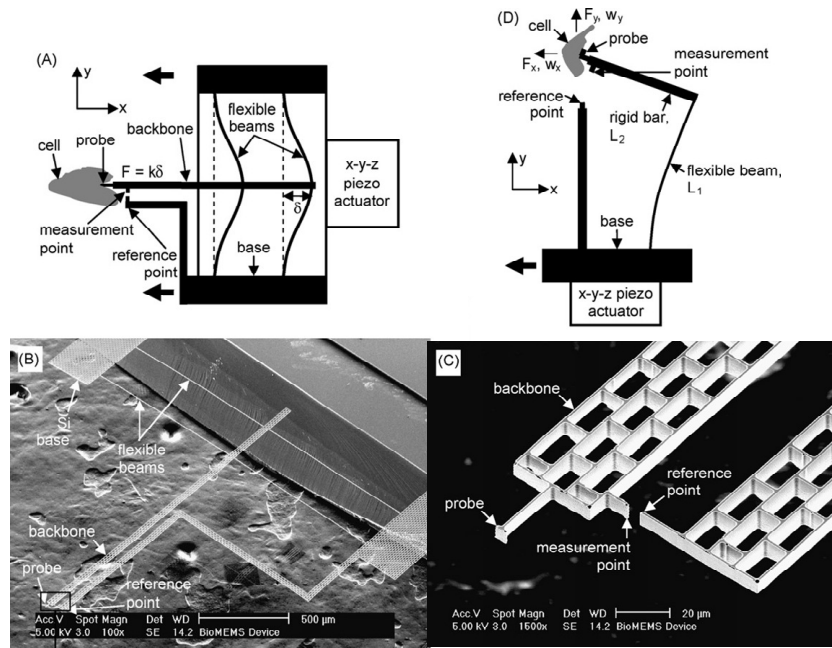


Figure 3.35: The developments to the previous design made by Yang and Saif; (a) Schematic of the one component force sensor. (b) and (c) are the SEM images of the one component force sensor. The deflection measurement reference point is shown. (d) Schematic of the two component force sensor. (Yang et al, 2007)

3.2.2. MEMS platform for biaxial stimulation of living cells

Scuor et al in 2006 designed a MEMS based platform for performing biaxial tensile testing on living cells. While most common methods in this area describe the uniaxial testing of the cells, biaxial testing of the cells remains elusive in the research

field. The design by Scuor et al presents a different approach which makes it possible to both actuate and sense the properties of living cells at a length scale.

This design is based on the concept of in-plane biaxial cell stretching rather than out of plane stretching such as typical flexion of membranes. Figure 3.36 shows the schematic of this MEMS design. The cell is adhered to the center of the platform containing the 4 quadrants. A four link mechanism is used to connect this platform to the comb drive actuator. Out of the 4 quadrants shown in the Figure 3.36 the top quadrant has a fixed constraint. The other three quadrants have one degree of freedom. Figure 3.37 shows the kinematic scheme of the linkages.

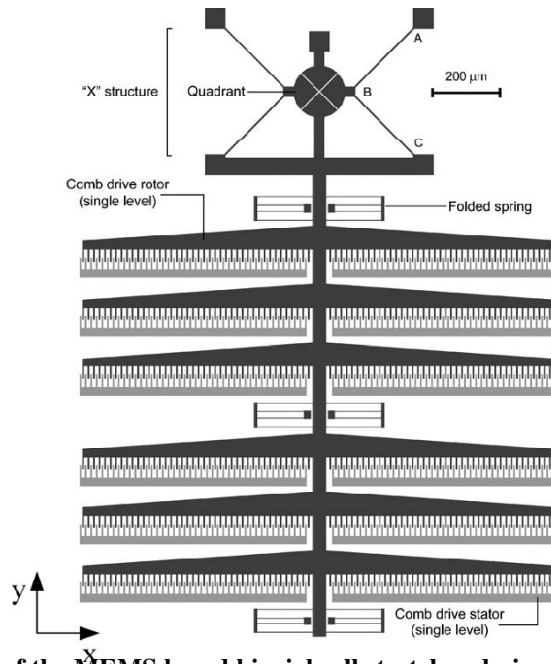


Figure 3.36: Layout of the MEMS based biaxial cell stretcher designed by Scuor et al (2006). It shows the quadrant platform and relative linkages on the top and comb drive actuator in the bottom. Three pairs of folded springs are linear guides so as to avoid any movement in the x direction.

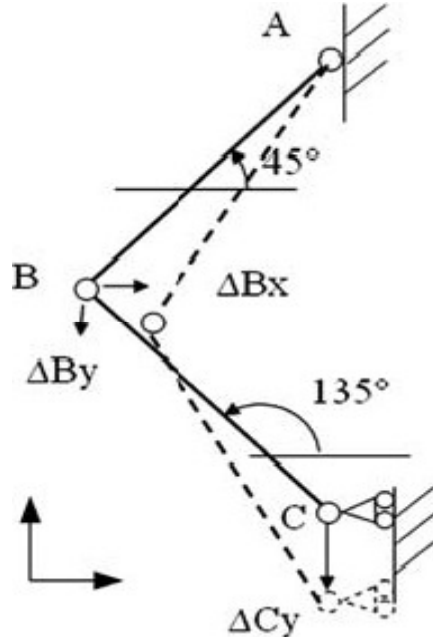


Figure 3.39: Kinematic principle of the biaxial cell stretcher platform, based on the links in Figure 3.36. Scuor et al (2006)

As voltage is applied to the comb drive actuator, the comb drive rotors are pulled down in the y-direction in the Figure 3.36, hence pulling the point C in Figure 3.37. This in turn deforms the quadrant and the quadrants displace in the x and y directions. For small displacements, we can say that the deflections in Figure 3.37 will be related as;

$$\Delta B_x \cong \Delta B_y = \Delta C_y / 2$$

Here ΔB_x is the displacement of the node B in the x-direction and ΔB_y is the displacement of node B in the y-direction. ΔC_y is the total movement of the node C which is the displacement of the comb drive. If Δx and Δy are the distances between the tips of the two pairs of opposite quadrants;

$$\Delta x = \Delta x_0 + 2. \Delta B_x \approx \Delta x_0 + \Delta C_y$$

$$\Delta y = \Delta y_0 + 2. \Delta B_y = \Delta y_0 + \Delta C_y$$

Here, Δx_0 and Δy_0 are the initial tip distances between the opposite quadrants in the un-deformed state. FEA and experimental results validate the initial assumption. Six folded springs are present for structural integrity of the device.

3.2.2.1. Experimental results:

To operate this MEMS device statically in air, the power supply used was a simple DC power wired to the plate connectors. The high voltage generator in the power supply would make it possible to calculate the displacement. This device was placed on a stage of an optical microscope equipped with a CCD camera to observe and record the displacement. Three different tests were performed in 3 environments: air, de-ionized water, and de-ionized water with ionized surfactant.

Firstly, the experiment was conducted in air with a driving voltage range of the comb drive of 0 to 100 V. Figure 3.38 shows the micrograph of the center of the circular platform (with 4 quadrants). It can be seen that the distances between the tips is approximately the same.

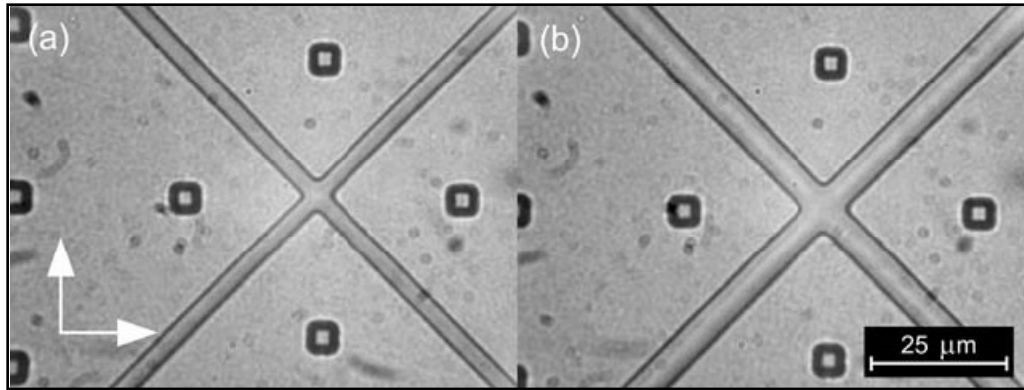


Figure 3.38: Micro-graphs representing the biaxial cell stretcher platform in air at (a) 0V and (b) 100V driving voltage. The small squares are dimples to reduce stiction problems. (Scuor et al, 2006)

The maximum displacement during this test was observed at 100V driving voltage, is about 3.4 μm . Multiple images and displacements were measured at different voltages. Figure 3.39 shows the plot between the displacement and voltage for this test. Figure 3.40 shows the micrographs of the device operating in the second test environment; de-ionized water. The driving voltage range was 0 to 20 V. In this case the maximum displacement measured was at 20 V, which was about 0.9 microns. From Figure 3.39 we see that in air at 20 V driving voltage, the maximum displacement of the tips were 0.15 μm . This is reasonable since the relative permittivity of water is higher than air.

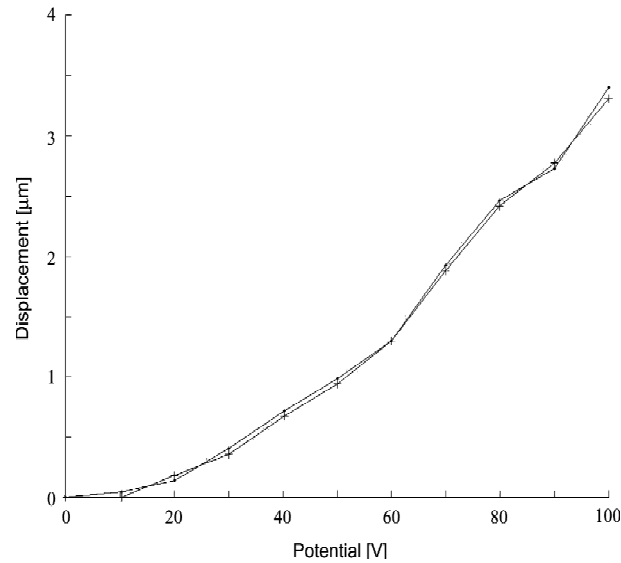


Figure 3.39: Plot of the cell stretcher displacement vs driving voltage in air. (Scuor et al, 2006)

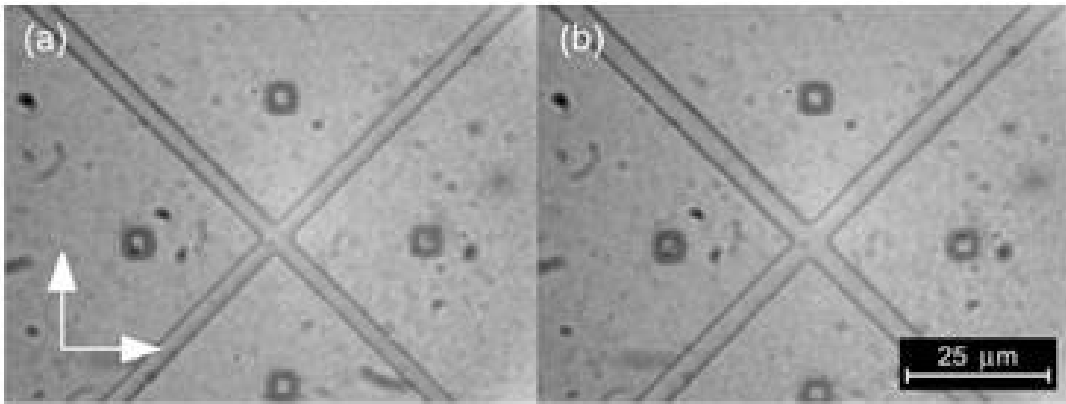


Figure 3.40: Micrograph representing the biaxial cell stretcher in DI water at (a) 0V and (b) 20V, (Scuor et al, 2006)

The third environment; de-ionized water with ionized surfactant between the voltage range of 0-20V. The maximum displacement found was at 20 V, which is about 0.2 microns. This unexpected behavior can be attributed to the increase in the conductivity due to the ionic nature of the surfactant. This might cause the current to bypass the actuators and reduce the power available to the comb drive. Hence, this

MEMS platform gives a good opportunity to explore into the mechanical characterization of living cells, and describes how significant it can be for human life.

3.2.3. *BioMEMS Devices for Uniaxial Cell Stretching*

Serrell et al in 2007 designed a novel technique to perform quantitative force measurements on a single cell and simultaneously allow imaging of the cell deformation to take place. Figure 3.41 shows a schematic of the device with a single cell placed on the platform.

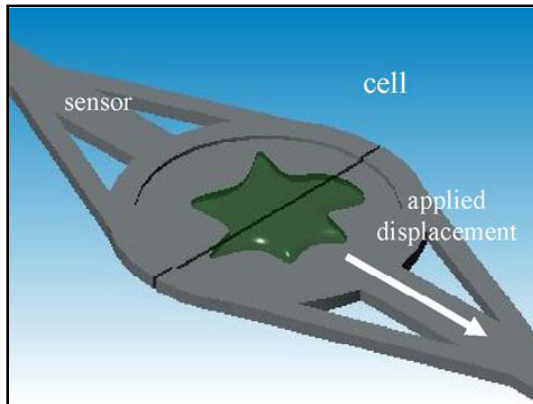


Figure 3.41: Schematic of the BioMEMS device for uniaxial cell stretching. The single fibroblast is placed on the platform. The sensor is on one side of the platform and the actuation takes place on the other side. (Serrell et al, 2007)

A single fibroblast cell is placed on the circular platform as shown in Figure 3.41, which is divided into two parts. The cell is adhered to the platform and after which a displacement is induced to one half of the platform. The other half of the platform is mechanically linked to a sensor which measures the force on the cell. An analogy to this

device would be a displacement controlled uniaxial tensile machine. Figure 3.42 shows the schematic of the complete device and the SEM images of device.

The actuation system of this design consists of an annulus which is hooked by a probe tip and is pulled to induce the displacement. This displacement is provided by a micro-manipulator. This actuator is attached to the cell platform by a poly-silicon beam which is supported by multiple folded beams. These folded beams maintain the structural integrity of the device by making it uniaxial. The resolution of this micro-manipulator is 40nm. This actuator has the ability to provide large displacements on the order of 90 microns depending on the stiffness of the spring. The advantage of this actuation system is that, unlike other devices which require electric power for actuation, this does not need to be isolated from the cell environment.

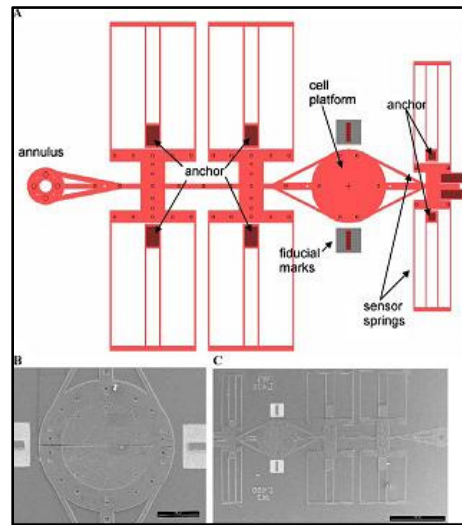


Figure 3.42: (a) Schematic of the device for uniaxial cell stretching. This image shows the actuation and the force sensing system. (b) and (c) SEM images of the circular cell platform and the complete device respectively. (Serrell et al., 2007)

3.2.3.1. Force Sensing Technique:

The sensor is located on the opposite side of the actuation system about the cell platform. The force sensing technique is based on a series of folded cantilever beams creating a spring. By designing the spring, we know the spring constant. Hence, we know the force that is acting on the sensor half of the cell platform. The displacement of the cell is simultaneously measured using a high speed high resolution camera. The fiducial marks on the substrate as shown in the Figure 3.42 are etched into the substrate and they remain stationary. They are created in such a manner that the center of the cell platform lies on the center line passing through the fiducial marks. While the cell platform is stretched, the deflection between the centers of the platform to the fiducial marks can be noted with the help of imaging. Hence, with this data the resolution of the displacement measurement was found to be 50 nm. The spring constant of the folded cantilever beams is calculated using standard beam theory. The in-plane stiffness of the sensor springs was calculated using AFM.

A standard probe station was assembled which constituted of the cell platform, actuator, sensor, cell placement equipment, and image acquisition. The cells which were used for experimental purposes were the hamster fibroblast cells. These cells were cultured in T75 cell culture medium inside the incubator at 37 °C. Once the cell monolayers reach 80% of their confluent growth, they were ready for experiments and were

setup on the cell platform with some solutions. The cell adheres to the cell platform on its own in about one to three hours.

3.2.3.2. Experimental Results:

After the cell was placed on the cell platform, a displacement was induced at 400 nm/s. The force is then calculated using $F_{\text{cell}} = k_{\text{spring}} * d_{\text{sensor}}$. As the platform keeps stretching, the cells start to de-adhere which means the adhesion begins to fail. The force at which these failure starts is 1330 nN. The cell is further stretched and the cell completely breaks at 1551 nN. This high force required to break the cell completely is due to multiple reasons such as surface roughness of the platform, shear force applied to the cell and the protein layer used to improve the adhesion.

This device successfully measured the force response of the cell by stretching it. Hence, this device is broadly applicable to various cell mechanics experiments, static strain experiments and static de-adhesion experiments.

After discussing the different MEMS techniques for both nano-material testing and cell mechanics, we will venture into the fabrication of the first bio-MEMS device (Yang et al, 2007) discussed in this section.

Chapter 4

Bio-MEMS Force Sensor Fabrication

This chapter discusses the fabrication of the MEMS force sensor which will be used to measure the force response of a living cell. This device was originally designed by Dr. Taher Saif and Dr. Shengyuan Yang from University of Illinois Urbana Champaign (Yang et al, 2007). The initial resource to start the fabrication was from the work of Dr. Taher Saif, but we used different fabrication methods. Initially (100) p-type Si wafers were purchased from Silicon quest International. The initial inventory requirement consisted of the wafers and the clear-field mask which was ordered from Bandwidth Foundry Inc. See Appendix I and Appendix II for the mask properties and the quotation respectively. Figure 4.1(a) shows the clear-field mask pattern which was used.

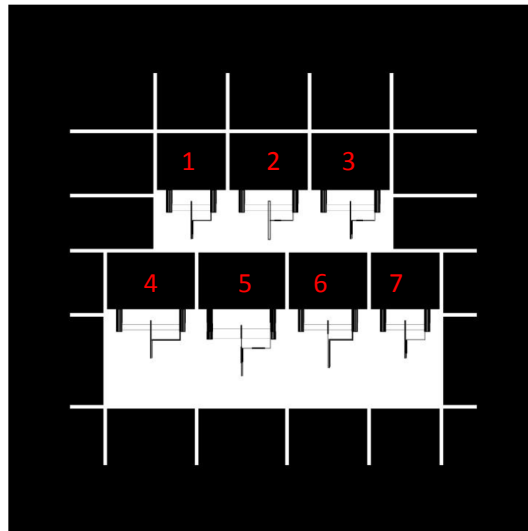


Figure 4.1(a): Pattern of the clear-field mask, showing the devices with different dimensions. Hence, this shows there can be seven devices fabricated in one wafer.

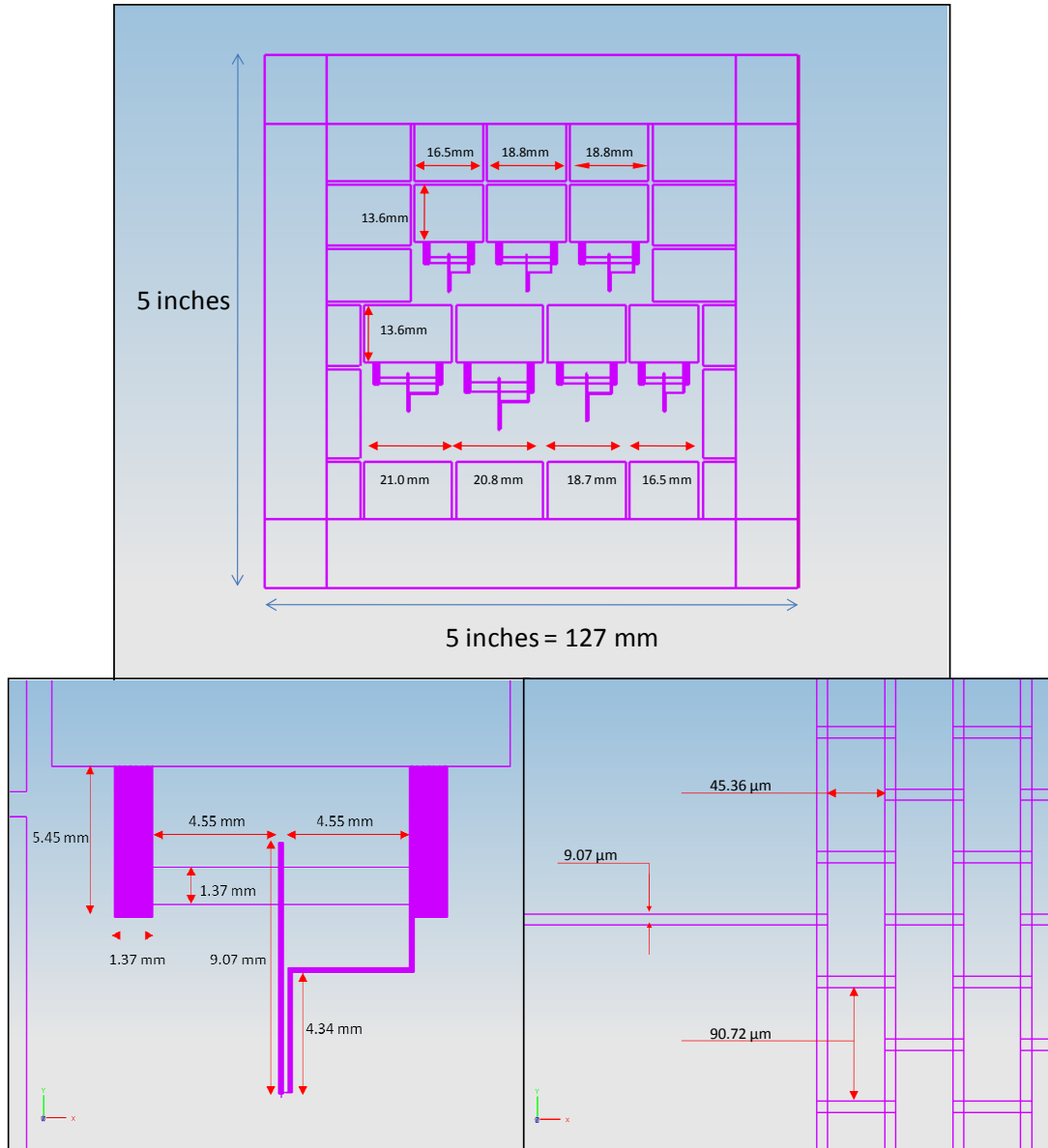


Figure 4.1: (b) shows the outer dimensions of the mask. (c) and (d) shows the device dimensions. The smallest feature being the force sensor beam at 9 μm

Figure 4.1 (b), (c), and (d) shows the dimensions of the mask, and the important dimensions on the device. The smallest feature on the device/mask is the width of the force sensor beam which is 9.07 μm .

The Micro-fabrication facilities at Michigan Tech (www.microfab.mtu.edu) were utilized to fabricate the MEMS device. The initial reference to begin the fabrication procedure was inspired from the process utilized by the scientists in UIUC. Further changes to the process were made according the availability of facilities here at Michigan Tech. The planned fabrication steps are as follows:

1. Silicon dioxide layer will be either grown or deposited on the bare silicon wafer. The thickness of the oxide layer would be 1 micron. Thermal oxide growth would be preferred over sputter deposition as it is a much cleaner process.

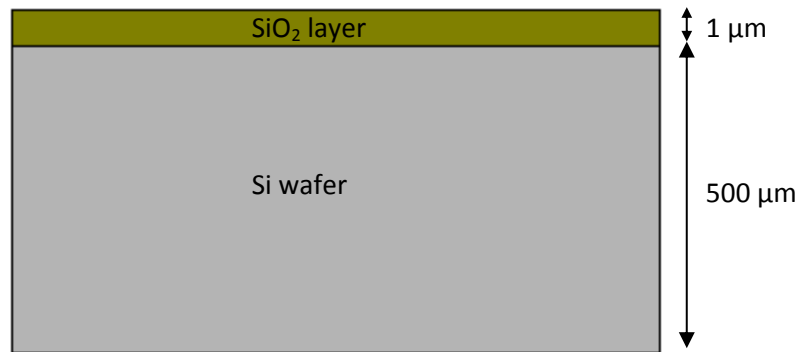


Figure 4.2: Schematic of step 1 of fabrication process

2. The next step would be to spin coat the photo resist over the SiO₂ layer and soft bake it. For this process, we would require a positive photo resist (PR).
3. Using the clear-field mask, lithography would be performed to pattern the wafer substrate.

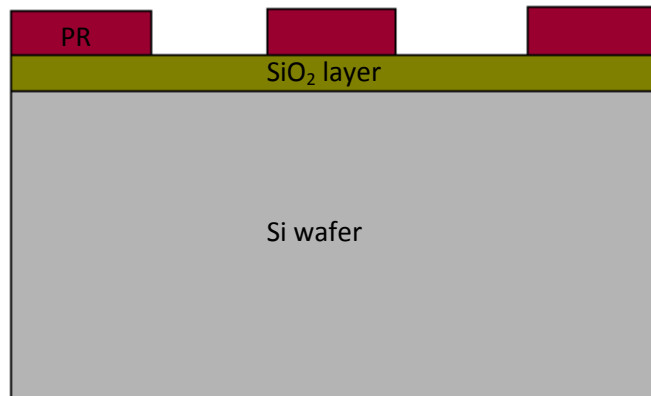


Figure 4.3: Schematic of step 3 of fabrication process

4. The next step was to perform Deep Reactive ion-etch, using PR and the oxide as the masks. The DRIE was planned such that we etch 20 microns deep as shown in the schematic below.

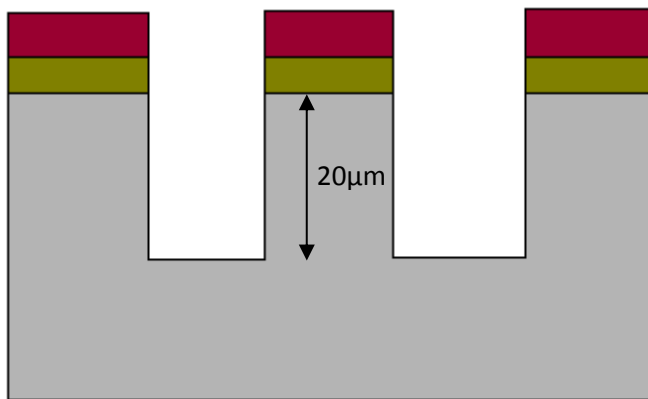


Figure 4.4: Schematic of step 3 of fabrication process, showing the cross section.

5. After etching, remove the photo-resist if it is still present, using acetone and isopropanol.
6. Grow another 150 to 300 nm layer of thermal oxide to act as a mask on the sidewalls. This layer will act as a protective layer on the sidewalls.

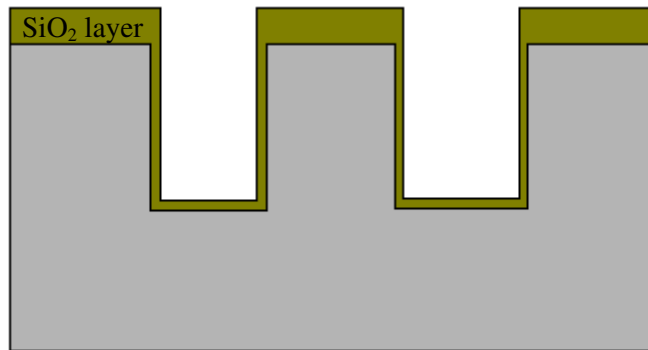


Figure 4.5: Schematic of step 6 of fabrication process,

7. Perform another ICP-RIE etch for 5 μm to etch through the oxide base and expose the silicon.

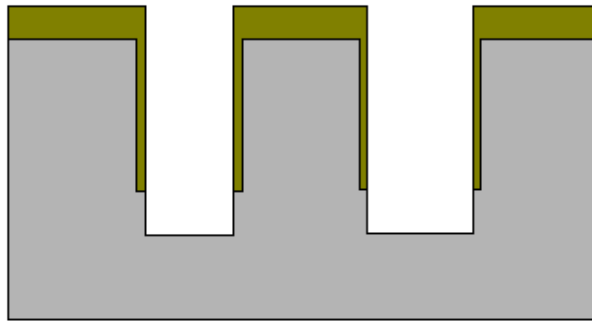


Figure 4.6: Schematic of step 7 of fabrication process.

8. SCREAM Process: Perform isotropic etch to expose to cantilever as shown in the schematic below. Etchant used is a mixture of hydrofluoric acid, nitric acid and glacial acetic acid which is termed as HNA in the ratio 1:3:8.

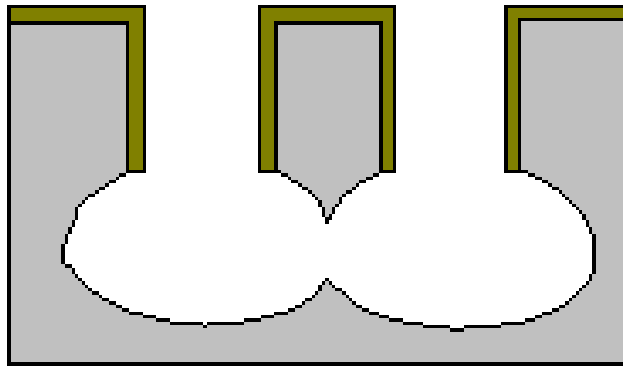


Figure 4.7: Schematic of step 8 of fabrication process.

9. SiO_2 removal: Use buffered HF to remove the SiO_2 layer to complete the device fabrication.

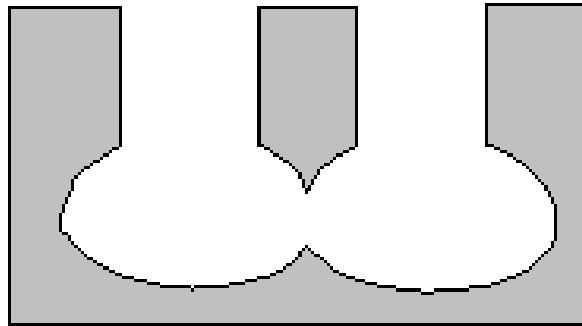


Figure 4.8: Schematic of step of fabrication process after the cantilevers have been obtained and SiO_2 is removed.

Hence, this was the fabrication process which was planned to start the experimentation. Now we will discuss each step in detail with the characterization results.

4.1. Oxidation:

Two different methods of oxides were tried on a bare silicon wafer. As dry thermal oxide growth was a very slow process. The oxide layer thickness which was required was 1 micron and as discussed in Chapter 2 Figure 2.2, the time that would take to grow 1 micron thick oxide would be in the order of 10^4 minutes, which is not possible to achieve with our facilities.

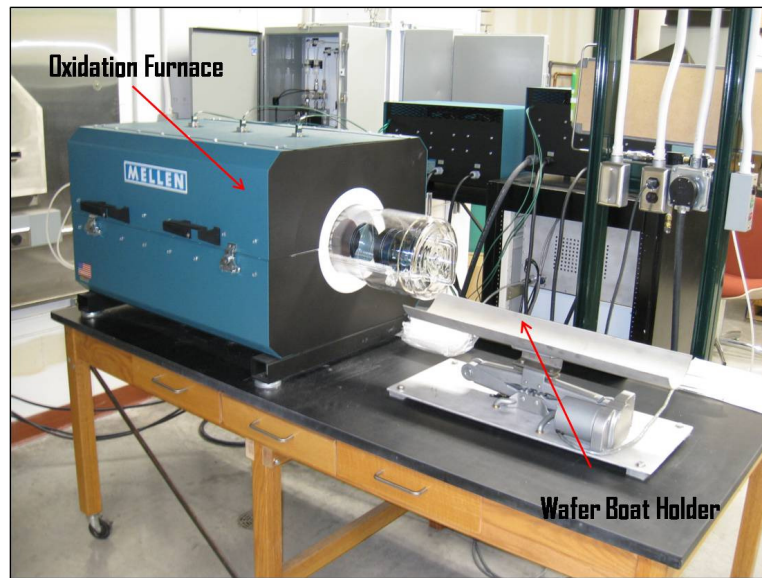


Figure 4.9: Mellen Furnace to perform dry thermal oxidation. The temperature at which the oxidation was performed was 1050 °C.

Initially we tried to grow dry thermal oxide as theoretically the dry thermal oxide is the purest form of oxide on the silicon wafer. Two (100) Si wafers were used and were put in the wafer tray. Thermal oxidation was carried out at 1050 °C for 5 hours inside the MELLEN furnace located in the Temperature processing lab in the 4th floor of the

Material Sciences Building at Michigan Tech. Figure 4.9 shows the picture of the furnace in the lab.

From figure 4.10, we can say that ideally the oxide thickness achieved would be approximately 290-300 nm. After completing the oxidation step and the samples were left in the furnace overnight for cooling purposes.

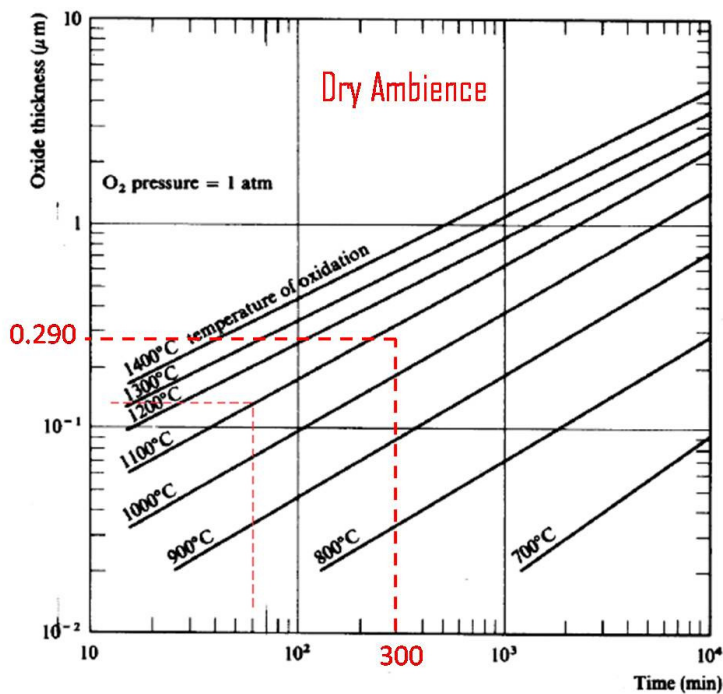


Figure 4.10: Oxide thickness vs. time plot for dry ambience.. Oxidation kept for 5 hours which is 300 minutes at 1050°C . Oxide layer of thickness of approximately 290 nm should have been formed. (Ghandhi, 1994)

The samples were taken out from the chamber the next day and the oxide thickness was measured with the help of filmetrics tool. Figure 4.11 (a) shows the Image of the Filmeteics tool which is present in the Powder Characterization lab in the 5th floor of the Material Sciences Building at Michigan Tech.

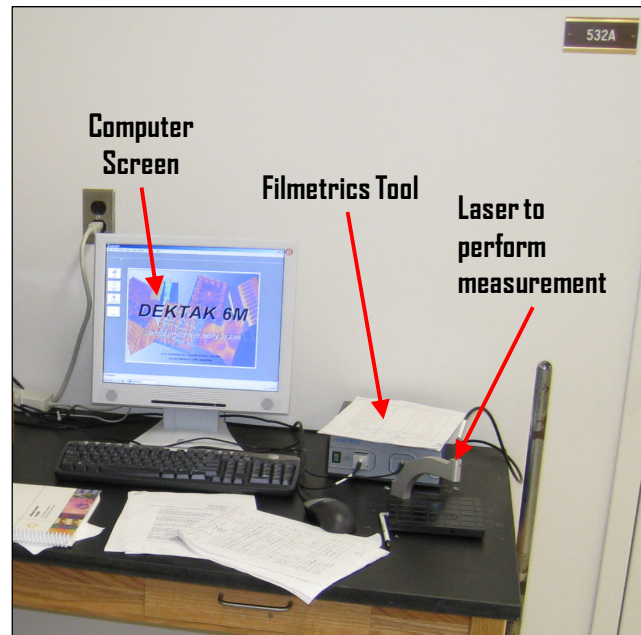


Figure 4.11 (a): Filmetrics tool which measures the oxide thickness located in the powder characterization lab at Michigan Tech.

This tool measures the thickness of the layer over a substrate using the concept of reflectance. Each material has its own reflectance value. Figure 4.11 (b) shows the thickness of the oxide obtained of 258.06 nm with 99.945% accuracy.

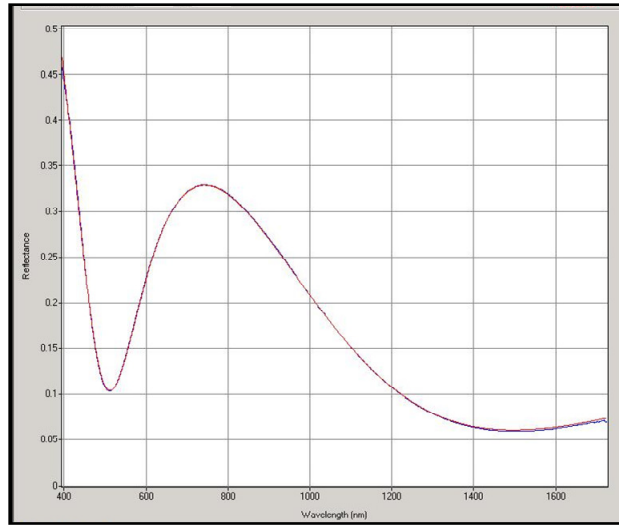


Figure 4.11(b): Oxide Thickness measured after the thermal oxidation using Filmetrics. The thickness measurement was 258 nm with a goodness of fit of 0.99945 which means the reading is extremely accurate.

Now considering the process requirements, SiO_2 acts as a mask while the etching process takes place. Now, 258 micron thick oxide layer is not a sufficiently thick layer to sustain during etching. There is a requirement of a thicker mask. Hence, sputtering of silicon dioxide was tried to achieve a thicker layer.

Sputtering: As discussed in chapter 1, sputtering is the deposition of a source on to the target by bombarding the source molecules with the help of plasma. The Figure 4.12 shows the picture of the instrument used to sputter the oxide on to the wafers. The system is a Perkin-Elmer 8 inch sputter system. The instrumentation layout is as shown in the Figure 4.12.

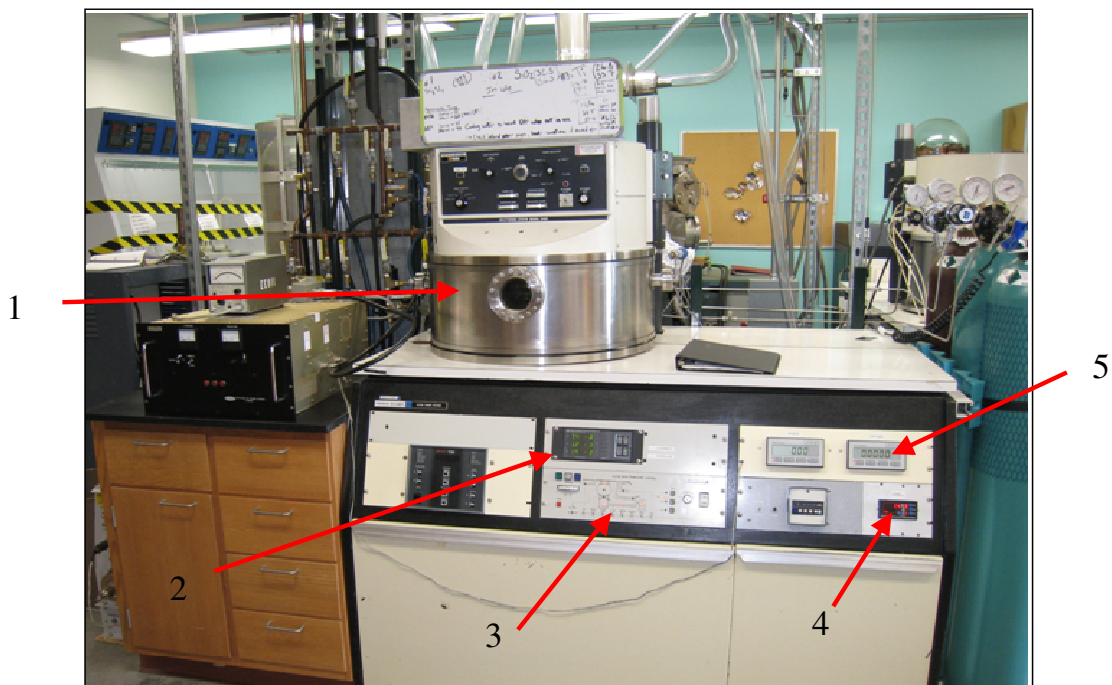


Figure 4.12: Perkin-Elmer 8 inch sputter tool which was used to deposit one micron thick SiO_2 layer. The arrows show different parts of the instrumentation.

Instrumentation Layout:

1. The vacuum chamber and the glass view port.
2. Granville Phillips 307 vacuum gage controller
3. Ultek Auto Pumpdown controller (see figure 4.13 for more information)
4. Teranova Baraton capacitive manometer gage controller.
5. Mass flow controllers showing the flow of oxygen and argon.

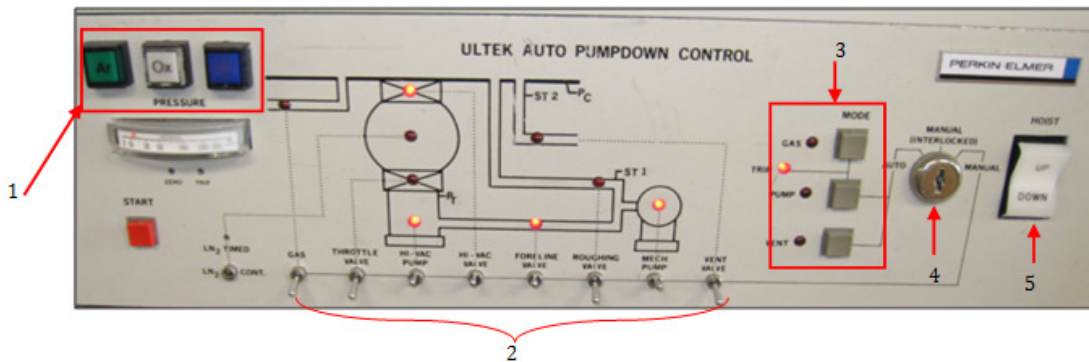


Figure 4.13: Ultek Auto Pumpdown control panel.

1. Gas selection switches (argon, oxygen and nitrogen)
2. Manual Switches- used to control the pumps and valves in manual and interlocked operation.
3. Mode selection buttons – used in automatic operation to select the appropriate mode.
4. Protection level selection key – sets the level of protection to auto, manual and interlocked.
5. Hoist controller which is used to raise and lower the head of the vacuum processing chamber when loading and unloading samples substrates.

The gas flow system will automatically flow the desired gases into the chamber as per the requirement. The plasma is generated inside the chamber which contains different sources such as silicon dioxide, silicon nitride, and aluminum etc. Silicon dioxide was chosen and the deposition was started. The parameters used were from previously

characterized data. The deposition rate for SiO_2 was 200 nm per minute. The oxide thickness achieved was about 1042 nm, which was measured using filmetrics. Figure 4.14 shows the measured result from filmetrics with an accuracy of 99.802%.

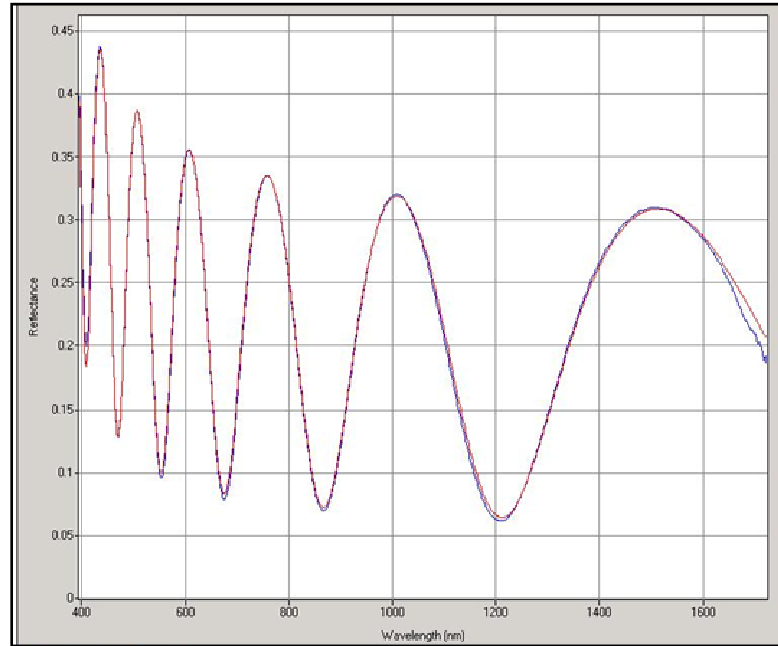


Figure 4.14: Oxide Thickness measured after sputtering using Filmetrics. The thickness measurement was 1045.4 nm with a goodness of fit of 0.99802 which means the reading is extremely accurate.

Thermal oxide: As we discussed before, dry thermal oxide was tried and the thickness on the order of a micron was not achieved. Hence, to achieve 1 micron thick oxide layer, we had to perform wet oxidation. Due to time constraint, ten (100) single sided polished wafers, with 1 micron thick thermal oxide was purchased from Silicon Quest International. See Appendix IV for the quotation for the silicon wafers showing the properties of the wafers. After receiving the wafers, the oxide thickness was measured

and it came out to be 975 nm. Figure 4.15 shows the measured result from filmetrics with an accuracy of 99.398%.

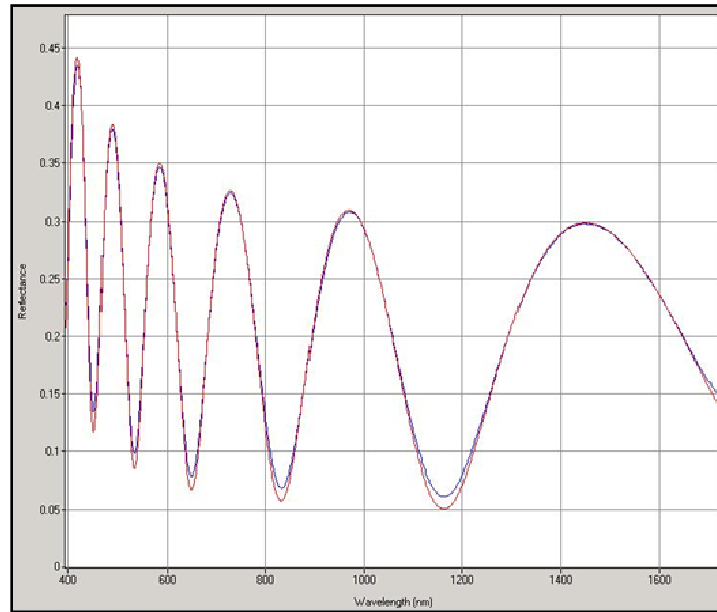


Figure 4.15: Oxide thickness measured after thermal oxidation using Filmetrics. The thickness measurement was 975 nm with a goodness of fit of 0.99398 which means the reading is extremely accurate.

4.2. Photo-lithography:

As discussed in the chapter 1, photolithography is a process in micro-fabrication which selectively removes parts of the thin film called photo-resist, to expose the bulk of the substrate. The first step in the lithography procedure is the spin coating of the photo resist. But before that we should select the appropriate photo-resist, for our fabrication purposes. The type of photo-resist depends on the type of the mask that is being used and

the smallest feature size on the pattern on the mask. A clear field mask will have chrome in the patterned areas and the un-patterned regions will be clear, and in a dark field mask, the patterned regions will be clear, and the remaining areas will be chrome. Hence, the effect of a clear field mask with positive photo-resist would be opposite to that of a dark field mask with positive photo resist, and vice-versa. Figure 4.16 explains the concept of masks clearly.

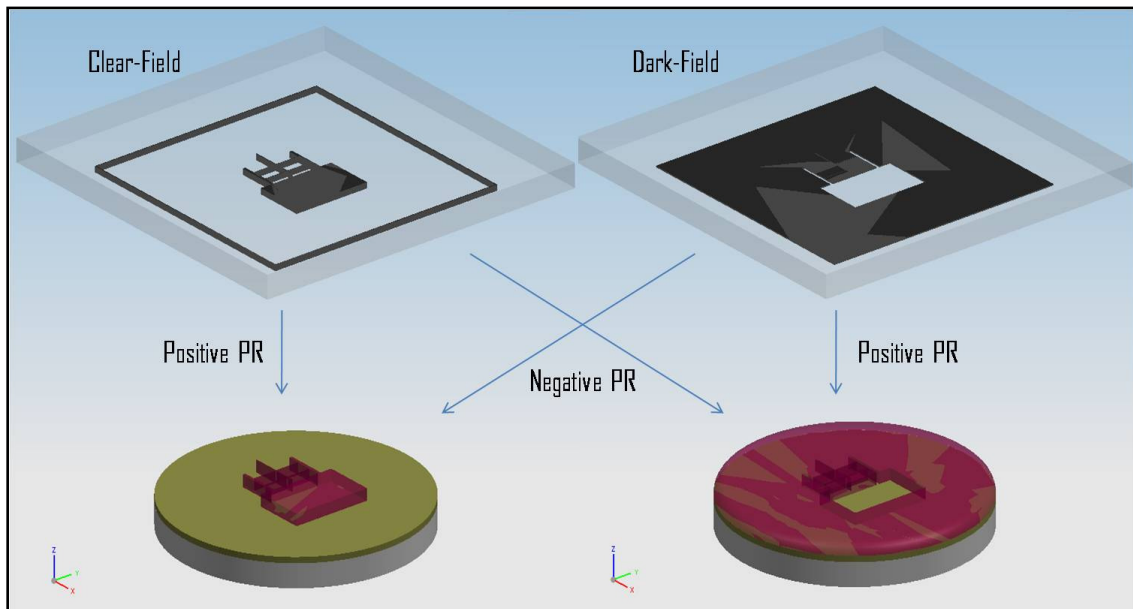


Figure 4.16: Figure shows the distinction between clear field mask and dark field mask and the effect of the positive and negative PR on the resulting pattern. In a clear field mask, patterned region is chrome and the remaining region is glass, whereas in a dark field mask patterned region is glass and the remaining region is chrome. When clear field mask is used with a positive PR, then the areas exposed to UV radiation would get removed while developing.

From Figure 4.1 which shows the layout of the mask which was used, we can see that our mask is a clear field mask and depending on the pattern, we would be using a positive photo-resist. The next step in the micro-processing is reactive ion etching.

Hence, from basic theories of MEMS, photo-resist should act as a good mask in the RIE environment. Table 4.1 shows the photo-resists that were available for use and their properties which are characterized previously.

Table 4.1: Table showing different photo-resists used for characterization and their properties. The thickness values obtained from the company through previous characterization results.

<u>Photo-resist</u>	<u>Polarity</u>	<u>Thickness</u>	<u>Developer</u>	<u>Comments</u>
<i>Shipley SC 1827 with HMDS</i>	Positive	2-3 μm	MF-319	Accepted for characterization
<i>P-Futurrex PR-2000</i>	Positive	2 μm	Futurrex developer	Accepted for characterization
<i>AZ-P4620</i>	Positive	10-17 μm	AZ- 400K	Accepted for characterization
<i>SU-8</i>	Negative	25-30 μm	SU-8 developer	Rejected

Now, we will discuss the characterization results of each of the following photo-resists in detail.

4.2.1. Shipley SC 1827:

This photo-resist is a polymer compound which changes in chemical composition while reacting with UV radiation. The polymer is compositionally divided into the following parts:

- Diazo photoactive compound
- Nonionic surfactant

- Mixed cresol novolak resin
- Electronic grade propylene glycol monomethyl ether acetate
- Cresol (Material Safety Data Sheet)

Here are some of the physical and chemical properties of the polymer compound SC 1827. See Appendix V for more details on the properties of the polymer.

- Appearance:
 - Form: Viscous liquid
 - Colour: Red
 - Odor: Sweet
- pH: neutral
- Boiling Point: 146 °C

The developer used for SC 1827 is MF-319. From the previously characterized data it was found that the thickness of the photo-resist achieved was about 3 microns. But as the next step in micro-fabrication process is RIE, we would like to have a thicker photo-resist layer to support etching and the pattern. Hence, different characterizations were performed in the quest to obtain a thicker layer of photo-resist. Below are the different attempts to spin coat the SC 1827 and to measure the PR thickness.

Initially, the (100) silicon wafers without the thermal oxide were used for photo-resist characterization purposes. One of the properties of SC1827 is that, it does not

adhere to silicon or silicon dioxide. Hence, a chemical called HMDS (hexa methyl di silazane) is used as an adhesive.

The initial values for the process parameters were obtained from previously characterized results. The following steps were followed to spin coat the photo-resist. All the steps below are performed under the fume hood in the clean room. Figure 4.17 shows the laboratory setup which was used for the spin coating purpose.

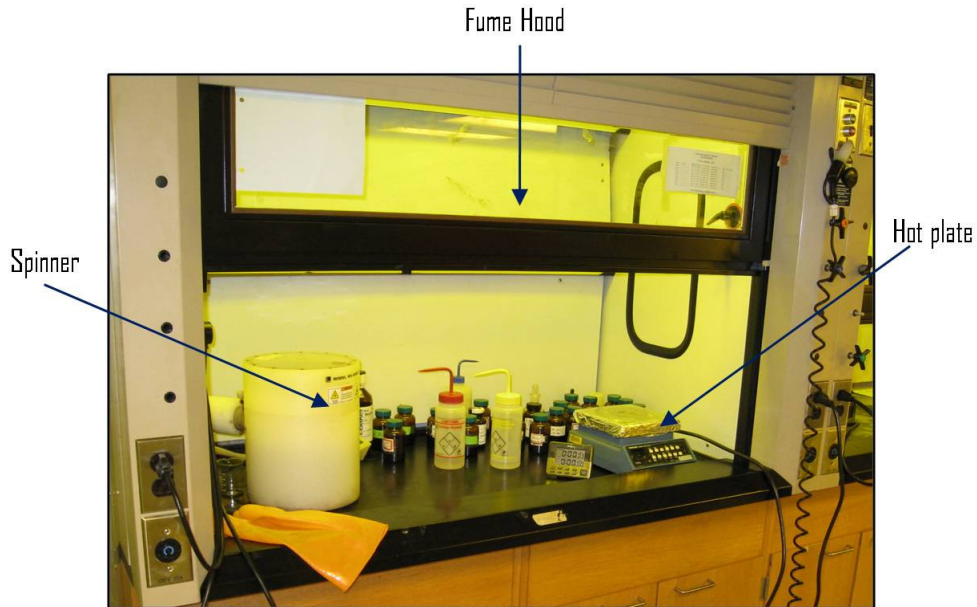


Figure 4.17: Picture showing the Fume hood inside the clean room. The equipments necessary for performing the spin coating of any photo-resist are a hot plate, spinner and the necessary chemicals.

Characterization Results: Spin coating procedure:

- Set the hot plate at 120°C
- Clean the substrate with acetone and iso-propanol (IPA).

- Place the substrate on the hot plate and pre-bake for 60 seconds at 120⁰C.
- Let the substrate cool down to room temperature.
- Spin coat HMDS on the substrate spinning at 4000 rpm for 1 minute.
- Spin coat SC 1827 on the substrate spinning at 4000 rpm for 1 minute.
- Place the substrate on the hot plate and soft bake for 4 minutes at 120⁰C.
- Now the substrate is ready for lithography.

Lithography basically is the process of exposing the substrate with the photo-resist to the UV radiation. The lithography facility is present inside the clean room. The UV lamp voltage range: 0 to 200 V (the voltage set at 60 V), Lamp intensity range: 0 to 750 W (the power set at 360 W). The substrates used are all 4 inch Si wafers; the mask size is 5 inch by 5 inch. There are different types of contact between the mask and the substrate. Hard contact is the type of contact where there is a physical contact between the mask and the substrate. Soft contact is a type of contact where there is a minimum distance of 50 microns kept between the mask and the substrate. Proximity contact is a type of contact where there needs to be a separation distance between the mask and the substrate. These different types of contacts can be used to manipulate the dimensions on the pattern.

In this case, the following lithography properties were used:

- Contact mode: Soft contact with a separation of 50 microns.
- Exposure Time: 12 seconds

Chapter 4- Bio-MEMS Force Sensor Fabrication

- After the lithography is complete, place the substrate on the hot plate for a post-exposure bake for 1 minute at 120⁰C.
- Develop the photo-resist until the resist from the exposed region is completely removed. This will take about 8 minutes.
- Check the features under the optical microscope.
- Once all the features are well developed, place the substrate on the hot plate and hard bake it for 2 minutes and 30 seconds at 120⁰C.

Now, the thickness of the photo-resist layer is measure under the DEKTAK-6M profiler. Figure 4.18 shows the image of the DEKTAK 6-M profiler located in the Powder characterization lab in the 5th floor of the Material Sciences Building at Michigan Tech.

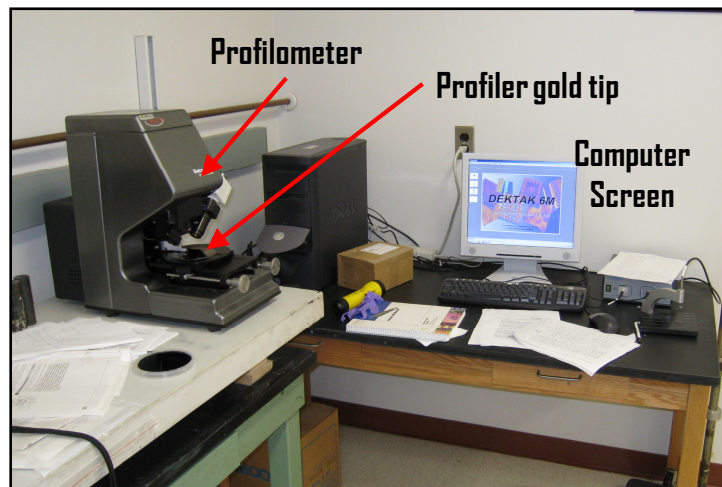


Figure 4.18: DEKTAK 6M Profiler used to measure the step profile of the etched material on the substrate. It is located in the Powder Characterization lab at Michigan Tech.

The next step in the characterization was to try to achieve thicker photo-resist thickness than 2.85 microns. Hence, the spinning rate of the photo-resist was reduced from 4000 rpm to 3000 rpm. As we know, theoretically by reducing the speed the thickness of the spun layer will increase.

The same spin coating procedure was followed as mentioned in the above case with the change in the spin speed of SC 1827 from 4000 rpm to 3000 rpm for 1 minute. Soft bake the substrate for 4 minutes at 120 °C. Figure 4.19 shows the photo-resist thickness obtained on the features from this process.

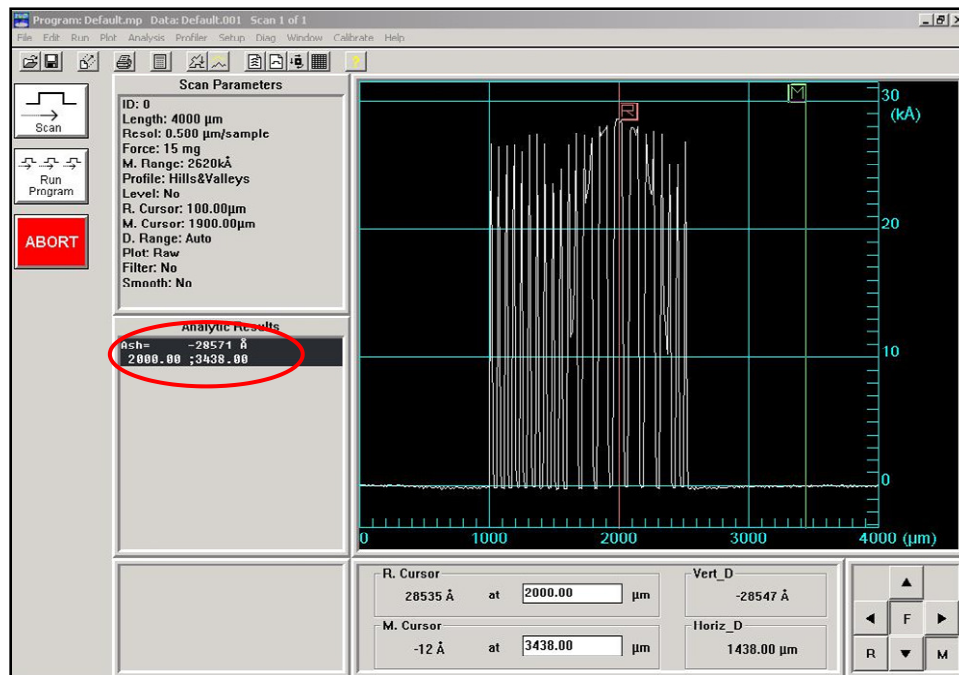


Figure 4.19: Plot showing the path of the gold tip of the profilometer following the path over the features and over the photo-resist region and the substrate intersection. The thickness result is given to be $28571 \text{ \AA} = 2.85 \text{ }\mu\text{m}$. Hence, the approximate thickness of the photo-resist is 2.85 μm .

As the spin speed is reduced, assuming the thickness of the photo-resist has increased, the UV exposure time during the lithography was set to 15 seconds. Using the developer MF-319, the substrate was kept for developing. The development time obtained was about 18 minutes. Then the substrate was placed on the hot plate for 2 minutes and 30 seconds at 120 °C. The thickness results were a little unexpected. The thickness value of the photo-resist was about 3.25 microns on the intersection of photo-resist and the substrate. The thickness of the photo-resist on the features was found to be 2.5 microns. Figure 4.20 shows the profilometer results of the thickness measurements.

As there was no significant change in the thickness of the photo-resist found, the next idea in the characterization of SC 1827 was trying double layer of photo-resist to obtain a thicker layer. The same spin coating procedure was followed as mentioned in the first case.

- Set the hot plate at 120 °C
- Clean the substrate with acetone and iso-propanol (IPA).
- Place the substrate on the hot plate and pre-bake for 60 seconds at 120 °C.
- Let the substrate cool down to room temperature.
- Spin coat HMDS on the substrate spinning at 4000 rpm for 1 minute.
- Spin coat SC 1827 on the substrate spinning at 3000 rpm for 1 minute.
- Place the substrate on the hot plate and soft bake for 3 minutes at 120°C.

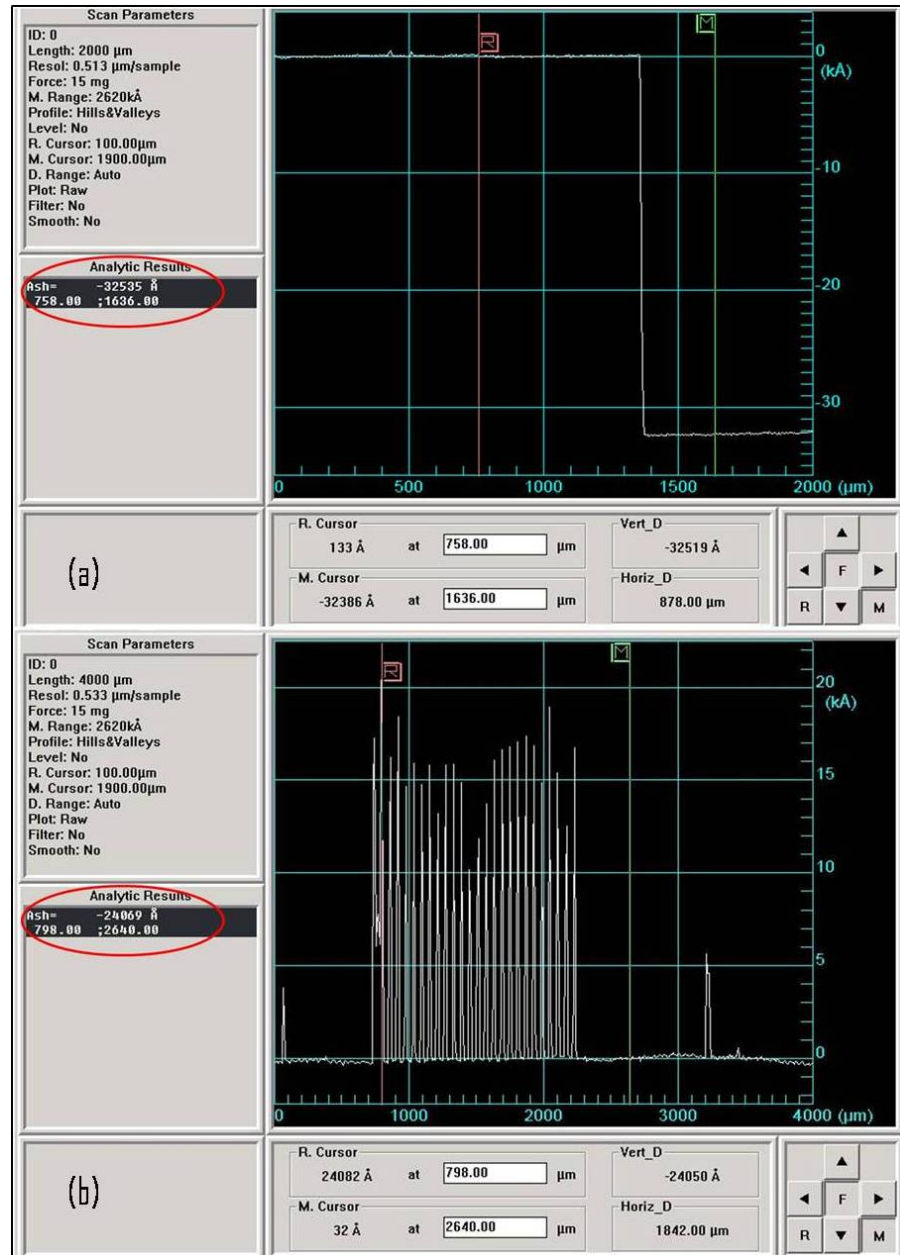


Figure 4.20: (a) Plot showing the path of the gold tip of the profilometer following the path over the photo-resist region and the substrate intersection; the thickness result is given to be $32535 \text{ Å} = 3.25 \mu\text{m}$. (b) over the features; the thickness result is given to be $24069 \text{ Å} = 2.41 \mu\text{m}$.

- Spin coat again a second layer of SC 1827 on the substrate spinning at 3000 rpm for 1 minute.

- Place the substrate on the hot plate and soft bake for 4 minutes at 120⁰C
- Now the substrate is ready for lithography

Again the exposure time during lithography was increased to 30 seconds as there were 2 layers of photo-resist. The substrate is kept for a post-exposure bake for 1 minute at 120⁰C. An interesting development took place at this juncture of experimentation. The substrate was kept for development in the MF-319 developer. The photo-resist completely developed within 4 minutes and 15 seconds. The substrate was then placed on the hot plate for 2 minutes and 30 seconds for hard baking at 120⁰C.

The substrate was then taken to the DEKTAK 6M profilometer for thickness measurement. Interestingly, the thickness measurement was between **2.8 microns and 3 microns**. Hence, we conclude that SC 1827 photo-resist would achieve only about 2.8 to 3 microns thickness.

Figure 4.21 (a) shows the spin speed curve obtained from the data collected by Shipley Company. Note: Spin coating of SC 1827 was performed by changing the spin speeds and the exposure times. But as the spin speeds were reduced below 2000 rpm, the development of the photo-resist was hampered. The features could not be formed with the required resolution. Hence, the thickness of the photo-resist Sc 1827 was concluded to be 2.8 to 3 microns for our feature sizes.

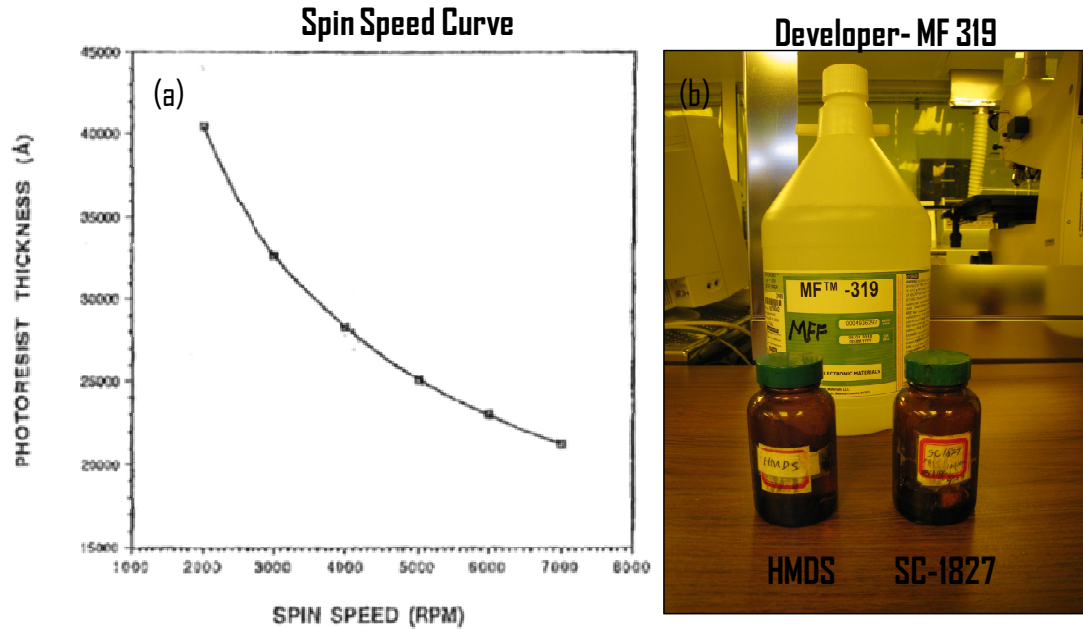


Figure 4.21: (a) Spin speed vs. the thickness obtained plot, shown for SC 1827 photo-resist. Characterization performed by Shipley Co. (See Appendix V). (b) SC-1827, HMDS and the developer MF-319 placed inside the clean room.

4.2.2. P- Futurrex: PR-2000

PR 2000 is a positive photo-resist which ideally has a thickness of 2000 nm. Some PR-2000 properties show that, it has a superior resolution capability, short exposure and development time, superior temperature resistance and a good shelf life. All futurrex compounds have a common developer called the Futurrex developer. The characterization of Futurrex PR-2000 was performed to obtain a good resolution and 2 micron thickness.

Spin coating procedure:

- Set the hot plate at 100 °C

Chapter 4- Bio-MEMS Force Sensor Fabrication

- Clean the substrate with acetone and iso-propanol (IPA).
- Place the substrate on the hot plate and pre-bake for 60 seconds at 100 °C.
- Let the substrate cool down to room temperature.
- Spin coat HMDS on the substrate spinning at 4000 rpm for 1 minute.
- Spin coat PR-2000 on the substrate spinning at 2000 rpm for 1 minute.
- Place the substrate on the hot plate and soft bake for 5 minutes at 100°C.
- Let the substrate cool down to room temperature.
- Now the substrate is ready for lithography

Figure 4.22 shows the PR-2000 photo-resist and its developer placed in the clean room.



Figure 4.22: Picture showing the photo-resist P-Futurrex in the

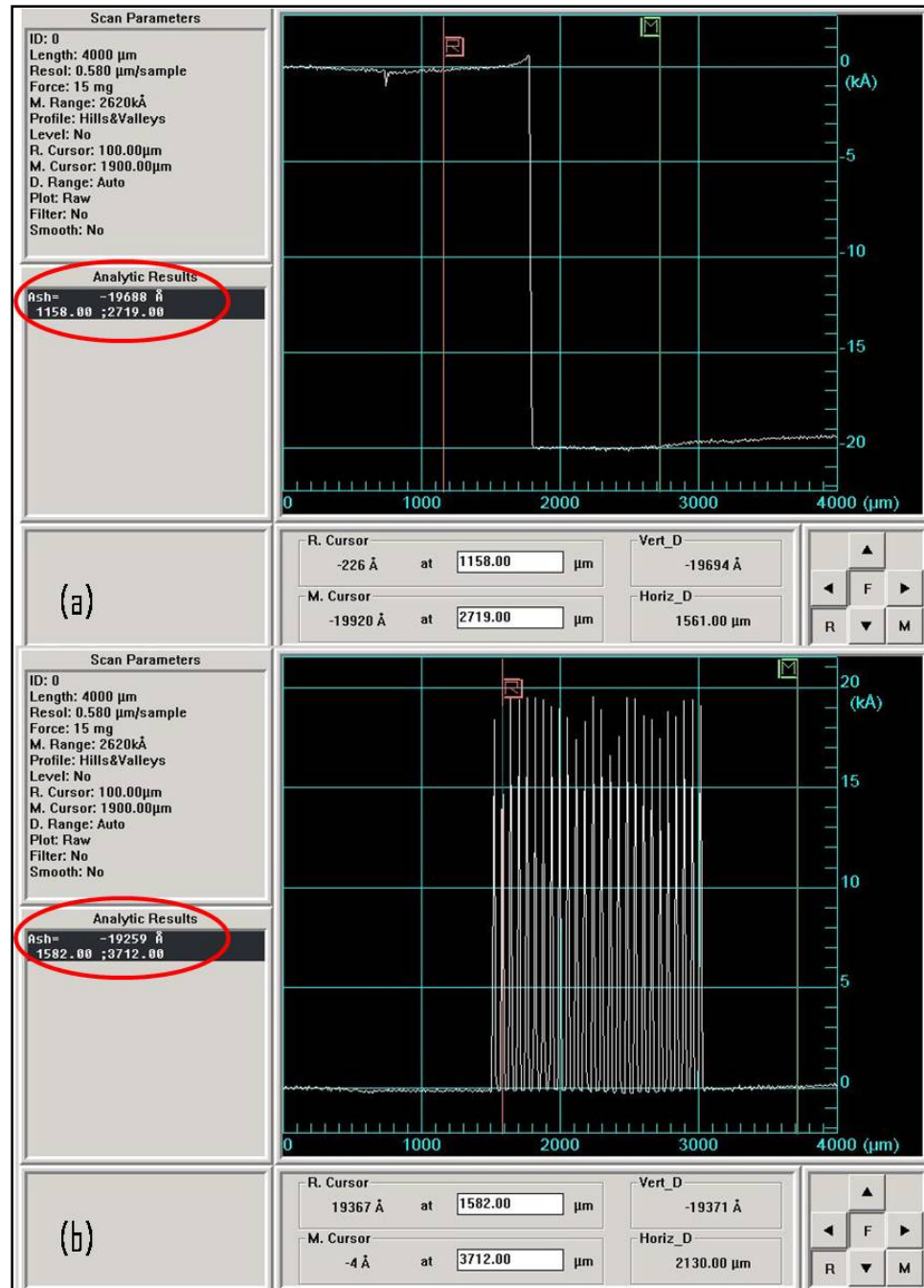


Figure 4.23: (a) Plot showing the path of the gold tip of the profilometer following the path over the photo-resist region and the substrate intersection; the thickness result is given to be 19688 Å = 1.97 μm . (b) over the features; the thickness result is given to be 19259Å = 1.93 μm .

As the mask remains the same, the wafer size remains the same; the only parameter that needs to be changed during lithography is the exposure time. The exposure time is set at 12 seconds, a value obtained from previous characterizations. The contact mode is soft contact with a separation of 50 microns. The substrate is then transferred to the Futurrex developer solution. It was developed for about 4 minutes and 15 seconds and then placed on the hot plate for about 2 minutes at 100 °C. The thickness is then measured using DEKTAK-6M profiler. Figure 4.23 shows the profilometer reading for the PR-2000 photo-resist thickness on the resist-substrate interface and on the features. Hence, the thickness of the PR-2000 photo-resist is found to be very consistent at 2 microns.

4.2.3. AZ-P4620

Figure 4.24 shows the AZ-P4620 bottle kept in the clean room.



Figure 4.24: Picture showing the photo-resist AZ-P4620 in the clean room

Spin Coating procedure:

- Set the hot plate at 120 °C
- Clean the substrate with acetone and iso-propanol (IPA).
- Place the substrate on the hot plate and pre-bake for 60 seconds at 100 °C.
- Let the substrate cool down to room temperature.
- Spin coat HMDS on the substrate spinning at 4000 rpm for 1 minute.
- Spin coat AZ-P4620 on the substrate spinning at 1000 rpm for 1 minute.
- Place the substrate on the hot plate and soft bake for 4 minutes at 120°C.
- Let the substrate cool down to room temperature.
- Now the substrate is ready for lithography

The exposure time for the lithography is set to be 30 seconds, the contact mode being soft contact with the separation of 50 microns. The developer for this photo-resist is AZ-400K. After about 8 minutes the relatively larger areas are developed. When viewed under the microscope the smaller features are not developed. But the thickness measured using the DEKTAK-6M profilometer is found to be about 10 microns. Figure 4.25 shows the profilometer plot measuring the photo-resist thickness.

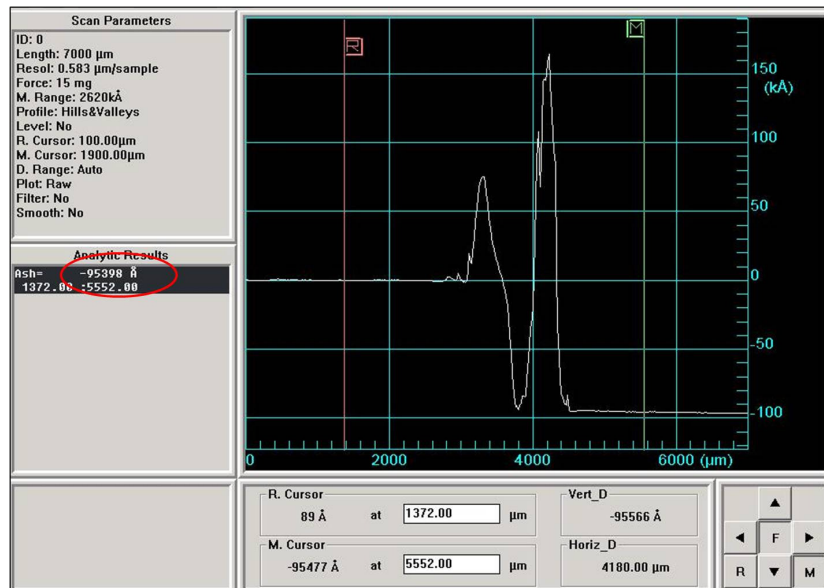


Figure 4.25: Plot showing the path of the gold tip of the profilometer following the path over the photo-resist region and the substrate intersection; the thickness result is given to be $95398 \text{ \AA} = 9.54\mu\text{m}$.

Now after the photo-lithography step we can find seven samples in one wafer as shown in the Figure 4.1. Hence, the wafer was diced into seven pieces. Figure 4.26 below shows the dicing saw machine which was used for dicing all the samples.



Figure 4.26: Automated Dicing System which was used for all the dicing purposes.

Result: Figure 4.27 shows the SEM image of the SC1827 Photo-resist patterned on the Si wafer. The thickness of the PR is shown which is consistent with the DEKTAK-6M profilometer readings.

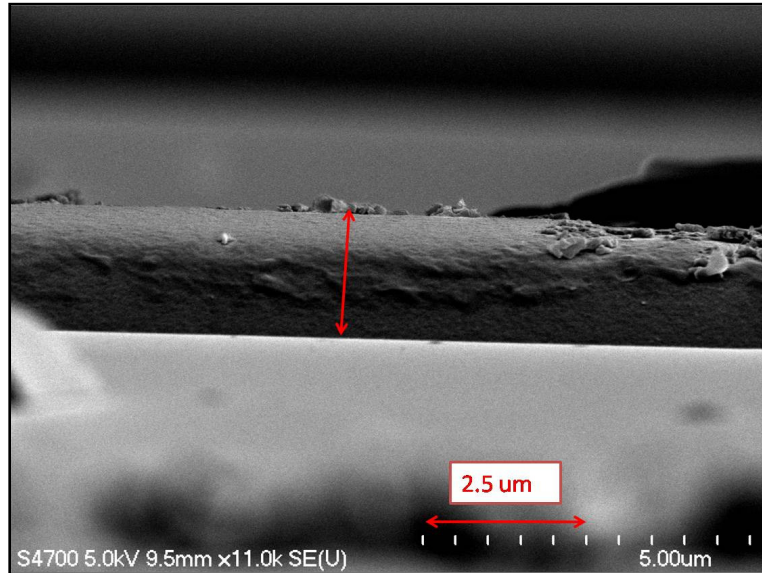


Figure 4.27: SEM image of the SC1827 photo-resist patterned on the Si wafer. The thickness of the layer on the features is about 2.5 μm which is quiet consistent with the DEKTAK-6M readings.

Following Table 4.2 summarizes the results of the three photo-resists we have discussed in this section.

Table 4.2: Characterization results of the three photo-resists for photo-lithography

Photo-resist	Thickness	Comment	Result
SC 1827	2.8 to 3 μm	Good resolution capability	Selected
PR-2000	2 μm	Good resolution capability	Rejected
AZ-P4620	10 μm	Bad resolution capability	Rejected

SC 1827 is the best amongst the three photo-resists, as it has the maximum thickness with the best resolution capability.

4.3. *Silicon Etching:*

The next step in the micro-fabrication and the most critical step is the etching process. There are different types of etching processes viz. isotropic etching, anisotropic etching, reactive ion etching (RIE), and deep reactive ion etching (DRIE). As discussed in the first chapter, the preferred etching process would be the deep reactive ion etching (DRIE). But due to the lack of DRIE facility, the etching process chosen for characterization was RIE. Figure 4.28 shows the laboratory setup of the TRION reactive ion etching system which was used to perform the etch characterizations.



Figure 4.28: TRION ICP-RIE system, which was used for all the etch characterizations. The gas containers shown in the (c) are CF_4 , Nitrogen, Argon, CHF_3 , Oxygen, SF_6 etc.

4.3.1. Reactive Ion Etching

As discussed in chapter 1, RIE is dry plasma etch in which the substrates are etched with the help of gases such as CF_4 and SF_6 , and also RF power which generates the plasma. Here, the substrates are placed at normal position to the gas flow, and are immersed in plasma. In addition, they are normal to the RF field, so that the movement of the ionized particles is both highly directional and rapid. Due to this, a high degree of anisotropic etching will occur. This anisotropic nature can be improved by using chemicals which have reaction products with large ionized components. There is another technique which can be used to enhance the anisotropic nature of the etching. This process is known as Scalloping. In this process, special gas chemistry is utilized to form a

polymer on the sidewalls of the trench as it is being etched. This gas chemistry is known as passivation gas. This thin layer of polymer prevents lateral undercutting and etching of the Si on the side walls resulting in a high aspect ratio etch. This process is often used in DRIE. This process is explained in chapter 2.

In the experiments conducted, specific gas chemistry was used to enhance the anisotropy and get a DRIE type behavior. The gaseous etchants available in the laboratory were carbon tetrafluoride (CF_4) and sulphur-hexafluoride (SF_6). As our masking material is SC 1827, previous RIE etch characterizations show that the presence of SF_6 initiates the crosslinking of the photo-resist polymer, which makes it to adhere strongly to the silicon wafer. This makes it very difficult to remove the photo-resist. Hence, the etchant chemistry which was used contained CF_4 as the primary etchant. Trifluoromethane (CHF_3) was used as the passivation gas for initiating scalloping. Oxygen was the third gas in the etchant gaseous mixture, which improved the etching nature. Hence, the etch chemistry constituted of $\text{CF}_4 + \text{O}_2 + \text{CHF}_3$. The initial aim was to achieve an etch depth of 20 microns. This magnitude of etching had never been done before on the TRION system, hence there were no previous characterization results. When consulted with the TRION Co. to check whether there were any characterizations done on the particular system for such magnitude of etches, there were no results. Below shown are the characterization results. Initially a Silicon wafer with 1 micron thick sputtered oxide is patterned using SC1827 photo-resist. The substrate is diced into 7 samples.

Test 1:

Sample: Silicon wafer with 1 μm sputtered SiO_2 layer patterned with SC 1827 PR

Aim: To check the effect of plasma etching on the photo-resist, and its simultaneous effect on SiO_2 .

Etching duration: 16 minutes

Etch intervals: 180 seconds

Instructions: Check the sample under the microscope for discoloration, after each etch interval.

Etchant chemistry: $\text{CF}_4 = 25$ units; $\text{O}_2 = 5$ units

Initial observation: Using a multi-meter, the conductivity of the sample was measured.

Initially due to the presence of SiO_2 (insulator) there was no conductivity.

Table 4.3: Test 1

Run	Etch interval (sec)	ICP (W)	RIE (W)	PRESSURE (mTorr)	CF4	O2	CHF3	Comments
1	60	100	100	50	45	5	0	
2	180	100	100	50	45	5	0	
3	180	100	100	50	45	5	0	PR color changing to orange from yellow
4	180	100	100	50	45	5	0	Sample is rough.
5	180	100	100	50	45	5	0	
6	180	100	100	50	45	5	0	Sample turns dark and shady.

Chapter 4- Bio-MEMS Force Sensor Fabrication

Conclusion and observations:

- The sample was conducting after the etching sequence after the measurement with the multi-meter. Hence, this shows the SiO_2 has etched away and exposed the Si substrate.
- After cleaning the wafer with acetone, the PR is removed very easily, which shows there is no cross-linking happening and hence, the PR is etching and not burning.
- Due to the possibility of the PR being etched away, there is no possible method to measure the depth of the etch.
- Sputter oxide is very rough and the surface is not clean.

Test 2:

Sample: Silicon wafer with 1 μm sputtered SiO_2 layer patterned with SC 1827 PR

Aim: To check the effect of plasma etching on the photo-resist, and its simultaneous effect on SiO_2 .

Etching duration: 15 minutes

Etch intervals: 180 seconds

Instructions: Chemistry changed, observe the discoloration of PR.

Etchant chemistry: $\text{CF}_4 = 40$ units; $\text{O}_2 = 10$ units; $\text{CHF}_3 = 35$ units

Initial observation: PR thickness = 2 μm

Table 4.4: Test 2

Run	Etch interval (sec)	ICP (W)	RIE (W)	PRESSURE (mTorr)	CF4	O2	CHF3	Comments
1	180	100	150	45	40	10	35	PR dark brown color throughout
2	180	100	150	45	40	10	35	PR turns brownish green, still dark. The silicon oxide is light cream color
3	180	100	150	45	40	10	35	PR turns greener towards the probe and stays brownish green towards the support
4	180	100	150	45	40	10	35	
5	180	100	150	45	40	10	35	A step of 1750 nm observed between the PR and the substrate

Conclusions and observations:

- Filmetrics show the thickness of oxide layer remaining to be as 180 nm.
- PR is either getting burnt or etched away, as the thickness of PR is reducing.
- Possibility of grass formation, which means a polymer deposition, might be happening.
- About 1070 nm of PR being etched away.

Figure 4.29 shows the schematic for the calculation of the amount of PR being etched away.

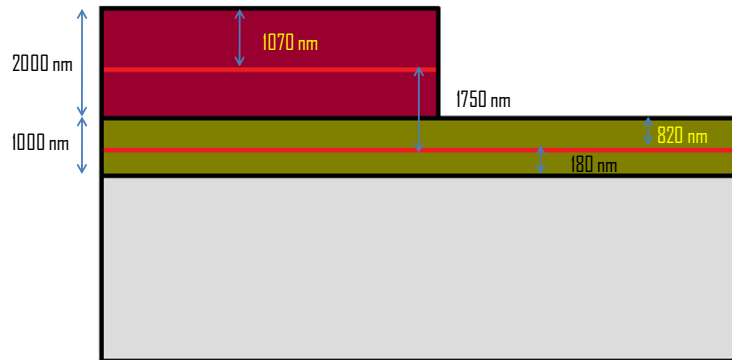


Figure 4.29: Schematic showing the etching of PR as well as SiO₂ taking place. With this set of parameters, PR is etching faster than the SiO₂. PR etch = 1070 nm; SiO₂ etch = 820 nm

Test 3:

Sample: Bare Silicon wafer patterned with SC 1827 PR.

Aim: Use a *glass slide* to cover up a region of the sample, to characterize the silicon etching rate as well as the PR etching rate, and also to check the effect of Oxygen on the etching of the sample.

Etching duration: 8 minutes

Etch intervals: 120 seconds

Instructions: Oxygen content increased. Perform the same test for another 8 minutes to test the repeatability

Etchant chemistry: CF₄ = 40 units; O₂ = 15 units; CHF₃ = 35 units

Initial observation: PR thickness = 1.5 μm at the features

Table 4.5: Test 3

Run	Etch interval (sec)	ICP (W)	RIE (W)	PRESSURE (mTorr)	CF4	O2	CHF3	Comments
1	120	100	150	45	40	15	35	
2	120	100	150	45	40	15	35	
3	120	100	150	45	40	15	35	
4	120	100	150	45	40	15	35	Silicon etch = 750 nm; PR etch = 1.4 μm ; feature height = 850 nm

Conclusions and observations:

- All measurements on DEKTAK-6M.
- Silicon is etching at the rate of 750 to 800 nm in 8 minutes and PR is etching about 1.4 microns in 8 minutes.
- The high oxygen levels might be causing the PR to etch at such a high etch rate.
- After repeating the same test, the results were similar with silicon etching 700 nm in 8 minutes and PR etching about 1.3 to 1.4 microns.
- Hence, we observe a consistency in the repeatability of the system.

Test 4:

Sample: Bare Silicon wafer patterned with SC 1827 PR.

Aim: Use a *glass slide* to cover up a region of the sample, change the etching chemistry and the parameters to characterize the silicon etching rate as well as the PR etching rate.

Etching duration: 8 minutes

Chapter 4- Bio-MEMS Force Sensor Fabrication

Etch intervals: 120 seconds

Instructions: Oxygen content reduced. Perform the same test for another 8 minutes to test the repeatability of the experiment.

Etchant chemistry: $\text{CF}_4 = 45$ units; $\text{O}_2 = 5$ units; $\text{CHF}_3 = 35$ units

Initial observation: PR thickness = $1.5\text{ }\mu\text{m}$ at the features

Table 4.6: Test 4

Run	Etch interval (sec)	ICP (W)	RIE (W)	PRESSURE (mTorr)	CF4	O2	CHF3	Comments
1	120	75	200	45	45	5	35	
2	120	75	200	45	45	5	35	
3	120	75	200	45	45	5	35	
4	120	75	200	45	45	5	35	Silicon etch = 750 nm-800 nm; PR etch = 1000 -1050 nm

Conclusions and observations:

- The results are confirmed by taking original readings of PR thickness which show 1.5 microns between PR and Si, and reading after etch which show 1.3 microns, which gives a 200 nm offset.
- Hence, the PR etch rate has reduced with this chemistry compared to the previous test.
- By repeating the same test on another sample covered with glass slide, we get same results with Si etch being 750 nm in 8 minutes and PR etching 1000 nm in 8 minutes. Hence, a good repeatability is observed.

Test 5:

Sample: Bare Silicon wafer patterned with SC 1827 PR.

Aim: Use a *glass slide* to cover up a region of the sample, change the etching chemistry and the parameters to characterize the silicon etching rate as well as the PR etching rate.

Idea is to reduce the PR etch rate and increase the Si etch rate. Keep etching unless the PR completely gets etched away and exposes the silicon substrate

Etching duration: 24 minutes

Etch intervals: 60 seconds

Instructions: Take readings after every 8 minutes. Keep etching for 24 minutes. Cool the sample after each etch interval for 3 minutes.

Initial observation: PR thickness = 1.5 μm at the features

Etch parameters and etch chemistry:

Table 4.7: Test 5

Sr #	Etch parameters	Units
1	ICP (W)	100
2	RIE (W)	200
3	Pressure (mTorr)	45
4	CF ₄	45
5	O ₂	5
6	CHF ₃	35

Chapter 4- Bio-MEMS Force Sensor Fabrication

Conclusions and observations:

- After the first 8 minutes, silicon etch = 600-650 nm; PR etch = 950-1000 nm
- After 16 minutes, silicon etch = 1100-1200 nm; PR etched away, Si exposed
- The sample cleaned using acetone, to check for the presence of PR. PR completely etched away.
- After 24 minutes of etch with the glass slide, total silicon etch = 1.7 to 1.8 μm

Test 6:

Sample: Silicon wafer with 1 micron thick thermal oxide layer, patterned with SC 1827 PR.

Aim: Use a *glass slide* to cover up a region of the sample, continue with the same previous etch chemistry and the etch parameters. Characterize the thermal oxide etch rate. Etch 1 micron of the oxide layer and 1 micron of silicon substrate below the oxide.

Etching duration: 24 minutes with 60 seconds intervals

Instructions: Take readings after every 8 minutes. Keep etching for 24 minutes. Cool the sample for 3 minutes after each etch interval of 60 seconds.

Initial observation: PR thickness = 2.3 to 2.5 μm at the features

Etch parameters and etch chemistry:

Table 4.8: Test 6

Sr #	Etch parameters	Units
1	ICP (W)	100
2	RIE (W)	200
3	Pressure (mTorr)	45
4	CF ₄	45
5	O ₂	5
6	CHF ₃	35

Conclusions and Observations:

- After the first 8 minutes, thermal oxide (SiO₂) etch = 550 nm and PR etch = 850 to 900 nm.
- After 16 minutes, thermal oxide (SiO₂) etch is in consistent in the DEKTAK-6M profilometer, and filmetrics no oxide thickness. SiO₂ seems to be completely etched away.
- The surface is extremely rough, hence the measurements are inconsistent.
- After 16 minutes, PR etch = about 2.1 μm
- After 24 minutes, surface extremely rough, hence no measurement possible.

Cleaning the sample with acetone shows no presence of photo-resist.

Test 7:

Sample: Silicon wafer with 1 micron thick thermal oxide layer, patterned with SC 1827 PR.

Aim: Use a *glass slide* to cover up a region of the sample, continue with the same previous etch chemistry and the etch parameters to etch away the SiO₂. Change the etch parameters by removing the ICP for the Si substrate etch. Keep etching silicon substrate for 16 more minutes.

Etching duration: 32 minutes

Etch intervals: 120 seconds

Instructions: Take readings after every 8 minutes. Keep etching for 32 minutes in total.

Cool the sample for 5 minutes after each etch interval of 120 seconds.

Initial observation: PR thickness = 2.5 μm at the features

Table 4.9: Test 7

Set	Run	Etch interval (sec)	ICP (W)	RIE (W)	PRESSURE (mTorr)	CF4	O2	CHF3	Comments
1	1	120	100	200	45	45	5	35	SiO ₂ etch = 550 nm PR etch = 900 nm Feature height (after etch) = 2 μm
	2	120	100	200	45	45	5	35	
	3	120	100	200	45	45	5	35	
	4	120	100	200	45	45	5	35	
2	5	120	100	200	45	45	5	35	SiO ₂ etched away Total etch = 1000 to 1100 nm PR etch = 1.6 μm Feature height (after etch) = 1.8 μm
	6	120	100	200	45	45	5	35	
	7	120	100	200	45	45	5	35	
	8	120	100	200	45	45	5	35	

Table 4.9 Continued: Test 7									
Interesting thing is that the PR has not etched away completely. PR removed by cleaning the sample in acetone.									
3	9	120	0	200	50	48	2	0	Si etch = 2.8 to 3 μm PR etch = 2.5 Inconsistent readings Feature height (after etch) = 2.5 μm
	10	120	0	200	50	48	2	0	
	12	120	0	200	50	48	2	0	
4	13	120	0	200	50	48	2	0	Si etch = 4.6 to 5 μm PR etched away SiO ₂ etch = 700 nm Feature heights = 3 μm
	14	120	0	200	50	48	2	0	
	15	120	0	200	50	48	2	0	
	16	120	0	200	50	48	2	0	

Conclusions and observations:

- With the first set of etch parameters, SiO₂ was etched at a rate of 550 nm in 8 minutes. Figure 4.30 shows the filmetrics measurement of the thermal oxide thickness after 8 minutes of etching. The accuracy of the measurement is found to be 94.979%.
- After 8 minutes, the PR was etched for 900 nm, which is a very consistent and repetitive measurement.
- After 16 minutes, SiO₂ etches away completely and PR etches up to 1.6 μm .
- After 24 minutes, Si etches after SiO₂ for about 1.8 microns in 8 minutes which is very high etch rate. Hence, the test needs to be repeated to confirm the readings.

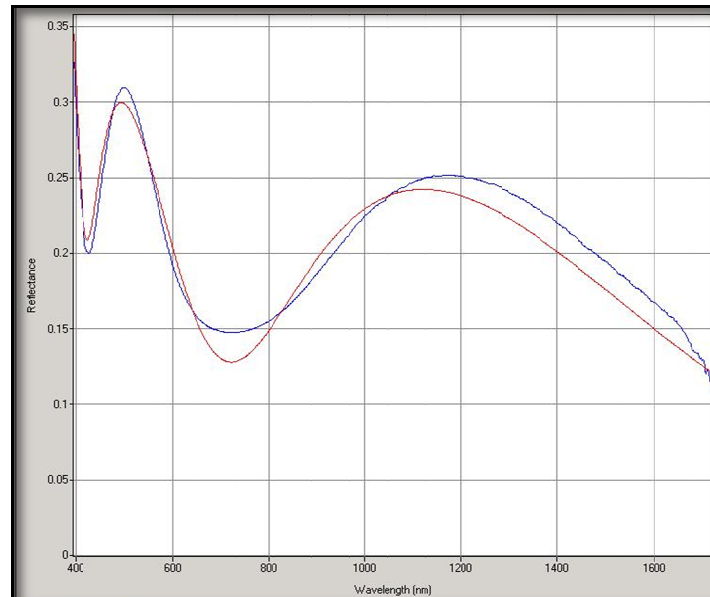


Figure 4.30: Oxide Thickness measured after 8 minutes of etching, using Filmetrics. The thickness measurement was 416 nm with a goodness of fit of 0.94979 which means that the oxide layer has etched $975 - 416 = 560$ nm. Hence the measurement is very accurate.

- PR etch is about $2.6\mu\text{m}$ which is higher than the original PR thickness. Hence, the presence of PR was checked by cleaning the wafer using acetone. PR was able to remove, which shows the presence of PR.
- After 32 minutes, the total etch is about 4.6 to $5\mu\text{m}$. which shows a Si etch of about $1.8\mu\text{m}$ in 8 minutes.
- Test to be repeated with same parameters.

Test 8:

Sample: Silicon wafer with 1 micron thick thermal oxide layer, patterned with SC 1827 PR.

Aim: Use a *glass slide* to cover up a region of the sample, continue with the same previous etch chemistries to repeat the same test. Aim is to achieve a silicon etch of 4.5 to 5 μm .

Etching duration: 32 minutes

Etch intervals: 120 seconds

Instructions: Take readings after every 8 minutes. Keep etching for 32 minutes in total.

Cool the sample for 5 minutes after each etch interval of 120 seconds.

Initial observation: PR thickness = 2.5 μm at the features.

Table 4.10: Test 8

Sr #	Etch parameters	Units	Units
		(Set 1)	(Set 2)
1	ICP (W)	100	0
2	RIE (W)	200	200
3	Pressure (mTorr)	45	50
4	CF ₄	45	48
5	O ₂	5	2
6	CHF ₃	35	0

Conclusions and Observations:

- After the first 8 minutes, SiO₂ etch = 520-530 nm; PR etch = 850-900 nm. These values are extremely consistent with the results in the previous test. The values obtained while measuring the feature heights after etching was 2.6 μm which was a bit inconsistent. By mathematical calculation, as shown in the Figure 4.31 below, the feature height should be about 2.3 μm.

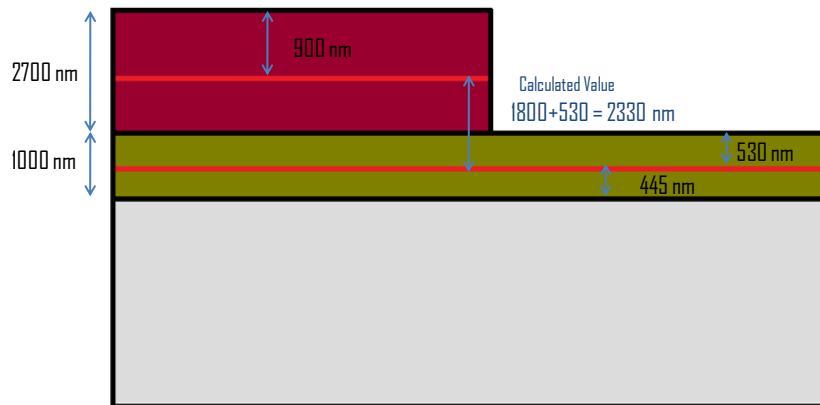


Figure 4.31: Schematic showing the etching of PR as well as SiO₂ taking place after 8 minutes. This is a mathematical explanation of what might be happening. The feature height theoretically should be 2.3 μm instead of the measurement value of 2.6 μm.

- After 12 minutes, SiO₂ etch = 800 nm; PR etch = 1100-1200 nm. Feature heights = 2.4 μm. Similarly, the feature height from calculation is 2.3 μm, which looks consistent.
- After 16 minutes, SiO₂ completely etched away; PR etch = 1.7 μm; feature heights 2.1 to 2.2 μm. From calculation, the feature height is 2 μm.

- After 24 minutes, Si etch begins. Total etch = 3 μm ; hence Si etch = 2 μm ; PR etch = 3.1 μm which means PR completely etched away and SiO₂ etch has begun; measured feature heights = 2.7 μm ; calculated feature heights = 2.6 μm . Hence very good consistency of the measured and calculated values.
- An EDAX analysis was performed to check whether SiO₂ was remaining beneath the PR. See Appendix VI which shows the presence of both silicon and oxygen confirming the presence of SiO₂.
- After 28 minutes, total silicon etch = 3.8 μm ; which means in 28-16 = 12 minutes, Si etch = 2.8 μm .
- After 32 minutes, Total Si etch = 4.7 μm ; PR has already etched away, and now even the SiO₂ layer is etched. Hence no more etching can take place.
- Result: Stop etching after 30 minutes.

Figure 4.32 below shows the SEM image of the etched feature. The sidewalls visible are very rough. This is due to the effect of plasma which makes the nature of etching very rough. Hence after a certain amount of plasma etching the filmetrics, which work on reflectance theory and depend on the surface to be very smooth, will not give accurate readings.

Figure 4.33 (a) shows the SEM image of the force sensor beam at a scale of 50 μm and figure 4.33 (b) shows a close up image of the force sensor beam. The force

sensor beam being the smallest feature is attacked the most. The image shows broken features, which is due to poor developing during the lithography.

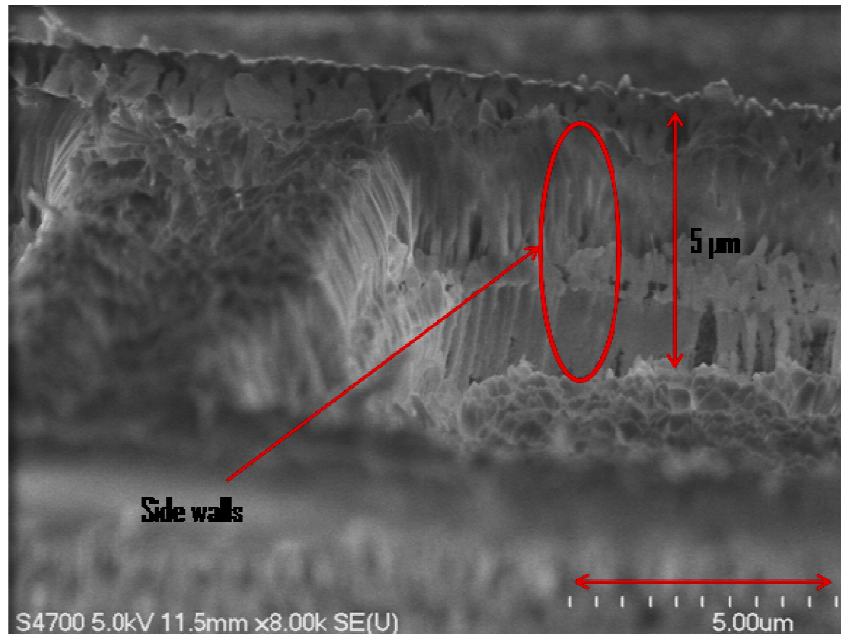


Figure 4.32: SEM image of the 32 minute RIE etch. Sidewalls of the features are visible very clearly. The total depth that could be reached with RIE etch was 5 microns. The surface as visible in the image is extremely rough.

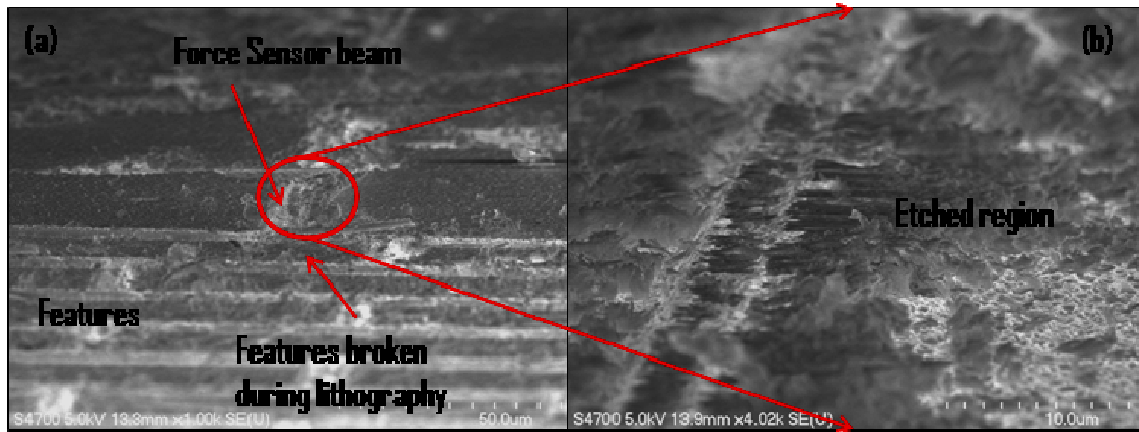


Figure 4.33: (a) SEM image force sensor beam along with the support features. There are regions where the features are broken due to poor lithography. (b) shows the close in view of the force-sensor

Figure 4.34 shows the nature of the RIE etch, while etching the photo-resist and the substrate.

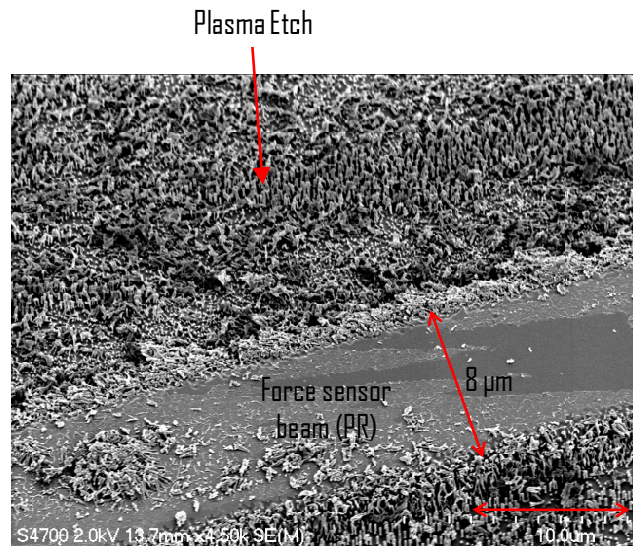


Figure 4.34: SEM image of the force sensor beam and the nearby regions after plasma etch. The feature is covered with PR and the image shows the rough nature of the RIE etch on the substrate and the RIE etch on the PR is not as rough

Chapter 4- Bio-MEMS Force Sensor Fabrication

While taking the SEM images, we stick the wafer using a carbon tape on to the sample holder. While the RIE etched sample was stuck to the sample holder, after imaging while removing the sample from the holder, the sample fractured into pieces. The fracture seemed like a brittle fracture. Initially the conclusion was the probability of handling and human errors. Then the second sample which went through a 30 minute RIE process failed while stress was applied while removing it from the SEM sample holder.

Figure 4.35 shows the failed sample and the fracture regions. From this incident, it was concluded that the RIE etch was increasing the brittleness of the substrate. Hence, RIE causes the silicon substrate to become brittle and the possibility of fracture increases.

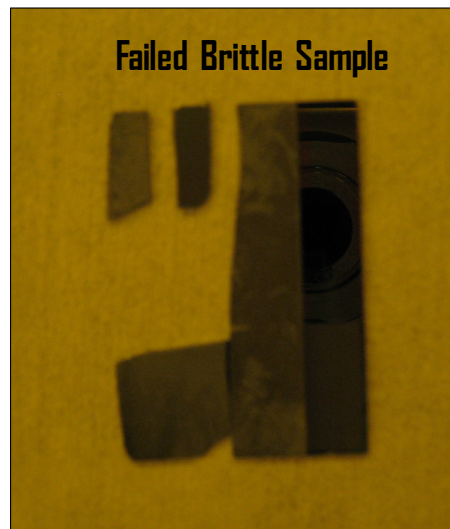


Figure 4.35: Picture of a failed sample while taking it out of the sample holder. This shows the increase of brittleness in the substrate after RIE.

The complete set of etch rates of the 3 different materials in SiO₂, Si and PR are shown. These etch rates show the depth of etching achieved per minute inside the RIE chamber.

SiO₂ Etch Rate	=	550 nm in 8 minutes = 70 nm per minute
	=	1000 nm in 16 minutes = 62 nm per minute
Average etch rate	=	66 nm per minute
Si Etch Rate	=	2000 nm in 8 minutes = 250 nm per minute
	=	2800 nm in 12 minutes = 233 nm per minute
	=	3700 nm in 16 minutes = 232 nm per minute
Average Si etch rate	=	239 nm per minute
PR Etch Rate	=	875 nm in 8 minutes = 110 nm per minute
	=	1200 nm in 12 minutes = 100 nm per minute
	=	1700 nm in 16 minutes = 106 nm per minute
Average PR Etch rate	=	105 nm per minute

4.3.2. *Anisotropic Etching:*

There are multiple reasons for not continuing the use of RIE. Firstly, the roughness of the surface caused by RIE is unacceptable for the device. There is a compromise on the accuracy of the measurements taken due to the roughness of the surface. Secondly, further RIE etching is not possible as the SiO_2 mask is being etched away which exposes the Si substrate. Hence, there is a need to use a different method to etch deeper and the sidewalls being smoother.

For this reason, anisotropic etching was employed for etching the Si substrate. Theoretically it is a known fact that KOH wet etching, has a good directionality and a very good selectivity between silicon and silicon di-oxide. There are common wet chemical etchants such as potassium hydroxide (KOH), ethylene diamine pyrocatechol (EDP), tetramethyl ammonium hydroxide (TMAH), hydrazine etc. As discussed in chapter 1, all of these chemicals etch silicon substrate much faster than silicon dioxide and silicon nitride. But as they follow a good directionality, for (100) wafers, they form sidewalls at an angle of 54.7° . Anisotropic etchants show an etch selectivity between the (100) and (111) planes. Anisotropic etchants etch the (100) planes of the Si substrate much faster than the (111) planes. The angle between the (111) and (100) planes is 54.7° . Now, let us venture over the experimental process for the KOH wet etching.

Experimental Procedure:

Initial notes: Photo-resist cannot be used as an etch mask. SiO_2 will etch but at a very slow rate compared to Si. Silicon nitride is the best mask for this process, as it will not etch under the influence of KOH.

Material Requirements:

- Equipment: one glass beaker, and two polypropylene beakers, stainless steel tweezers, PTFE wafer holder, and hot plate.
- Chemicals: Potassium hydroxide (KOH) can be purchased from the chem. store in the form of pellets, and De-ionized water.
- Conduct the procedure under a ventilated fume hood.
- Personal protective equipment: trionic gloves on top of nitrile gloves, goggles, acid sleeves. Never work with KOH etching processing without the above listed PPE.

Procedure:

- Get a water rinse beaker depending on the size of the sample.
- Get another beaker for processing. This beaker must be a Pyrex glass container for the KOH solution.
- Set the hot plate to a temperature at 72°C .
- Pour approximately 100 ml of de-ionized water in a 250 ml glass container. The size of the container can depend on the size of the sample.

Chapter 4- Bio-MEMS Force Sensor Fabrication

- Add approximately 100 mg of KOH pellets (about 50 pellets) into the DI water solution.
- Place this glass container on the hot plate and wait for about 5 minutes until the solution reaches the 72 °C temperature.
- Place the sample in the solution using the tweezers. Avoid dropping the sample into the solution and cause a splash. Place the sample slowly.
- During etching considerable amount of bubbles will emerge as the KOH solution etches silicon.
- Different ratios of KOH pellets to DI water will result in different etch rates.
- After etching, rinse the sample in DI water for about 5 minutes.
- Transfer the sample to another DI water beaker for a second rinse.
- After the second rinse, blow dry the sample using the nitrogen gun.

This is the experimental process which was followed to carry out the etching process. A new silicon wafer with one micron thick thermal oxide layer was patterned and diced into 7 samples. One of these samples is taken. Now, as SiO₂ is a mask, we etch the one micron oxide layer with RIE. As we have characterized RIE etch rates for etching SiO₂ we can use the same chemistries.

Test 1:

Etch the sample for 16 minutes using the accepted RIE parameters discussed above. After the SiO₂ layer is etched away, the PR layer is still remaining as the PR thickness is 2.7 μm and the PR etching taken place is only 1.7 μm . Now take this sample to the KOH etching.

KOH pellets / DI water ratio = 100 mg / 100 ml (about 50 pellets in 100 ml water)

Temperature of hot plate = 72⁰C

Total time of etching = 29 minutes

Etching intervals = after every 10 minutes, take the sample to the microscope and try to locate the side walls.

Results and Observation:

- During etching, the photo-resist peels off and it is visible.
- SiO₂ layer does not get etched at all, which proves SiO₂ is a good mask. Figure 4.36 shows the filmetrics measurement which was taken after the 29 minute of etching in the KOH solution.

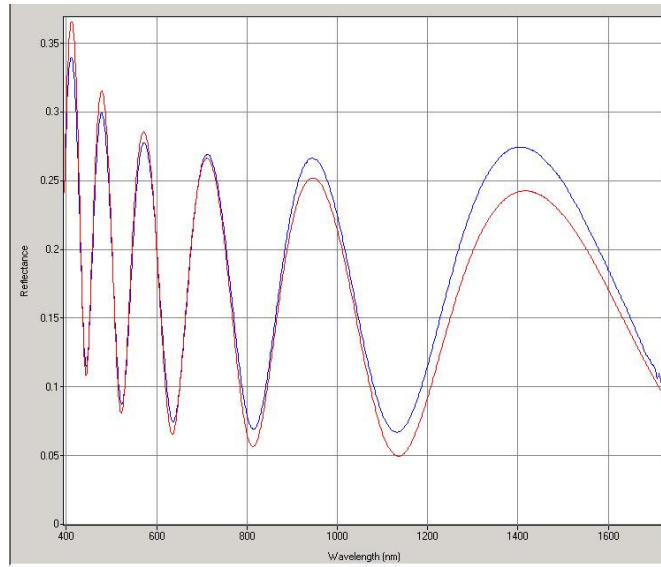


Figure 4.36: The thickness of the thermal oxide layer before the KOH etch was 975 nm as shown in figure 3.15. After the etching process the measurement is the same. The accuracy of the reading is 96.25%, which is very accurate.

- This etch process resulted in a 24 μm outer side wall depth and 11 μm sidewall depth inside the features.
- The 54.7° (111) planes are clearly visible as shown in the SEM image shown below.
- Figure 4.37 shows the SEM image clearly showing the anisotropic etch and the sidewalls.
- The SiO_2 layer on the top of the features is still very rough as shown in Figure 4.37.
- This means that the SiO_2 has not etched and it maintains the same etch surface, which it forms after the RIE.
- Figure 4.37 (d) shows clearly the rough nature of the SiO_2 layer on the features.

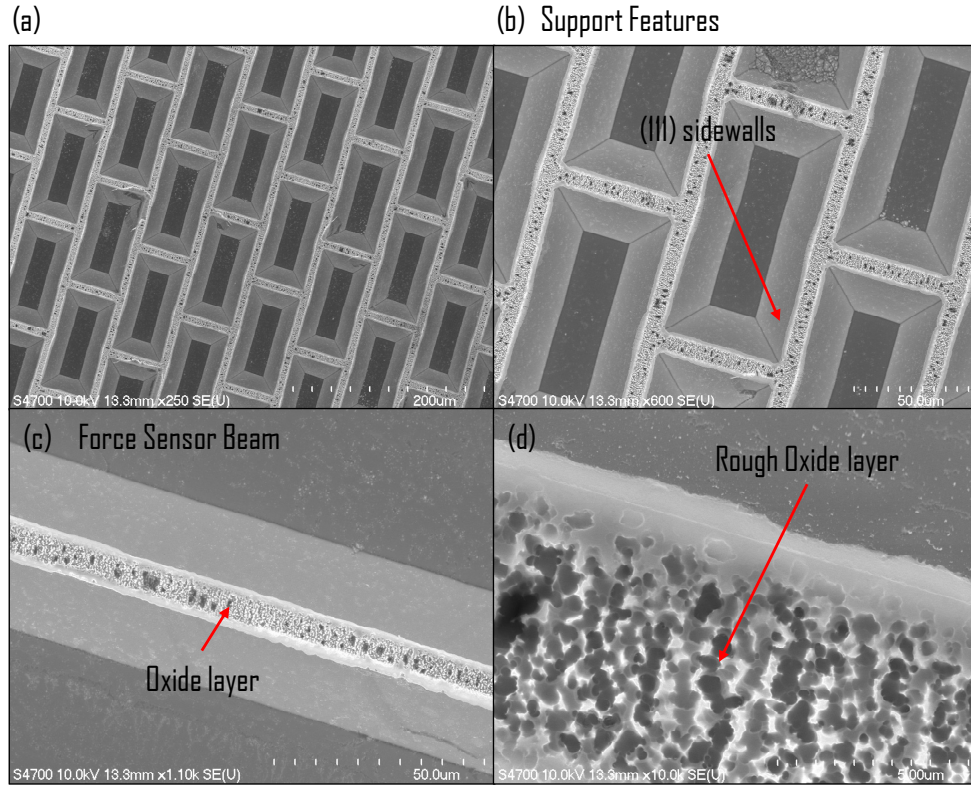


Figure 4.37: (a) SEM image of the Si substrate being etched by KOH. The (111) planes are clearly visible. (b) shows a closer image of the features and the sidewalls. (c) shows the force sensor beam with its etching profile. (d) The oxide layer shown at the top of the feature is a very rough surface after the RIE. This shows SiO_2 has not etched.

The figure 4.38 below shows the SEM image which was taken with the sample being vertically placed. This image shows the exact depth of the etch, i.e. the height of the sidewalls.

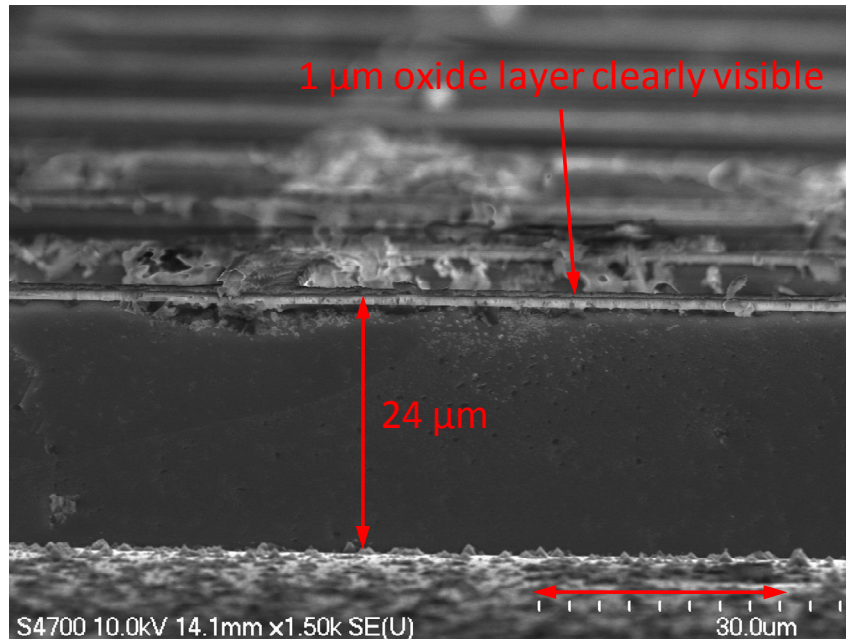


Figure 4.38: SEM image of the feature side walls, showing a depth of 24 microns of sidewalls. The image also clearly shows the one micron thick oxide layer on the top of the feature.

As we discussed in the Chapter 2, when the mask supporting the pattern on the substrate contains exposed corners, after a while of anisotropic etching, the etchant starts to etch the (111) planes also and there occurs undercutting beneath the mask. For example, the cantilever of the probe in our design is an exposed convex corner. The convex corners get attacked much faster than the concave corners when the sample is kept for a longer time in the KOH solution. The same phenomenon is observed during this etching. Figure 4.39 shows the SEM image of the probe of the device, which is a perfect example of an exposed corner. In this case the undercutting has begun and the (111) planes are being attacked.

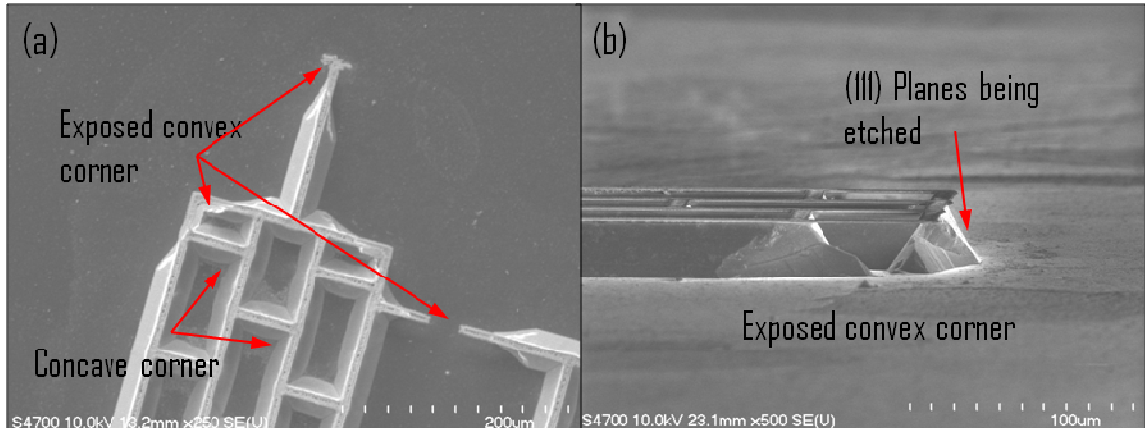


Figure 4.39: SEM image of the probe end of the device. The exposed convex corners are clearly being etched. (a) Top view of the device showing the exposed corners in the device, and the etching. (b) Side view showing the etching of the (111) planes

Figure 4.40 shows the SEM image of the device, explaining the weakening of the silicon dioxide mask at the exposed corners near the probe. This is accelerating the undercutting below the mask.

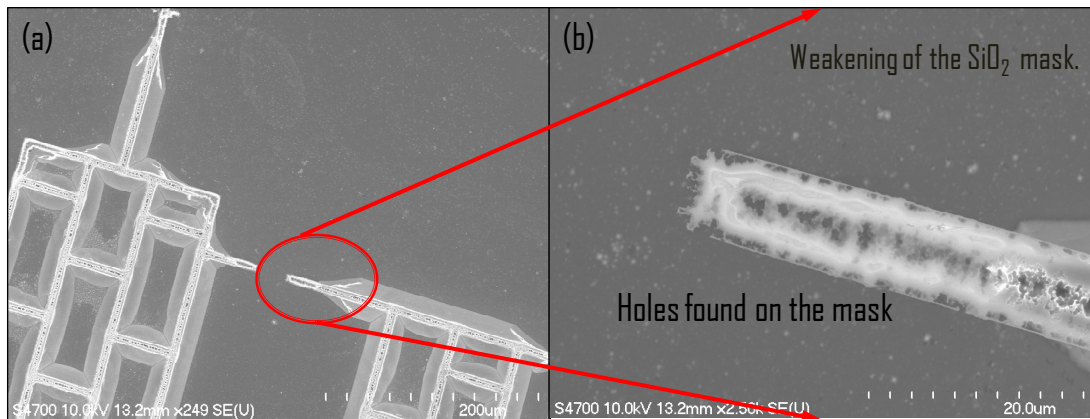


Figure 4.40 SEM image showing the weakening of the oxide mask. There are some holes found on the mask surface, which seems to expose the silicon substrate beneath. This region is the exposed convex corner near the probe region of the device.

Figure 4.41 shows the SEM image of the complete device on a tilted sample holder. This image shows how the device would look on the silicon substrate.

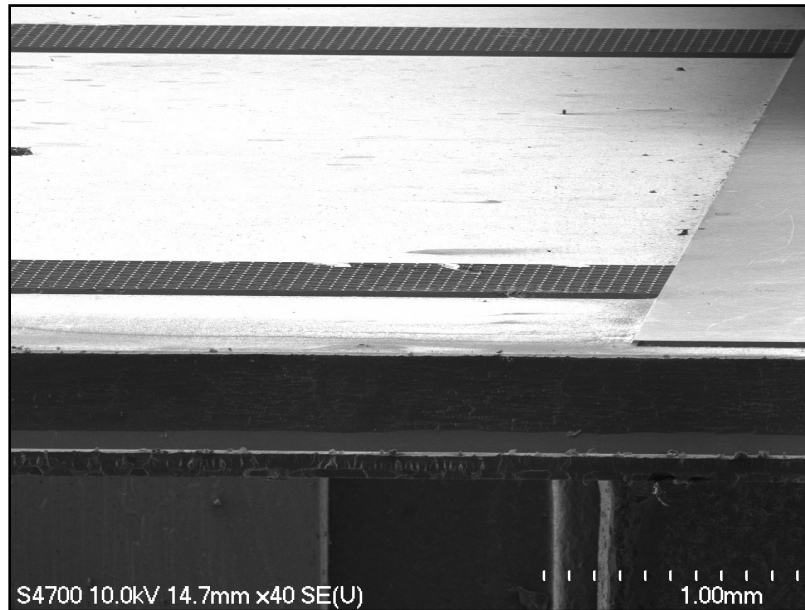


Figure 4.41 SEM image showing the device in the minimum

There were multiple tests done with other samples to characterize the etching process, and the results found were exactly similar with the KOH pellets to DI water ratio at 100 mg to 100 ml. In this case, the etching was performed for 25 minutes to achieve an etch depth of 24 microns. Hence, the etch rate is calculated to be about **960 nm per minute**. Theoretically this value seems correct as previous characterizations show the etch rates to be within the range of 700 nm to 4000 nm per minute. Hence, better etch rates could be achieved with some more characterization of this etching process. By making the solution more concentrated with KOH will result in better etch rate. In all, six

samples were used and prepared with the anisotropic wet etching for the next step in the micro-fabrication process. All six samples presented similar results with the etch concentration and the etch rates. The next step in the fabrication process is the creation of another mask layer over the etch to mask to sidewalls. Hence, thermal oxidation was performed to grow this mask.

4.4. Dry Thermal Oxidation:

The next step in the fabrication process was a requirement of masking the sidewalls with silicon dioxide. As discussed before, this masking step is for protecting the sidewalls from the isotropic etch step which follows the oxidation step. For this thermal oxidation step, five samples were selected which were etched with KOH for 24 microns. To measure the oxide thickness accurately, there were two clean coupon samples placed on the wafer boat. The specific wafer arrangement was planned. First, a blank coupon sample was placed on the wafer boat, then subsequently the five samples were placed on the wafer boat and finally the second blank coupon sample was placed. A blank silicon wafer is patterned with SC 1827 PR and the PR is developed. This wafer is diced into seven pieces to form the samples. Two samples are taken and the PR is removed by cleaning the sample with acetone and iso-propanol. Now these blank samples act as the coupon samples for the thermal oxidation step. Figure 4.42 shows the experimental setup of the oxidation furnace.

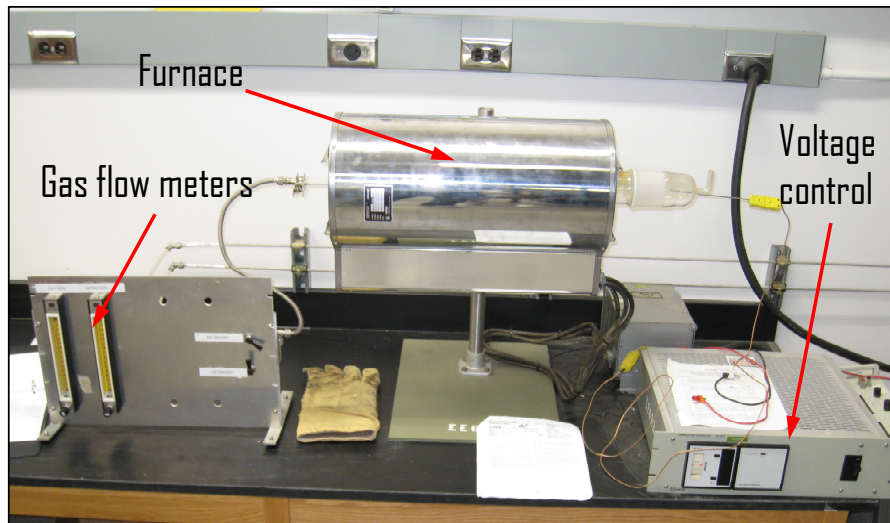


Figure 4.42 Laboratory experimental setup of the thermal oxidation furnace which was used to grow a thermal oxide of 300 nm.

The temperature of the furnace was raised to 550°C . Then the set of samples were placed in a wafer boat and inserted into the oxidation furnace. With the help of the gas flow meters, only nitrogen was allowed to flow into the furnace keeping the environment inside the furnace very clean. The temperature inside the chamber was controlled by controlling the voltage applied to the coils outside the chamber of the furnace. It took about one hour for the temperature to reach 1100°C , and when the temperature reached 1100°C , oxygen gas was turned on. The timer was set to 3 hours. Theoretically and from previous characterizations, the oxide thickness at 1100°C for 3 hours came to be about 300 nm. After 3 hours of oxidation, the oxygen gas was turned off and the nitrogen was turned on. The voltage supply was turned off. The samples were kept inside the chamber overnight for cooling purposes. The next day the samples were taken out the oxide thickness was measured using filmetrics. Figure 4.43 shows the filmetrics measurement

of the first and the last coupon. The samples were relative quiet rough for the filmetrics to present accurate measurements. In the first coupon which was closer to the oxygen flow, the oxide thickness was found to be 287 nm, and in the second coupon which was farther away from the oxygen flow, the oxide thickness was found to be 230 nm.

The measurements obtained from the filmetrics on the coupons are 99.98% accurate. Hence, the samples placed between the coupons would have an oxide thickness varying between 230 nm and 287 nm. Now we have five samples which could be used for the next and the final step of micro fabrication. This step is the isotropic etching process to release all the cantilevers like the probe.

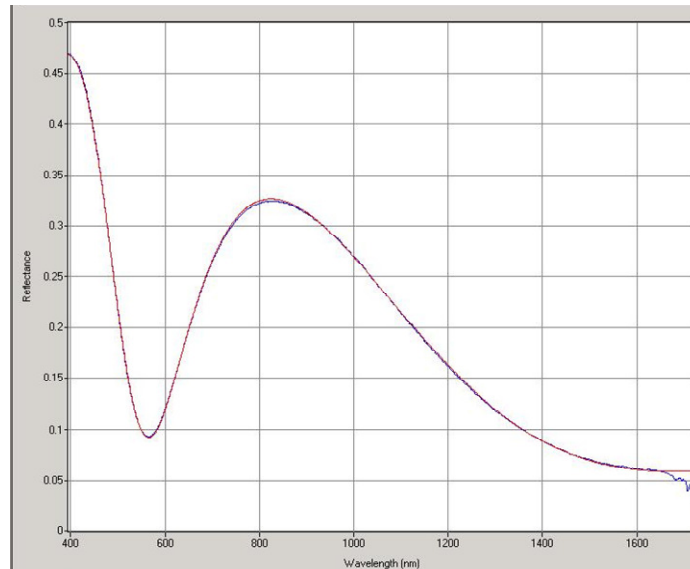


Figure 4.43: Oxide thickness of the coupon 1 and coupon 2 are shown. The coupon 1 shows 287 nm thick and coupon 2 shows 230 nm thick oxide layer. The accuracy of both these measurements is 99.98 % which is extremely accurate. The oxide thicknesses on the samples would be between 230 nm and 287 nm.

4.5. *Isotropic Etching:*

The next and the final step in the fabrication process of this MEMS force sensor is the isotropic etching. This process is known as the SCREAM process (Single-Crystal Reactive Etched and Metallization). In this method the oxide mask present on the side walls prevents the isotropic etchants from etching away the sidewalls. Now as we also have SiO_2 on the bottom of all the pits and the silicon substrate, it needs to be removed. To remove the oxide from the bottom, we perform RIE on the sample for 4 minutes to etch away the 250 nm thick oxide layer. The RIE parameters for etching the oxide are the same as we characterized previously for etching SiO_2 . Figure 4.44 shows the SEM image of the sample after the 4 minute RIE. This also shows its effects on the sidewalls. The surface of the sidewalls as well as the bottom of the pit of features becomes rough.

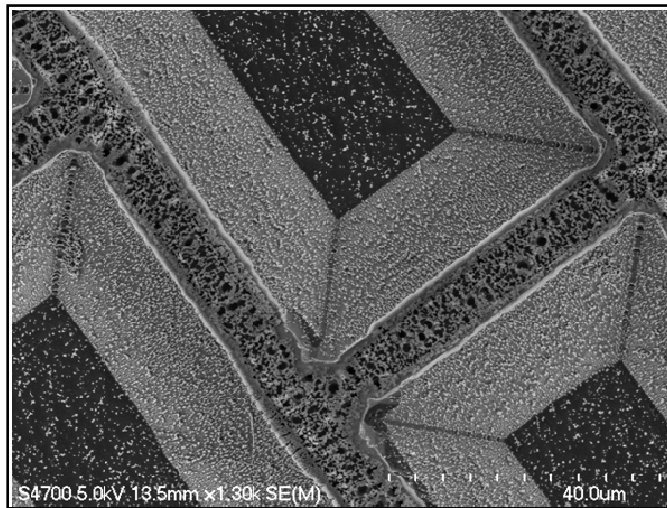


Figure 4.44: SEM image of the sample after performing RIE for 4 minutes to remove the Oxide layer from the bottom surfaces. The sidewalls are also being etched as the surface is becoming rough due to the plasma

After this etch, once the Si substrate is exposed the sample is taken to perform the isotropic etch. The experimental procedure for the isotropic etch is given below:

Material Requirements:

- Equipment: 3 polyethylene beakers, PTFE tweezers or stainless steel tweezers, PTFE handling tools.
- Chemicals:
 - Hydrofluoric acid (HF-49%): HF is extremely health hazardous. HF also attacks glass, hence glass beakers cannot be used for this purpose.
 - Nitric acid (HNO_3 -70%): it is compatible with glass, it causes acute burns to skin and eye irritation.
 - Glacial Acetic acid (CH_3COOH -98%)
- Engineering controls: conduct the whole procedure in a ventilated fume hood or an acid bench with neutralization station.
- Personal protective equipment: nitrile gloves on top of neoprene gloves, goggles, acid sleeves. Never work with HF etching processing without the above listed PPE.

Procedure:

- This etch process is also called HNA etching.
- Get 3 polyethylene beakers for the processing. One for processing and the other two for rinsing. While using the acid bench, you can use the same polyethylene beaker for rinsing as well as the neutralization station rinses the solution.

Chapter 4- Bio-MEMS Force Sensor Fabrication

- Use graduated cylinders to measure the chemicals. Theoretically, or from previous characterizations, a ratio of HF: HNO₃: acetic acid of 1:3:8 etches silicon with a good selectivity with SiO₂.
- Hence, the following ratio of the chemicals was used.
 - 20 ml of HF 49%
 - 60 ml of Nitric acid 70%
 - 160 ml of glacial acetic acid
- Add the acetic acid first, then nitric acid and then HF at the end.
- Fill the other two containers with de-ionized water.
- Transfer the sample into the HNA mixture carefully with PTFE tweezers.
- Etch the sample for the required length of time depending on the characterization.
- The next step after the etch is to rinse the sample.
- Rinse the sample for 5 minutes in each of the containers with DI water.
- If using an acid bench, then turn on the rinse after the etch.
- Dry the samples with a nitrogen gun after the rinsing is complete and view in the microscope.

This is the procedure used for performing the isotropic etch. Here are some of the characterization results:

Test 1:

From previous characterization results, with a HNA ratio of 1:3:8, a reference etch rate of 3 μm per minute was obtained. Considering this as a reference, the etching was performed for 6 minutes.

Figure 4.45 shows the SEM images of the isotropic etch which just began. The undercutting has started taking place, which shows that those sidewalls seem to be protected. Figure 4.45 also shows the effects of the isotropic etch on the probe. There is a severe amount of undercutting on the probe; the mask is also etched away which is etching away the probe.

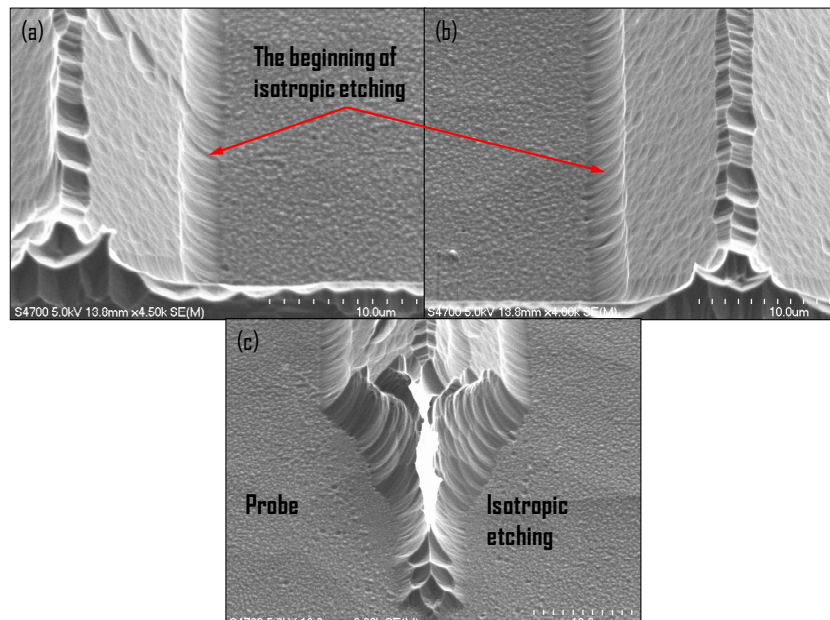


Figure 4.45: SEM image of the sample after the first attempt on isotropic etching. (a) and (b) show the beginning of isotropic etching. (c) shows the effect of isotropic etching on the probe regions, which are the exposed areas. The etchants are etching away the mask as well as the substrate.

Conclusions:

Characterization needs to be done for this isotropic etching. A total of about $30\text{ }\mu\text{m}$ has to be etched sideways with the HNA etch. SiO_2 does not seem a very good mask for the isotropic etching. Another attempt at isotropic etching is recommended with a longer duration of etching time.

Test2:

We used the same ratio of the HNA which is 1:3:8. The quantity of chemicals were

HF = 20 ml; Nitric Acid = 60 ml; and Glacial acetic acid = 160 ml

Etch timing = 8 minutes.

Figure 4.46 shows the SEM images of the isotropic etch. Undercutting is visible, but the sidewalls are getting etched at a high rate.

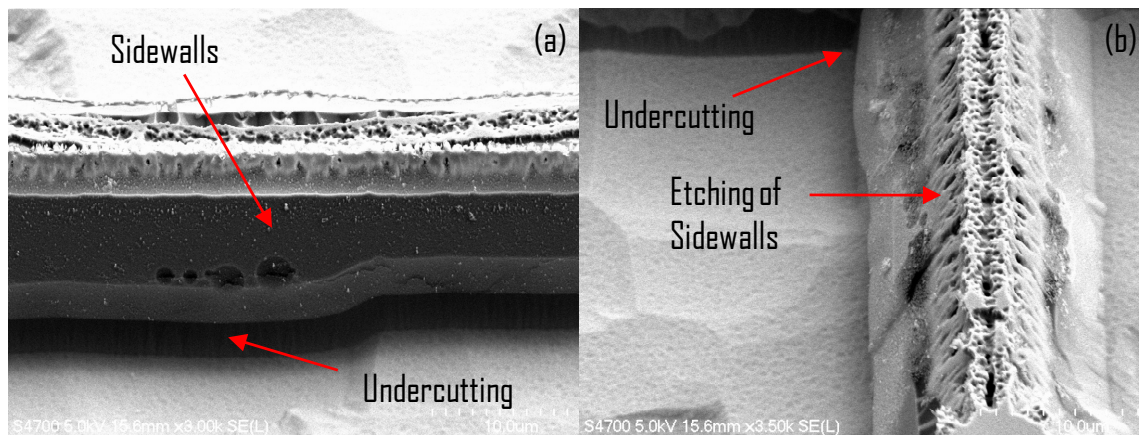


Figure 4.46: SEM image of the sample after the test 2 on isotropic etching. (a) Undercutting clearly visible. and (b) Etching of sidewalls has begun. The (111) planes are also getting etched. The SiO_2 mask is not holding up to the etchant.

Conclusion

The Isotropic etchant has started undercutting into the features to release them. But during this process, the sidewalls are also being attacked which in turn is etching them away. The SiO_2 mask on the features is not sufficiently strong.

Test 3:

We used the same ratio of the HNA which is 1:3:8. The quantity of chemicals were

HF = 20 ml; Nitric Acid = 60 ml; and Glacial acetic acid = 160 ml

Etch timing = 15 minutes.

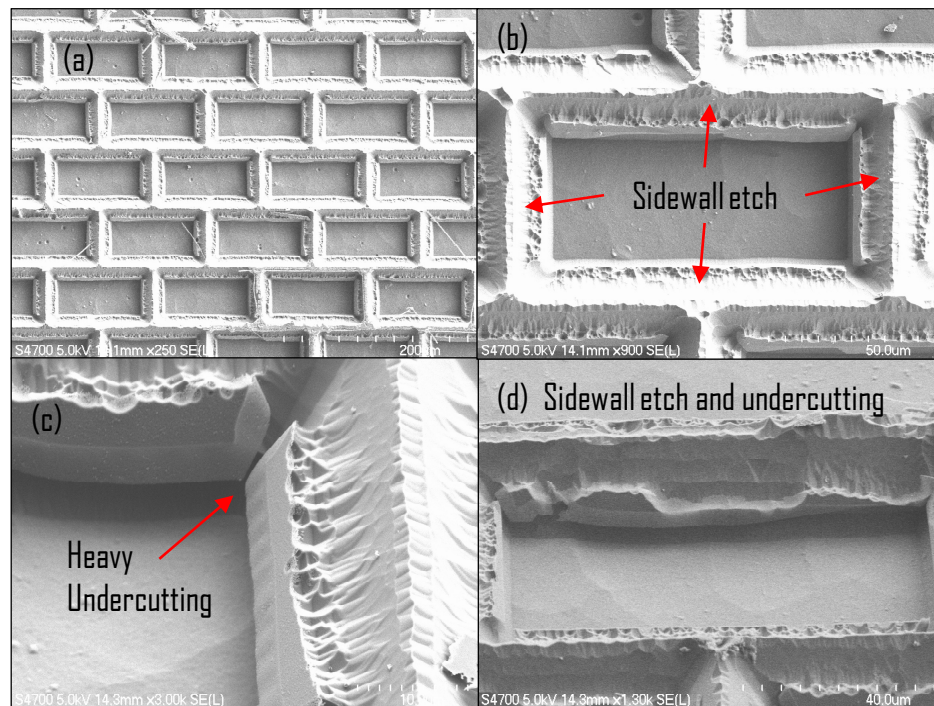


Figure 4.47: SEM image of the sample after the test 3 in isotropic etching. (a) Features with undercutting. (b) Etching of sidewalls clearly visible; (c) Heavy undercutting visible, but the sidewalls are attacked (d) Another image of the features after 15 minutes of isotropic etching.

Figure 4.47 shows the SEM images of the isotropic etch. Undercutting is visible, but the sidewalls are getting etched at a high rate. The sidewall etching has increased from the previous test. After 15 minutes of etching in HNA solution, the sidewalls are heavily attacked and the amount of undercutting has also risen. Try changing the etch ratios and check for the result.

Test 4:

Performing the same HNA etch with a different HNA ratio, for 18 minutes.

HF = 40 ml; Nitric Acid = 70 ml; and Glacial acetic acid = 110 ml

Result: The sample becomes shiny and looks like a polymer layer deposition over the whole area of the sample. When taken under the SEM, there is no contrast found as the SiO_2 seems to have etched.

Alternative methods for Isotropic Etching:

We can use different etching chemistries to perform isotropic etching. (Muller et al, 1996) (Williams et al, 2003). We can also use micromachining processes to cutting the device out of the Si substrate. Micro-mill with 6 axis aligner present in the ME-EM department which can be used to cut the sample out of the substrate. Characterization is required. Now, we will be discussing the essential work which needs to be done to further this process of completing the fabrication of this MEMS based bio-force sensor.

Chapter 5

Conclusions and Recommendations for Future Work

5.1. Conclusion

The goal of this project was to develop and fabricate a simple MEMS based biological force sensor to measure the force response of a living cell. This device has already been fabricated and put to test previously at University of Illinois at Urbana-Champaign. During the fabrication processes, we faced several challenges, since the fabrication of such devices has never been studied before here at Michigan Technological University. The fabrication of this force sensor was to be performed with the help of the laboratory facilities of Michigan Technological University. The main challenge before us while fabricating this device was to etch 20 microns deep features and the recipe suggested by UIUC is based on the deep reactive ion etching (DRIE). We do not possess the DRIE facility here at Michigan Technological University. In all, there were seven steps of micro-fabrication techniques involved in this project. Two different methods were used to perform the oxidation of the (100) Si wafer. Initially, one micron thick silicon dioxide layer was deposited on to the silicon wafer using the sputtering tool. The thickness of the deposited silicon dioxide was not very uniform throughout the silicon wafer. Since, the thermal oxidation is a very slow process ten (100) silicon wafers with one micron thick wet thermal oxide were purchased from Silicon Quest International for the experiments.

The next step in the micro-fabrication process was photo-lithography. A CAD file of the mask layout was prepared. Using this CAD file, a clear field photo-mask was purchased from Bandwidth Foundry Inc. in Australia. The most important factor in the photo-lithography process is the photo-resist. For our process, since our mask is a clear field mask, a positive photo-resist should be used. Four different photo-resists were selected for experimentation: SC 1827 (Shipley Co.), P-Futurrex PR-2000 (Futurrex), AZ-P4620 (AZ Electronics) and SU-8. One of these four photo-resists were selected and the selection criteria was; positive polarity, higher thickness and good resolution. Experiments were performed and SC 1827 was selected.

The next step in the micro-fabrication process was Etching. Initially deep reactive ion etching process was preferred. But due to the unavailability of this facility, reactive ion etching was employed. The requirement of the etch depth was about 20 microns. Multiple experiments were performed on the TRION etching tool, and a maximum of 4.8 micron depth was attained. Etching rate of SiO_2 was characterized. Hence, the focus was shifted from RIE to anisotropic etching where KOH solution was used to etch the silicon substrate. The (111) planes were exposed and an etch depth of 24 microns was obtained. This etching process was characterized and samples were prepared. Another masking layer of SiO_2 was required to mask the sidewalls of the features. Dry thermal oxidation was employed to grow 300 nm thick SiO_2 layer.

After exposing the silicon substrate by using RIE to etch away the SiO_2 from the base, isotropic etching was employed to undercut and release the features. Experiments were performed and the undercutting was found to be happening through the SEM images. But further characterization is required to completely release all the features and use the device as a force sensor.

5.2. *Results Summary*

The following results were obtained during the characterization of each micro-fabrication step performed to fabricate the force sensor:

- During deposition of SiO_2 , the deposition rate was 1045 nm in 180 minutes, which is 5.80 nm per minute.
- The photo-resist SC-1827 was selected for photo-lithography. The thickness of the photo-resist was between 2.8 to 3.0 μm . The resolution of this photo-resist was very good.
- The RIE etch rate for:
 - SiO_2 was 66 nm per minute
 - Si was 239 nm per minute
- The KOH etch rate for silicon was found to be 0.96 μm per minute.
- Isotropic etching was performed with the following chemicals: hydrofluoric acid (HF), Nitric acid (HNO_3), and Glacial Acetic Acid

(CH₃COOH). The ratio of mixture was 1:3:8 in the same order as given above.

Additional work is required for the characterization of the isotropic etching and release of the force sensor from the silicon substrate.

5.3. *Recommendations for Future Work*

Though we are very close to fabricating this device, there is still some work that needs to be done to complete the fabrication. Here are some recommendations to make the fabrication process better and more efficient.

Theoretically, silicon nitride is a better mask compared to silicon dioxide. Hence, silicon nitride could be deposited and used as a mask. Silicon nitride has been proved to be a harder material to etch compared to silicon dioxide. One micron thick layer of silicon nitride should act as a better mask. The company standards for the resolution of the photo-resist AZ-P4620 is about 4 μm. The smallest feature size on our device is about 9.07 μm. Hence, we can try to characterize the AZ-P4620 for the photo-lithography process as it gives a thicker layer of photo-resist. During isotropic etching, different ratios of the acids HF, HNO₃, and acetic acid can be tried to characterize the etch rate and the undercutting.

For Future work, the laboratory for performing the experiments needs to be setup with the following equipments: Olympus IX81- Motorized System Inverted Microscope

with CCD camera installed, one nanometer resolution piezo stage, one micrometer resolution mechanical stage, sample holder, culture dish, and culture medium with the monkey kidney fibroblast cells. Figure 5.1 shows the picture of the experimental setup that is required.

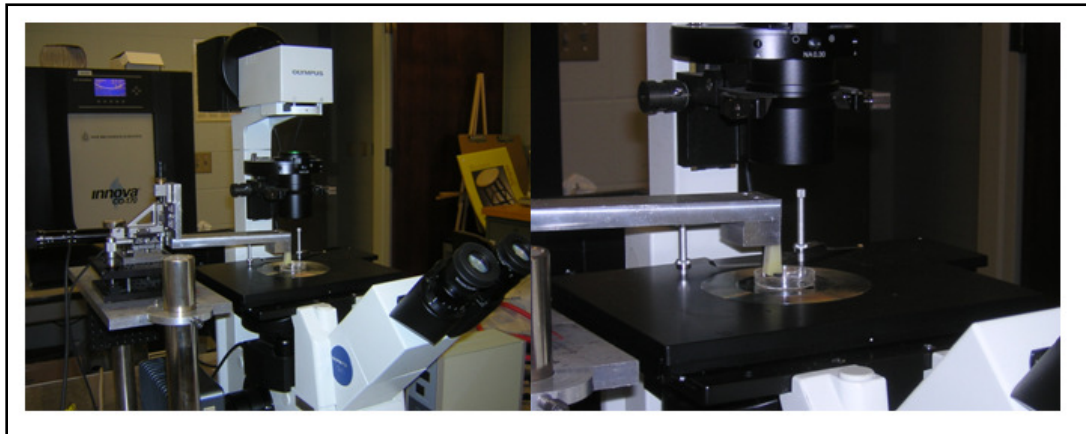


Figure 5.1: Picture showing the experimental which is required.

Bibliography

- [1]. N. Wang, J.P. Butler, and D.E. Ingber . (1993). Mechanotransduction across the cell surface and through the cytoskeleton. *Science* , 1124-1127.
- [2]. A. Corigliano, B. De Masi, A. Frangi, C. Comi, A. Villa, M. Marchi. (2004). Mechanical characterization of polysilicon through on-chip tensile tests. *Journal of microelectro mechanical systems* , 200-219.
- [3]. A. J. Baner, J. Gilbert, D. Taylor and O. Monbureau. (1985). A new vacuum-operated stress-providing instrument that applies static or variable duration cyclic tension or compression to cells in vitro. *Journal of Cell Science* , 35–42.
- [4]. A. R. Bausch, F. Ziemann, A. A. Boulbitch, K. Jacobson, E. Sackmann. (1998). Local Measurements of Viscoelastic Parameters of Adherent Cell Surfaces by Magnetic Bead Microrheometry. *Biophysical Journal* , 2038-2049.
- [5]. A. Yamamoto, S. Mishima, N. Maruyama, and M. Sumita. (1998). A new technique for direct measurement of the shear force necessary to detach a cell from a material . *Biomaterials* , 871-879.
- [6]. B. Nardelli, B.I.Yakobson, J.Bernholc. (1998). Mechanism of strain release in carbon nanotubes. *Physical Review B* , R4277–R4280.

Bibliography

- [7]. B.A.Samuel, A.V.Desai, M.A.Haque. (2006). Design and Modeling of a MEMS pico Newton loading/sensing device. *Sensors and Actuators* , 155-162.
- [8]. B.G.Demczyk, et al. (2002). Direct mechanical measurement of the tensile strength and elastic modulus of multiwalled carbon nanotubes. *Materials Science and Engineering* , 173-178.
- [9]. B.I.Yakobson, M.P.Campbell, C.J.Brabec, J.Bernholc. (1997). High strain rate fracture and C-chain unraveling in carbon nano-tubes. *Computational Materials Science* , 341-348.
- [10]. C. Haber, D. Wirtz. (2000). Magnetic tweezers for DNA micromanipulation. *Review of Scientific Instruments* , 4561.
- [11]. D.B Serrell, T.L Oreskovic, A.J Slifka, R.L Mahajan, D.S Finch. (2007). A uniaxial bioMEMS device for quantitative force displacement measurements. *Biomed Microdevices* , 267-275.
- [12]. E. Evans, D. Berk, and A. Leung. (1991). Detachment of agglutinin-bonded red blood cells. II. Mechanical energies to separate large contact areas. *Biophysical Journal* , 849–860.
- [13]. G.Bao, S.Suresh. (2003). Cell and molecular mechanics of biological materials. *Nature Materials* , 715-724.

- [14]. G.C.Easty, D.M.Easty, E.J.Ambrose. (1960). Studies of cellular adhesiveness. *Experimental Cell Research* , 539-548.
- [15]. Ghandhi, S. K. (1994). *VLSI Fabrication Principles - Silicon and Gallium Arsenide (2nd Edition)*. New York: Wiley Inter Science.
- [16]. Ghandhi, S. K. (1994). *VLSI Fabrication Principles - Silicon and Gallium Arsenide (2nd Edition)*. New York: Wiley Inter Science.
- [17]. H. Miyazaki, Y. Hasegawa, and K. Hayashi. (2000). A newly designed tensile tester for cells and its application to fibroblasts . *Journal of Biomechanics* , 97-104.
- [18]. H.Espinosa, Y.Zhu, N.Moldovan. (2007). Design and operation of MEMS-Based Material testing system for Nanomechanical Characterization. *Journal of Microelectro mechanical Systems* , 1219-1231.
- [19]. J. Guck, R. Ananthakrishnan, C. C. Cunningham, and J. Kas. (2002). Stretching biological cells with light. *Journal of Physics: Condensed Matter* , 4843-4856.
- [20]. J. W. Dai and M. P. Sheetz. (1995). Mechanical properties of neuronal growth cone membranes studied by tether formation with laser optical tweezers . *Biophysical Journal* , 988-996.

Bibliography

- [21]. J.Cummings, A.Zettl. (2000). Low-Friction Nanoscale Linear Bearing Realized from Multiwall Carbon Nanotubes. *Science* , 602-604.
- [22]. J.Cummings, A.Zettl, P.G.Collins,. (2000). Materials - Peeling and sharpening multiwall nanotubes. *Nature* , 586.
- [23]. J.H.Han, M.T.A.Saif. (2006). In-situ microtensile stage for electromechanical characterization of nanoscale free standing films. *Review of Scientific Instruments* , 045102 (1-8).
- [24]. K. Bryant; D. Bernard. (2000). X-Ray Inspection for Nano-technology. *Dage X-Ray systems* , 1-5.
- [25]. K.R.Williams, K. Gupta. (2003). Etch rates for Micromachining processes- part 2. *Journal of Microelectromechanical Systems* , 761-768.
- [26]. M. A. Haque and M. T. A. Saif. (2004). Deformation mechanisms in free-standing nanoscale thin films: A quantitative in situ transmission electron microscope study. *PNAS* , 6335–6340.
- [27]. M.A Haque, M.T.A. Saif. (2002). In-Situ Tensile testing of Nano-scale Specimens in SEM and TEM. *Experimental Mechanics* , 123-128.

- [28]. M.Kiuchi, S.Matsui, Y.Isono. (2007). Mechanical Characteristics of FIB Deposited Carbon Nanowires Using an Electrostatic Actuated Nano Tensile Testing Device. *Journal of Microelectro Mechanical Systems* , 191-201.
- [29]. Material Safety Data Sheet. (n.d.). *Electronic Materials* .
- [30]. N.Scuor, P.Gallina, H.V.Panchawagh, R.L Mahajan, O.Sbaizero, V.Sergo. (2006). Design of a novel MEMS platform for the biaxial stimulation of living cells. *Biomed Microdevices* , 239-246.
- [31]. P.Poncharal, Z.L.Wang, D.Ugate, W.A.DeHeer. (1999). Electrostatic Deflections and Electromechanical Resonances of Carbon Nanotubes. *Science* , 1513-1516.
- [32]. R. Merkel, P. Nassoy, A. Leung, K. Ritchie, and E. Evans. (1999). Energy landscapes of receptor–ligand bonds explored with dynamic force spectroscopy. *Nature* , 50-53.
- [33]. R.Muller, K.R.Williams. (1996). Etch Rates for micromachining processes. *Journal of Microelectromechanical Systems* , 256-259.
- [34]. S. G. Shroff, D. R. Saner, R. Lal . (1995). Dynamic micromechanical properties of cultured rat atrial myocytes measured by atomic force microscopy. *AJP - Cell Physiology* , C286-C292.

Bibliography

- [35]. S. Lu, et al. (2006). In-situ mechanical testing of template carbon nano-tubes. *Review of Scientific Instruments* , 125101 (1-6).
- [36]. S. Yang, M.T.A. Saif. (2007). Force response and actin remodeling (agglomeration) in fibroblasts due to lateral indentation. *Acta Biomaterialia* , 77–87.
- [37]. S. Yang, M.T.A.Saif. (2005). Micromachined force sensors for the study of cell mechanics. *Review of Scientific Instruments* , 044301-(1-8).
- [38]. S.Lu, J.Chung, R.S.Ruoff. (2005). Controlled Deposition of nano-tubes on opposing electrodes. *Nanotechnology* , 1765-1770.
- [39]. S.Yang, M.T.A. Saif. (2007). MEMS based force sensors for the study of indentation response of single living cells. *Sensors and Actuators* , 16-22.
- [40]. SC 1827 Data Sheet. (n.d.). *ShIPLEY Co.*
- [41]. W.C.Tang, T.H.Nguyen, M.W.Judy, R.T.Howe. (1990). Electrostatic-comb drive of lateral polysilicon resonators. *Sensors and Actuators* , 21-23.
- [42]. Y. Tseng, T.P. Kole, D. Wirtz. (2002). Micromechanical Mapping of Live Cells by Multiple-Particle-Tracking Microrheology. *Biophysical Journal* , 3162-3176.

- [43]. Y.Zhu, A.Corigliano, H.D. Espinosa. (2006). A thermal actuator for nanoscale in situ microscopy testing: design and characterization. *Journal of Micromechanics and Microengineering* , 242-253.

- [44]. Z.C.Leseman, T.J.Mackin. (2007). Indentation testing of axisymmetric freestanding nano-films using a MEMS load cell. *Sensors and Actuators* , 264-270.

Bibliography

Appendix A

Photomask Design Form Bandwidth Foundry International Pty Ltd

Customer Name: Varun Gouthaman Date: 04/14/08

Substrate type*

Quartz	Soda Lime	other
	X	

Substrate size*

4" x 4" x 0.06"	5" x 5" x 0.09"	6" x 6" x 0.09"	7" x 7" x 0.12"	other
	X			

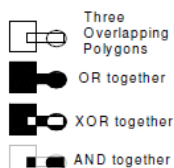
File name / Layer name/number / Top cell structure name

File name	Front side of MEMS device.tdb
Layer to be written (and GDS II number for GDS II Format only)	
Name of top cell (for GDS II Format only)	

Overlapping polygons (OLP)

Overlapping polygons defines the way they should be printed:

Print as OR	Print as XOR	Print as AND
X		



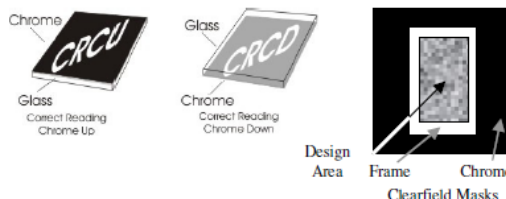
Black areas will be Chrome in a Clearfield mask and transparent in a Darkfield Mask

Polarity

Closed polygons will be transparent in Darkfield and chrome in Clearfield mode:

Darkfield	Clearfield	Frame ¹
X		

Note: If frame distance is not specified a 2 mm frame will be used to frame your design



Symmetry:

"Correct Reading Chrome up": layout equals mask when looking at chrome side
 "Correct Reading Chrome down": layout equals mask when looking at quartz side

CR Chrome up	CR Chrome down
	X

Placement on mask

Auto-centre design	Use origin of design and place it on the following coordinate (relative to mask centre)	
	x [μm]	y [μm]
X		

Required resolution*

CD > 20μm	CD > 4μm	CD > 2μm	CD > 1μm
400nm tolerance	250nm tolerance	200nm tolerance	100nm tolerance
		X	

Maximum Written Area (units)*

Length	(Units)inches
Width	inches

Requested delivery time from shop (faster delivery may cost more)*:

Shipping in 20 working days	Shipping in 10 working days	Shipping in 3 working days
	X	

Note * minimum information required for quotation, the rest is required for writing

Appendix B



Bandwidth Foundry International Pty Ltd

Suite 113, National Innovation Centre
 Australian Technology Park
 Eveleigh, NSW 1430
 Australia

Quotation

ABN	Date	Estimate #
84 125 105 857	24/04/2008	260508CR1

Name / Address
Varun Gouthaman Michigan Technological University 1400 Townsend Drive Houghton, MI 49931 USA

	Terms	Quote Valid to	Project	Other		
	Credit Card	26/06/2008	Varun Gouthaman			
Description			Qty	GST Tax AMT	Rate	Total
PHOTOMASKS File Name - Biomems device mask.tdb 5 inch Standard Soda Lime Photomask Write area - 110 by 110 mm Critical Dimension >2 micron with +/- 200 nm Tolerance Polarity - Dark Field Symmetry - CRCU, OLP - OR Resolution - Low res with writing grid at 65 nm Delivery - Normal 10 working days ex-works from acknowledged working design BFI Mask #1221 Shipping and Handling Charges				0.00	620.00	620.00
				0.00	135.00	135.00
All Amounts in US dollars			SUBTOTAL		\$755.00	
Acceptance of this quote and placement of an order is also acceptance of the payment terms. Terms: 1. Prices are EX works unless delivery charges are included. 2. Turnaround time starts on receipt of both Purchase Order and working design. Bank: National Australia Bank Branch: 260 Unley Road, Unley SA, 5061, Australia Account Name: Bandwidth Foundry International Pty Ltd BSB: 085-458, Account Number 87-287-6798 We also accept Visa or MasterCard Please advise us of Card Type, Card Number, Expiry Date and Name on Card.			Tax Total		\$0.00	
			Total		\$755.00	
Phone #		Fax #		E-mail		
+ 61-2-8374-5300		+ 61-2-8374-5301		bfi.accounts@bwfoundry.com		

Signature

Signature

Appendix C



Silicon Quest International, Inc.
 1230 Memorex Drive
 Santa Clara, CA 95050-2812
 408.496.1000 Phone
 408.496.1133 Fax

120 Woodland Avenue #E
 Reno, NV 89523
 775.356.2155 Phone
 775.356.0396 Fax

Quote For:

MICHIGAN TECHNOLOGICAL UNIVERSITY

Requestor:

VARUN G

Quote	STDQTE0000061200a
Date	6/30/2008
Page	1

ISO Control Document # F-720-012-2

Salesperson Name		F.O.B.	Shipping Method	Payment Terms	
SAT/P		Santa Clara, CA	UPS GROUND	Bankcard	
Quantity	Description	UOM	Unit Price	Ext. Price	
25	4" N/PH <1-0-0> 10-20 OHM-CM, 525±25µm PRIME SINGLE SIDE POLISHED AVAILABLE FOR IMMEDIATE SHIPMENT *****	each	\$18.2500	\$456.25	
			Subtotal	\$456.25	
			Tax	\$0.00	
			Freight	\$0.00	
			Trade Discount	\$0.00	
			Total	\$456.25	

Thank You,
Elissa Mills
(408) 496-1000 X 136
elissa@siliconquest.com
The above quote is good for 5 business days. Material is subject to prior sale.

Appendix

Appendix D



Silicon Quest International, Inc.

1230 Memorex Drive
Santa Clara, CA 95050-2812
408.496.1000 Phone
408.496.1133 Fax

120 Woodland Avenue #E
Reno, NV 89523
775.356.2155 Phone
775.356.0396 Fax

Quote For:

MICHIGAN TECHNOLOGICAL UNIVERSITY

Requestor:

VARUN GOUTHAM

Quote	STDQTE0000068178a
Date	5/27/2009
Page	1

ISO Control Document # F-720-012-2

Salesperson Name		F.O.B.	Shipping Method	Payment Terms	
Elissa		Santa Clara, CA		NET 30 DAYS	
Quantity	Description	UOM	Unit Price	Ext. Price	
10	4" P/B <100> 1-20 OHM-CM., 475-575 µm TEST WAFERS SINGLE SIDE POLISHED 10,000A±5% THERMAL OXIDE ON BOTH SIDES ESTIMATED SHIP DATE = 7 WORKING DAYS A.R.O. *****	each	\$40.00	\$400.00	

Thank You,

Elissa Mills

(408) 496-1000 X 136

elissa@siliconquest.com

The above quote is good for 5 business days. Material is subject to prior sale.
Release schedules subject to price increase with a 60 day notice.

Subtotal	\$400.00
Tax	\$0.00
Freight	\$0.00
Trade Discount	\$0.00
Total	\$400.00

Appendix E



ELECTRONIC MATERIALS

Material Safety Data Sheet

1. PRODUCT AND COMPANY IDENTIFICATION

MICROPOSIT™ SC™ 1827 Positive Photoresist

Supplier

Rohm and Haas Electronic Materials LLC
455 Forest Street
Marlborough, MA 01752 United States of America

Revision date: 04/02/2004

For non-emergency information contact: 508-481-7950

Emergency telephone number

Chemtec 800-424-9300
Rohm and Haas Emergency 215-592-3000

2. COMPOSITION/INFORMATION ON INGREDIENTS

Component	CAS-No.	Concentration
Diazo Photoactive Compound		1.0 - <= 10.0 %
Nonionic surfactant		< 1.0 %
Mixed cresol novolak resin		10.0 - <= 30.0 %
Electronic grade propylene glycol monomethyl ether acetate	108-65-6	65.0 - <= 76.0 %
Cresol	1319-77-3	< 0.9 %

3. HAZARDS IDENTIFICATION

Emergency Overview
Appearance

Form viscous liquid
Colour red
Odour sweet

Hazard Summary
CAUTION!

Combustible liquid and vapor. Causes irritation to eyes, nose, and respiratory tract.
Prolonged, repeated contact, inhalation, ingestion, or absorption through the skin, may cause toxic effects to internal organ systems (liver, kidney, central nervous system).

Potential Health Effects

Page 1 of 8

Revision date 04/02/2004

MICROPOSIT(TM) SC(TM) 1827 Positive Photoresist

Primary Routes of Entry: Inhalation, ingestion, eye and skin contact, absorption.

Eyes: May cause pain, transient irritation and superficial corneal effects.

Skin: Material may cause irritation.

Prolonged or repeated exposure may have the following effects:

drowsiness

defatting and drying of the skin which can lead to irritation and dermatitis

central nervous system depression

kidney damage

liver damage

Ingestion: Swallowing may have the following effects:

irritation of mouth, throat and digestive tract

headache

nausea

vomiting

Repeated doses may have the following effects:

central nervous system depression

liver damage

kidney damage

Inhalation: Inhalation may have the following effects:

irritation of nose, throat and respiratory tract

Higher concentrations may have the following effects:

systemic effects similar to those resulting from ingestion

Target Organs: Eye

Respiratory System

nervous system

Liver

Kidney

Skin

Carcinogenicity

Not considered carcinogenic by NTP, IARC, and OSHA

4. FIRST AID MEASURES

Inhalation: Remove from exposure. If there is difficulty in breathing, give oxygen. Seek medical attention if symptoms persist.

Skin contact: Wash skin with water. Continue washing for at least 15 minutes. Obtain medical attention if blistering occurs or redness persists.

Eye contact: Immediately flush the eye with plenty of water for at least 15 minutes, holding the eye open. Obtain medical attention if soreness or redness persists.

Ingestion: Wash out mouth with water. Have victim drink 1-3 glasses of water to dilute stomach contents. Induce vomiting if person is conscious. Immediate medical attention is required. Never administer anything by mouth if a victim is losing consciousness, is unconscious or is convulsing.

Notes to physician

MICROPOSIT(TM) SC(TM) 1827 Positive Photoresist

Treat symptomatically.

5. FIRE- FIGHTING MEASURES

Flash point 40 - 46 °C (104 - 115 °F)

Suitable extinguishing media: Use water spray, foam, dry chemical or carbon dioxide.
Keep containers and surroundings cool with water spray.

Specific hazards during fire fighting: This product may give rise to hazardous vapors in a fire. Vapors can travel a considerable distance to a source of ignition and result in flashback.

Special protective equipment for fire-fighters: Wear full protective clothing and self-contained breathing apparatus.

Further information: Pressure may build up in closed containers with possible liberation of combustible vapors.

6. ACCIDENTAL RELEASE MEASURES

Personal precautions

Wear suitable protective clothing.
Wear respiratory protection.
Eliminate all ignition sources.

Environmental precautions

Prevent the material from entering drains or water courses.
Do not discharge directly to a water source.
Advise Authorities if spillage has entered watercourse or sewer or has contaminated soil or vegetation.

Methods for cleaning up

Contain spills immediately with inert materials (e.g., sand, earth).
Transfer into suitable containers for recovery or disposal.
Finally flush area with plenty of water.

7. HANDLING AND STORAGE

Handling

Use local exhaust ventilation. Avoid contact with eyes, skin and clothing. Keep container tightly closed.

Further information on storage conditions: Proprietary photoresist film contains approximately 2-4% of 2,3,4-trihydroxybenzophenone (THBP), which may sublime during soft-bake or hard-bake processing. THBP has low acute toxicity (LD50>5g/kg). Contact with eyes, skin or mucous membranes cause irritation. To prevent accumulation of THBP on equipment surfaces and ventilation ducts, preventative maintenance program including regular cleaning should be implemented. Wipe surfaces using an appropriate cleaning solvent when possible. Provide adequate general or local exhaust ventilation during the cleaning process. In situations where this is not possible or where solvent or dust concentrations become excessive, use an air purifying respirator with an organic vapor/toxic particulate cartridge. When cleaning residual THBP, wear protective gloves and adequate protective clothing to prevent skin contact. Practice good personal hygiene to prevent accidental exposure. Clean all protective clothing and equipment thoroughly after each use.

MICROPOSIT(TM) SC(TM) 1827 Positive Photoresist

Storage

Storage conditions: Store in original container. Keep away from heat and sources of ignition.
Storage area should be: cool dry well ventilated out of direct sunlight

8. EXPOSURE CONTROLS / PERSONAL PROTECTION**Exposure limit(s)**

Exposure limits are listed below, if they exist.

Component	Regulation	Type of listing	Value
Electronic grade propylene glycol monomethyl ether acetate	Rohm and Haas	TWA	30 ppm
	Rohm and Haas	STEL	90 ppm
	Rohm and Haas	Absorbed via skin	
Component	Regulation	Type of listing	Value
Cresol	ACGIH	TWA	22 mg/m3 5 ppm
	ACGIH	SKIN_DES	
	OSHA_TRANS	PEL	22 mg/m3 5 ppm
	OSHA_TRANS	SKIN_DES	

Eye protection: goggles

Hand protection: Butyl rubber gloves. Other chemical resistant gloves may be recommended by your safety professional.

Skin and body protection: Normal work wear.

Respiratory protection: Respiratory protection if there is a risk of exposure to high vapor concentrations. The specific respirator selected must be based on the airborne concentration found in the workplace and must not exceed the working limits of the respirator.

Engineering measures: Engineering methods to prevent or control exposure are preferred. Methods include process or personnel enclosure, mechanical ventilation (local exhaust), and control of process conditions.

9. PHYSICAL AND CHEMICAL PROPERTIES**Appearance**

Form	viscous liquid
Colour	red
Odour	sweet
pH	neutral
Boiling point/range	146 °C (295 °F)
Flash point	40 - 46 °C (104 - 115 °F)

MICROPOSIT(TM) SC(TM) 1827 Positive Photoresist

Component:	<u>Electronic grade propylene glycol monomethyl ether acetate</u>
Vapour pressure	3.7 mmHg at 20 °C
Relative vapour density	Heavier than air.
Water solubility	insoluble
Relative density	1.05
Evaporation rate	Slower than ether
VOC's	697 - 768 g/l

NOTE: The physical data presented above are typical values and should not be construed as a specification.

10. STABILITY AND REACTIVITY

Hazardous reactions	Stable under normal conditions.
Conditions to avoid	High temperatures Static discharge
Materials to avoid	Oxidizing agents
Hazardous decomposition products polymerization	Combustion will generate:, Carbon monoxide, carbon dioxide, toxic fluorine compounds, nitrogen oxides (NOx), aldehydes, acrid smoke and irritating fumes, Will not occur.

11. TOXICOLOGICAL INFORMATION

Toxicological information on this product or its components appear in this section when such data is available.

Component:	<u>Nonionic surfactant</u>
Acute oral toxicity	LD50 rat > 10,000 mg/kg
Component:	<u>Electronic grade propylene glycol monomethyl ether acetate</u>
Acute oral toxicity	LD50 rat 8,532 mg/kg
Component:	<u>Cresol</u>
Acute oral toxicity	LD50 rat 2,737 mg/kg
Component:	<u>Electronic grade propylene glycol monomethyl ether acetate</u>
Acute inhalation toxicity	LC50 rat 6 h 23.49 mg/l
Component:	<u>Cresol</u>
Acute inhalation toxicity	LC50 rat 8 h 35.38 mg/l
Component:	<u>Nonionic surfactant</u>
Acute dermal toxicity	> 5,000 mg/kg
Component:	<u>Electronic grade propylene glycol monomethyl ether acetate</u>

MICROPOSIT(TM) SC(TM) 1827 Positive Photoresist

Acute dermal toxicity	LD50 rabbit >5,000 mg/kg
Component: <u>Cresol</u>	
Acute dermal toxicity	LD50 rabbit > 5,000 mg/kg
Component: <u>Electronic grade propylene glycol monomethyl ether acetate</u>	
Toxicity to reproduction	
Dermal teratology testing of this solvent (with less than 3% beta isomer) revealed no maternally toxic, teratogenic or fetotoxic responses in rats or rabbits exposed to concentrations of 1,000 and 2,000 mg/kg per day.	
Component: <u>Electronic grade propylene glycol monomethyl ether acetate</u>	
Mutagenicity	
No significant mutagenic response was observed and the carcinogenic potential of the material is therefore considered to be low.	
Component: <u>Cresol</u>	
Toxicity to reproduction	
Developmental effects were seen in laboratory animals only at dose levels that were maternally toxic.	

12. ECOLOGICAL INFORMATION

Ecotoxicological information on this product or its components appear in this section when such data is available.

Electronic grade propylene glycol monomethyl ether acetate

Ecotoxicity effects	
Toxicity to fish	LC50 Fathead minnow (Pimephales promelas) 96 h 161 mg/l
Toxicity to aquatic invertebrates	EC50 Daphnia magna 48 h >500 mg/l

13. DISPOSAL CONSIDERATIONS

Environmental precautions: Prevent the material from entering drains or water courses.
Do not discharge directly to a water source.
Advise Authorities if spillage has entered watercourse or sewer or has contaminated soil or vegetation.

Disposal

Dispose in accordance with all local, state (provincial), and federal regulations. Incineration is the recommended method of disposal for containers. Under RCRA, it is the responsibility of the product's user to determine at the time of disposal, whether the product meets RCRA criteria for hazardous waste. This is because the product uses, transformations, mixtures, processes, etc. may render the resulting materials hazardous.
Do not remove label until container is thoroughly cleaned. Empty containers may contain hazardous residues. This material and its container must be disposed of in a safe way.

14. TRANSPORT INFORMATION**DOT**

MICROPOSIT(TM) SC(TM) 1827 Positive Photoresist

Not regulated per 49CFR 173.150(f)(2)

IMO/IMDG

Proper shipping name	RESIN SOLUTION
UN-No	UN 1866
Class	3
Packing group	III

15. REGULATORY INFORMATION

SARA TITLE III: Section 311/312 Categorizations (40CFR370): Immediate, delayed, flammability hazard

SARA TITLE III: Section 313 Information (40CFR372)

This product does not contain a chemical which is listed in Section 313 at or above de minimis concentrations.

U.S. Toxic Substances Control Act (TSCA) Section 12(b) Export Notification (40 CFR 707, Subpt D):

U.S. Toxic Substances Control Act (TSCA) Section 12(b) Export Notification (40 CFR 707, Subpt D)
This product does not contain any substances subject to Section 12(b) export notification.

US. Toxic Substances Control Act (TSCA) All components of this product are in compliance with the inventory listing requirements of the U.S. Toxic Substances Control Act (TSCA) Chemical Substance Inventory.

California (Proposition 65)

This product does not contain materials which the State of California has found to cause cancer, birth defects or other reproductive harm.

16. OTHER INFORMATION**Hazard Rating**

	Health	Fire	Reactivity
NFPA	2	2	0

Legend

ACGIH	American Conference of Governmental Industrial Hygienists
BAC	Butyl acetate
OSHA	Occupational Safety and Health Administration
PEL	Permissible Exposure Limit
STEL	Short Term Exposure Limit (STEL):
TLV	Threshold Limit Value
TWA	Time Weighted Average (TWA):
	Bar denotes a revision from prior MSDS.

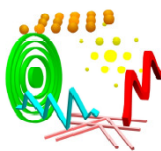
Appendix

MICROPOSIT(TM) SC(TM) 1827 Positive Photoresist

The information provided in this Safety Data Sheet is correct to the best of our knowledge, information and belief at the date of its publication. The information given is designed only as a guidance for safe handling, use, processing, storage, transportation, disposal and release and is not to be considered a warranty or quality specification. The information relates only to the specific material designated and may not be valid for such material used in combination with any other materials or in any process, unless specified in the text.

Print Date: Version: 3.0
 11/30/2005
 Layout 304773

Appendix F

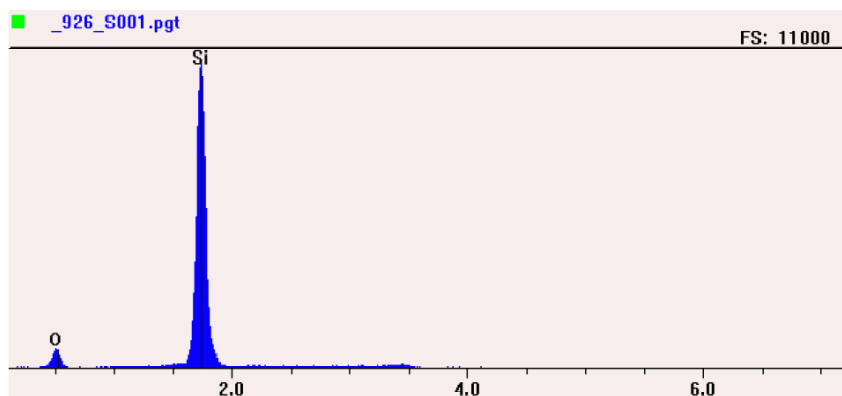


Applied Chemical and Morphological Analysis Laboratory,
Michigan Technological University

Spectrum Report
Monday, July 06, 2009

File: C:\Program Files\PGT_926_S001.pgt
Collected: July 06, 2009 13:53:45

Live Time: 100.00 Count Rate: 1510 Dead Time: 22.87 %
Beam Voltage: 20.00 Beam Current: 0.20 Takeoff Angle: 40.00



Element	Line	keV	KRatio	Wt%	At%	At Prop	ChiSquared
Si	KA1	1.740	0.5942	68.27	55.07	6.1	89.72
O	KA1	0.523	0.0954	31.73	44.93	5.0	9.93
Total			0.6896	100.00	100.00	11.1	65.63

Element	Line	Gross (cps)	BKG (cps)	Overlap (cps)	Net (cps)	P:B Ratio
Si	KA1	890.6	11.8	0.0	878.8	74.8
O	KA1	46.2	2.6	0.0	43.6	17.0

Element	Line	Det Eff	Z Corr	A Corr	F Corr	Tot Corr	Modes
Si	KA1	0.861	1.033	1.113	1.000	1.149	Element
O	KA1	0.210	0.938	3.550	0.999	3.326	Element